

Morphology and mechanical properties of abdominal aortic aneurysms

Citation for published version (APA):

Dam, van, E. A. (2007). *Morphology and mechanical properties of abdominal aortic aneurysms*. [Phd Thesis 1 (Research TU/e / Graduation TU/e), Mechanical Engineering]. Technische Universiteit Eindhoven.
<https://doi.org/10.6100/IR627626>

DOI:

[10.6100/IR627626](https://doi.org/10.6100/IR627626)

Document status and date:

Published: 01/01/2007

Document Version:

Publisher's PDF, also known as Version of Record (includes final page, issue and volume numbers)

Please check the document version of this publication:

- A submitted manuscript is the version of the article upon submission and before peer-review. There can be important differences between the submitted version and the official published version of record. People interested in the research are advised to contact the author for the final version of the publication, or visit the DOI to the publisher's website.
- The final author version and the galley proof are versions of the publication after peer review.
- The final published version features the final layout of the paper including the volume, issue and page numbers.

[Link to publication](#)

General rights

Copyright and moral rights for the publications made accessible in the public portal are retained by the authors and/or other copyright owners and it is a condition of accessing publications that users recognise and abide by the legal requirements associated with these rights.

- Users may download and print one copy of any publication from the public portal for the purpose of private study or research.
- You may not further distribute the material or use it for any profit-making activity or commercial gain
- You may freely distribute the URL identifying the publication in the public portal.

If the publication is distributed under the terms of Article 25fa of the Dutch Copyright Act, indicated by the "Taverne" license above, please follow below link for the End User Agreement:

www.tue.nl/taverne

Take down policy

If you believe that this document breaches copyright please contact us at:

openaccess@tue.nl

providing details and we will investigate your claim.

Morphology and mechanical properties of Abdominal Aortic Aneurysms

A catalogue record is available from the Eindhoven University of Technology Library

ISBN: 978-90-386-1057-3

Cover design: Evelyne van Dam & Jorrit van Rijt, Oranje Vormgevers
Printed by Universiteitsdrukkerij TU Eindhoven, Eindhoven, The Netherlands.

This research was performed in the scope of the hemodyn project, a cooperation between Philips Medical systems (Healthcare IT - Advanced Development), Best, the Technische Universiteit Eindhoven (Biomedical Engineering department), Eindhoven and the Erasmus University (Thoraxcenter, Biomedical Engineering), Rotterdam. The Hemodyn project is partly funded by SenterNovem (Dutch Ministry of economic affairs).

Morphology and mechanical properties of Abdominal Aortic Aneurysms

PROEFSCHRIFT

ter verkrijging van de graad van doctor
aan de Technische Universiteit Eindhoven,
op gezag van de Rector Magnificus, prof.dr.ir. C.J. van Duijn,
voor een commissie aangewezen door het College voor Promoties
in het openbaar te verdedigen op
dinsdag 3 juli 2007 om 16.00 uur

door

Evelyne Andrea van Dam

geboren te Maastricht

Dit proefschrift is goedgekeurd door de promotor:

prof.dr.ir. F.N. van de Vosse

Copromotoren:

dr.ir. M.C.M. Rutten

en

dr.ir. G.W.M. Peters

*- neet zeure, begin, 't het genne zin
ge wacht tevergeafs op 'n wonder -*

Vechte, valle en opstoan - Rowwen Heze

Contents

Summary	ix
1 Introduction	1
1.1 Abdominal Aortic Aneurysms	2
1.2 Treatment	4
1.3 Rupture risk prediction	5
1.4 Objective and outline	6
2 Determination of Linear Viscoelastic Behaviour of Abdominal Aortic Aneurysm Thrombus	9
2.1 Introduction	10
2.2 Methods and Materials	12
2.2.1 Methods	12
2.2.2 Discrete transition group	13
2.2.3 Continuous transition group	14
2.3 Results	15
2.3.1 Discrete transition	15
2.3.2 Continuous transition	17
2.4 Discussion	18
2.5 Conclusion	21
3 Non-linear Viscoelastic Behaviour of Abdominal Aortic Aneurysm Thrombus	23
3.1 Introduction	24
3.2 Methods	26
3.2.1 Kinematics	26
3.2.2 The constitutive model	27
3.2.3 Determination of material parameters	29
3.3 Results	33
3.3.1 Small strain experiments	33
3.3.2 Large strain experiments	34
3.4 Discussion	35
3.5 Conclusion	41

4	Discrimination of Components of AAA Vessel Wall by Multi Contrast MRI	43
4.1	Introduction	44
4.2	Methods and Materials	45
4.2.1	Multi Contrast MRI	45
4.2.2	μ CT & histology	46
4.2.3	Image analysis	48
4.3	Results	51
4.4	Discussion	51
5	A Mixed Numerical Experimental Method for Mechanical Characterisation of AAA Vessel Wall	55
5.1	Introduction	56
5.2	Mixed numerical experimental method	57
5.2.1	Load protocol and MR imaging	58
5.2.2	Digital Image Correlation	59
5.2.3	Mesh generation and Finite Element Modelling	61
5.2.4	Parameter estimation	61
5.3	Validation	62
5.3.1	Simulation	62
5.3.2	Results simulation	64
5.3.3	Experiment	64
5.3.4	Results experiment	65
5.4	Discussion	66
6	Local Mechanical Properties of Abdominal Aortic Aneurysms	69
6.1	Introduction	70
6.2	Methods	71
6.3	Results	74
6.4	Discussion	75
7	General Discussion: Towards Rupture Risk Analysis	81
7.1	Introduction	82
7.2	Implication for wall stress analyses	83
7.3	Limitations for clinical application	87
7.4	Future aspects	88
	References	89
	Samenvatting	97
	Dankwoord	99
	Samenvatting	99
	Curriculum Vitae	101

Morphology and mechanical properties of Abdominal Aortic Aneurysms: Summary

Abdominal Aortic Aneurysm (AAA) rupture is a life-threatening event, but can, when diagnosed timely, be avoided by either endovascular or conventional repair. Since these methods are accompanied by a high mortality rate, the decision to operate should only be made when the rupture risk exceeds the risks of repair. To date, the maximum diameter of the aneurysm is used as a measure for rupture risk and hence as a criterion for surgical intervention. It has, however, been shown already that small aneurysms do rupture sometimes, while some large aneurysms have not ruptured yet, and therefore the diameter criterion alone may not be sufficient. Since rupture of an AAA occurs when locally the wall stress exceeds the strength of the vessel wall, it is generally believed that wall stress distribution could help to better assess AAA rupture.

Patient specific models for wall stress computations do not only require the geometry of the aneurysm but also the mechanical properties of the aneurysm tissue. Studies on the material properties of vessel wall have mainly focused on describing AAA vessel wall and thrombus as a homogeneous material. Local inhomogeneities can have large influences on the stress magnitude and distributions. AAA vessel wall may contain inhomogeneities such as calcifications and atherosclerotic plaques. Furthermore, the thrombus, which is present in the majority of the aneurysms may influence the local mechanics considerably. It is a layered fibrin structure, that shows different levels of degeneration. The level of degeneration of the fibrin structure might have influence on the mechanical properties of the thrombus.

To improve future wall rupture risk prediction based on wall stress, the objective of this study is to obtain the local mechanical properties of both thrombus and the AAA vessel wall.

AAA vessel wall and thrombus are obtained from patients treated with conventional surgery. The viscoelastic behaviour of thrombus is determined using plate-plate rheom-

etry. To study the changes in mechanical properties throughout the thickness of the thrombus a radially oriented stack of samples was used. In the small strain regime frequency sweep test are performed and the elastic and viscous moduli are found to be in the range of 1.7 ± 1.3 kPa and 0.2 ± 0.1 kPa respectively. Since large deformations occur in thrombus the non-linear properties are determined by stress relaxation experiments. To describe the phenomena observed experimentally, a non-linear multi mode model is used. The parameters for this model are obtained by fitting this model successfully to the experiments in both the linear and non-linear regime.

To determine the morphology of the AAA vessel wall, the applicability of multi contrast MRI to discriminate the components of the vessel wall is studied. Multi contrast MR results are compared to the golden standards, histology and μ CT. Components like the media, calcified deposits, areas containing cholesterol, thrombus and the adventitia containing fat cells and vasa vasorum can be recognised in the MR images. The results obtained so far are not suitable for an automatic classification by an unsupervised clustering algorithm.

To obtain the mechanical properties of the components present in the vessel wall a mixed numerical experimental method is proposed. This method is a robust way to determine the mechanical properties of the individual components without having to isolate them.

The method is applied to AAA vessel wall samples. The morphology is obtained with multi contrast MR. The Young's moduli of media, adventitia, calcification, an area with cholesterol crystals and thrombus are determined. Although the media is less stiff than the adventitia the moduli are in same the order of magnitude (≈ 1.0 MPa). The stiffness of thrombus is found to be an order of magnitude lower (≈ 40 kPa). An area with a lot of cholesterol is stiffer than the rest of the wall (≈ 7.5 MPa) and a calcified area is even stiffer (≈ 50 MPa).

By implementing the findings for thrombus in a patient specific model it is shown that thrombus does change the stress distribution and peak wall stresses, but the effect is much lower than reported in literature by others. The presence of calcification has a large effect on the wall stress distribution. It is shown that the wall stress distribution is influenced by the accuracy with which the geometry of the calcification is described. The limited resolution available in the clinical setting results in a non-realistic stress distribution. For correct implementation of inhomogeneities of the vessel wall the spatial resolution of both imaging techniques and computations should increase.

The contribution of this work consists not only of the reported morphologies and mechanical properties. The observations reported in this work also suggest that effort should be put into development of clinical methods to include the morphology and mechanical properties of the aneurysm into the rupture risk analysis.

Chapter 1

Introduction

1.1 Abdominal Aortic Aneurysms

The aorta is the main blood vessel of the human body and its major function is to transport blood to the organs and the extremities. The abdominal aorta is the part of the aorta between the diaphragm and the bifurcation to the left and right common iliac arteries. An abdominal aortic aneurysm (AAA) is a localised dilation of the aorta between the renal arteries and the bifurcation to the iliac arteries (figure 1.1). This abdominal part of the aorta is classified as aneurysmal when the diameter has increased 50% compared to the expected normal diameter of the artery, or the diameter proximal to the dilation.

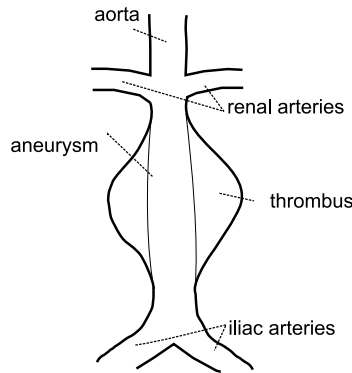


Figure 1.1: Schematic view of an Abdominal Aortic Aneurysm.

In a Norwegian population-based study, the diameter of the abdominal aorta of 6386 men and women aged 25-84 years was measured. AAA was present in 8.9% of the men and 2.2% of the women (Singh et al., 2001). Although some AAA patients have vague symptoms like back pain or an abdominal pain, most AAA are symptomless until the event of rupture, which is lethal for 65% to 85% of the patients (van der Vliet and Boll, 1997). Each year, approximately 15 000 deaths in the USA are attributed to abdominal aortic aneurysms (Grange et al., 1997). Elderly, a growing segment of the population, are primarily affected by this disease (Grange et al., 1997). 1.3% of the deaths in men and 0.6% in women over the age of 65 are caused by abdominal aortic aneurysms. Within this group the incidence of aneurysm development seems to be increasing (Wolf and Bernstein, 1994).

Although the mechanisms in development of AAA are still unclear, it is likely that changes in the contents of the vessel wall play an important role in the development of an AAA. The wall of a healthy aorta consists of three layers. The tunica interna or intima is the innermost layer, lined by endothelium. The intermediate thick elastic layer is called the tunica media and consists of elastic fibres (elastin), collagen and smooth muscle cells (SMC). SMCs synthesise the components of the extracellular matrix. The tunica externa or adventitia is the tough outer layer, which consists mainly

of collagen fibres. Adventitial fibroblasts also have the capacity to synthesise extra cellular matrix components. The most important structural macromolecules of the aortic wall are elastin and fibrillar collagen. The elastic properties of elastin enable it to stretch to twice its original length and then rapidly return to its normal size. The elasticity of elastin helps to maintain vessels at their normal dimensions. Fibrillar collagen provides the wall with tensile strength (Dobrin, 1989). The molecules are long, thin rods, which are coiled around one another into a triple helix. Fibrillar collagen has a tensile strength over 20 times larger than that of elastin (MacSweeney et al., 1994). The close association of elastin, collagen and SMCs in the aortic media is responsible for the viscoelastic properties of the aorta (Wills et al., 1996). The dilatation is accompanied by a decrease in SMC and elastin content of the media and dense inflammatory infiltrates (Carmo et al., 2002; Wills et al., 1996). The changes in collagen structure and content are still controversial. Both an increase in collagen content (Grange et al., 1997; He and Roach, 1994; Wills et al., 1996) as a decrease (Sumner et al., 1970) have been reported. Carmo et al. (2002) found no change in collagen content but suggest that old collagen accumulates cross-links while new collagen biosynthesis is somehow defective. The abdominal aorta is a region prone to develop advanced atherosclerotic plaques (Wassef et al., 2007). Aortic calcification is common in AAA patients. The stiffness of the calcifications limits the deformation of the vessel wall (Marra et al., 2006).

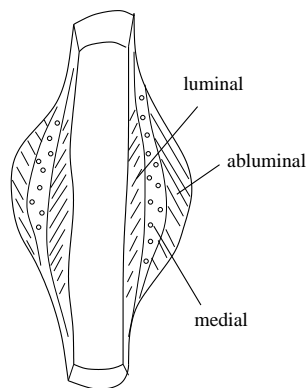


Figure 1.2: *Thrombus can be divided in luminal, medial and abluminal thrombus*

AAAs are lined with intraluminal laminated thrombus to varying extent. Thrombus is a fibrin structure infiltrated with blood cells, platelets, blood proteins and cellular debris (Falk, 1992). Observation of thrombus reveals that three types of thrombus exist (figure 1.2). New thrombus is formed at the luminal side and appears red. Fibrin fibres are clearly identifiable, arranged into primary, thick fibrin bundles and a fine secondary cross linked structure. Attached to this thrombus is a more aged region, which appears white. Fibres in this regions have degenerated. In the abluminal region, the thrombus has aged most and all fibres appear degenerated, no structure

can be recognised (Wang et al., 2001).

When the fine structure and cellular composition is studied, it can be demonstrated that thrombus contains a system of reticular canaliculi (Adolph et al., 1997). This is a delivery system for both cells and macromolecules, although cells do not seem to penetrate the thrombus beyond the first centimetre. Near the surface deposition of new thrombus by the penetrating platelets occurs more than thrombus degradation. Degradation of thrombus is concentrated in the abluminal region, and in absence of cells, thrombus is not renewed.

Studies of the pathogenic influence of thrombus on AAA show that the aneurysm wall covered with thrombus is thinner and shows more frequent signs of inflammation (Kazi et al., 2003). This may, together with local mural neovascularisation, be caused by localised hypoxia (Vorp et al., 2001). This may lead to regional wall weakening and thereby increase the risk of aneurysm rupture.

1.2 Treatment

Although the life expectancy of individuals with symptomless AAA is decreased by the chance of rupture, elective surgical correction can improve survival rates (van der Vliet and Boll, 1997). Every year, 40 000 people undergo surgical repair to prevent rupture. When performed in an emergency these operations are, however, associated with a mortality rate of 50%. Mortality rates in elective surgery are still as high as 5% (Grange et al., 1997; Franks et al., 2007). Conventional surgery requires a major operation during which the dilated part of the abdominal aorta is replaced by an artificial graft. An incision is made from the bottom of the sternum to the pubic bone. After laying aside the intestines the aorta is clamped. Next, the aorta is incised and the thrombus inside the aneurysm is removed. The graft material is then sutured into the healthy part of the aorta just below the renal arteries. After cutting it to length, the graft is sutured into the iliac arteries. The clamps are removed and the wall over the aneurysm is closed over the graft to prevent the graft from eroding into the surrounding intestine (Brands, 2003). Open surgical repair is, however, associated with significant morbidity rates in 15% to 30% of the patients (Uflacker and Robison, 2001; Zarins et al., 1999). Less invasive treatment has therefore become favourable in the majority of the cases.

Endovascular repair of an AAA was first performed by Parodi et al. (1991). They performed the first human stent graft placement for treatment of AAA in 1990 (Parodi et al., 1991; Uflacker and Robison, 2001). The device was balloon expandable and used a stent, stitched to a Dacron tube. Results were encouraging and endovascular repair is now employed worldwide. Problems with these endovascular devices arise when endoleak occurs. Endoleak is a condition unique to endoluminal vascular grafts defined by the persistence of blood flow outside the lumen of the endoluminal graft but within the aneurysm sac (Uflacker and Robison, 2001). The pressure in the lumen does not decrease in this situation and the risk of rupture is not diminished. Although the endoleak rate decreased over the years it still occurs in approximately 10% of the patients (Franks et al., 2007).

Since conventional and endovascular repair are accompanied by a 30-day mortality rate of 4.0 % versus 2.9% (Hua et al., 2005), the decision to operate should only be made when rupture risk exceeds the risks of repair.

1.3 Rupture risk prediction

To date, the maximum diameter of the aneurysm is used as a measure for rupture risk and hence as a criterion for surgical intervention. Aneurysm size is the most important factor related to likelihood of rupture. Although rupture may occur with an aortic diameter of less than 4 cm, the risk is very small. For aneurysms smaller than 5 cm the annual chance of rupture is about 0.5% and for aneurysms between 5 and 6 cm the chance of rupture increases to 5%. The risk increases exponentially for even larger aneurysms (van der Vliet and Boll, 1997; Wolf and Bernstein, 1994). It has, however, been shown already that small aneurysms do rupture sometimes, while some large aneurysms have not ruptured yet, and therefore the diameter criterion alone may not be sufficient. Since rupture of an AAA occurs when locally the wall stress exceeds the strength of the vessel wall, it is generally believed that wall stress distribution could help to better assess AAA rupture. Several studies of AAA wall stress by means of computational methods have been reported in literature.

Studies using idealised geometries showed that the wall stress distribution of an aneurysm is dependent on the wall thickness (Scotti et al., 2005), diameter (Stringfellow et al., 1987; Vorp et al., 1998) and shape (Hua and Mower, 2001; Scotti et al., 2005; Stringfellow et al., 1987; Vorp et al., 1998). Since geometries of aneurysms are widely complex (Sacks et al., 1999), several studies focused on patient specific models. Wall stress turned out to be complexly distributed, to show large regional variations (Raghavan et al., 2000; Thubrikar et al., 2001a) and to be sensitive to small geometrical variations (de Putter et al., 2006a). Peak wall stress was correlated to the site of rupture (Venkatasubramaniam et al., 2004) and was suggested to be a superior rupture risk predictor compared to diameter (Fillinger et al., 2002, 2003; Raghavan et al., 2005; Venkatasubramaniam et al., 2004).

The effect of the presence of thrombus has been studied on both idealised (di Martino et al., 1998; Inzoli et al., 1993; Mower et al., 1997) and patient specific models (di Martino and Vorp, 2003; Wang et al., 2002). Thrombus was found to reduce and redistribute wall stress. The size of the effect is dependent on the size and the mechanical properties of the thrombus. Atherosclerotic plaques cause stress concentration and a significant increase in maximum stress (Inzoli et al., 1993). The effect of calcification is similar. Speelman et al. (2007) reported that not only the relative amount but also location and shape of the calcified regions influence the wall stress. de Putter et al. (2006b) showed that peak wall stress is sensitive to the material properties of the calcification. Several recent studies also included fluid-dynamics by application of fluid-structure interactions (Breeuwer et al., 2004; di Martino et al., 2001; Papaharilaou et al., 2007; Scotti et al., 2005; Wolters et al., 2005). An underestimation of peak wall stress is reported when fluid dynamics are not incorporated

(Papaharilaou et al., 2007; Scotti et al., 2005).

The mechanical properties of the thrombus, used in these models were either assumed (Inzoli et al., 1993; Mower et al., 1997) or were determined by fitting tensile test data to a linear elastic model (di Martino et al., 1998) or to a two-parameter, hyper elastic, isotropic and incompressible material model (Wang et al., 2001, 2002). An ideal model for calculating AAA wall stresses would include loading with a dynamic pressure and applying a proper constitutive model that also incorporates the position dependent viscoelastic properties of the thrombus.

The mechanical properties of the vessel wall in the several patient specific models are assumed to be linear elastic (Inzoli et al., 1993; Hua and Mower, 2001; di Martino et al., 2001; Mower et al., 1997; Scotti et al., 2005; Stringfellow et al., 1987; Vorp et al., 1996, 1998; Wolters et al., 2005). Parameters are either estimated or experimentally determined (di Martino et al., 2001). The stress-strain curve which results from uniaxial test can be described by $\sigma = ae^b$ (He and Roach, 1994; Thubrikar et al., 2001b) or by a two parameter, hyper elastic, isotropic, incompressible model (Raghavan and Vorp, 2000). The latter has been implemented in several studies on the wall stresses in AAA (de Putter et al., 2007; Fillinger et al., 2003; di Martino and Vorp, 2003; Papaharilaou et al., 2007; Raghavan et al., 2000; Raghavan and Vorp, 2000; Raghavan et al., 2005; Venkatasubramaniam et al., 2004; Wang et al., 2002). These models all assume the vessel wall to be an isotropic material.

For thrombus and vessel wall the influence of variations in the parameters of the hyper elastic model was found to be negligible when values varied within the standard deviation found by experiments. It was concluded that population means can be used reasonably in wall stress evaluations (di Martino and Vorp, 2003; Raghavan and Vorp, 2000).

1.4 Objective and outline

Studies on the material properties of vessel wall have mainly focused on describing AAA vessel wall as a homogeneous material. Local inhomogeneities can, however, have large influences on the stress magnitude and distribution as can be concluded from the previously described effect of atherosclerotic plaques and calcifications (Inzoli et al., 1993; de Putter et al., 2006b). To improve future wall rupture risk prediction based on wall stress, the objective of this study is to obtain the local mechanical properties of both thrombus and the AAA vessel wall.

A schematic overview of the contents of this work is shown in figure 1.3. For the thrombus, one might expect a gradient in mechanical properties over the laminated structure. The material should, as proposed in the previous section, be described by a viscoelastic model. Chapter 2 will focus on the use of rheometry as a tool for measuring linear viscoelastic properties of thrombus. In chapter 3 the position dependent non-linear viscoelastic behaviour of the thrombus is determined. A non-linear viscoelastic material model is presented to describe the phenomena observed experimentally.

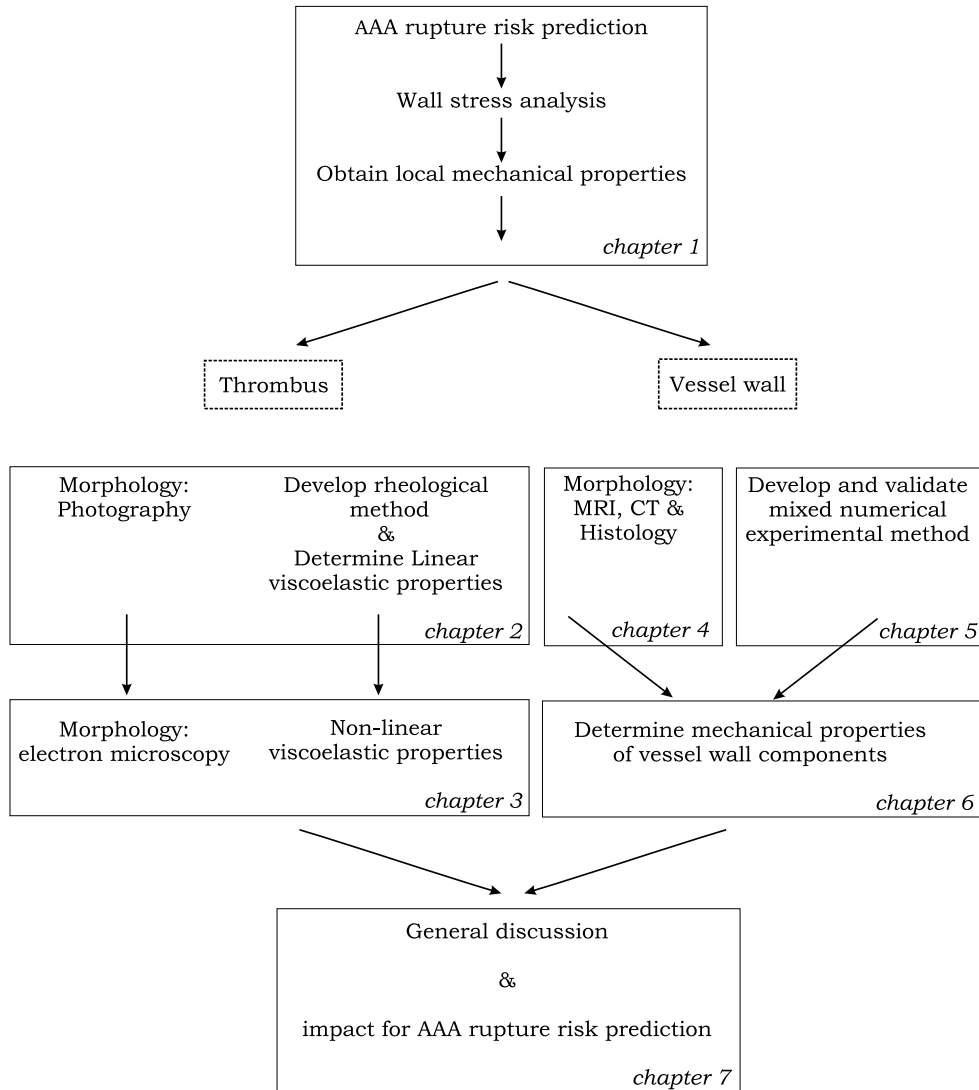


Figure 1.3: Overview of contents

The composition of the vessel wall is known to show local variations. Since mechanical properties and composition are strongly related, local variations in mechanical properties are expected in the vessel wall. These might have large influence on the wall stress analyses. Isolation of the individual components will automatically result in destruction of tissue morphology. Therefore, the mechanical properties of individual components need to be tested when integrated in their original surrounding tissue. To achieve this a non-destructive method, Magnetic Resonance Imaging (MRI) is used to obtain information from the different components of the vessel wall. MRI is a widely used method to study the components of human atherosclerotic plaques (Cappendijk et al., 2002; Clarke et al., 2003; Correia et al., 1997; Fayad et al., 1998; Kooi et al., 2003; Luk-Pat et al., 1999; Shinnar et al., 1999; Toussaint et al., 1996; Yuan et al., 1998, 2001, 2002; Zimmermann-Paul et al., 1999). Shinnar et al. (1999) showed that calcium, fibrocellular tissue, lipid, lipid rich core and thrombus can be distinguished using multi contrast MR images of the carotid walls. The relationship between these components, their MR grey values and their mechanical properties is of great importance for the patient specific wall stress analysis. If this relationship is known the local mechanical properties can be assigned to the vessel wall in the wall stress analyses based on the MR findings alone.

In chapter 4 the composition of the AAA wall will be studied by using these multi contrast MR techniques. Histology and μ CT are used as golden standards. In chapter 5 an inverse method is described with which local mechanical properties can be determined by a combination of tensile tests and MR imaging. This method is applied to AAA samples in chapter 6 to obtain the local mechanical properties. The final chapter will summarise the work done and discuss the influence of the variations found in mechanical properties on the AAA wall stress analyses and the subsequent rupture risk prediction.

Chapter 2

Determination of Linear Viscoelastic Behaviour of Abdominal Aortic Aneurysm Thrombus

This chapter is based on: EA van Dam, SD Dams, GWM Peters, MCM Rutten, GWH Schurink, J Buth and FN van de Vosse, *Determination of Linear Viscoelastic Behavior of Abdominal Aortic Aneurysm Thrombus*, *Biorheology*, **43**(6),695-707,2006.

2.1 Introduction

Abdominal Aortic Aneurysm (AAA) rupture is a life-threatening event, but can, when diagnosed timely, be avoided by either endovascular or conventional repair. Since these methods are accompanied by a 30-day mortality rate of 2.9% versus 4.0% (Hua et al., 2005), the decision to operate should only be made when rupture risk exceeds the risks of repair. Presently, the maximum diameter of the aneurysm is used as a measure of rupture risk and hence as a criterion for surgical intervention. Since rupture of an AAA occurs when locally the wall stress exceeds the strength of the vessel wall, it has already been suggested that wall stress is a more reliable rupture predictor than the maximum vessel diameter (Fillinger et al., 2003). Stress analyses of AAAs have already been performed by several groups using computational methods (di Martino et al., 1998; Fillinger et al., 2002; Inzoli et al., 1993; Mower et al., 1997; Raghavan et al., 2000; Thubrikar et al., 2001a; Wang et al., 2002; Wolters et al., 2005) and in some of these analyses the effect of intraluminal thrombus, present in most AAAs, on the stress distribution was incorporated (di Martino et al., 1998; Inzoli et al., 1993; Mower et al., 1997; Wang et al., 2002). The presence of a thrombus is found to alter the wall stress distribution and to reduce the peak wall stress. The mechanical properties of the thrombus, used in these models were either assumed (Inzoli et al., 1993; Mower et al., 1997) or were determined by fitting tensile test data to a linear elastic model (di Martino et al., 1998) or to a two-parameter, hyper elastic, isotropic and incompressible model (Wang et al., 2001, 2002). An ideal model for calculating AAA wall stresses would include loading with a dynamic pressure and applying a proper constitutive model that also incorporates the position dependent viscoelastic properties of the thrombus.

A thrombus is a fibrin structure infiltrated with blood cells, blood proteins and cellular debris (Falk, 1992; Fontaine et al., 2004; Wang et al., 2001). Observation of thrombus reveals that three types of thrombus exist (Fig. 1.2) (Wang et al., 2001). New thrombus tissue is formed at the luminal side and appears red. Fibrin fibres are clearly identifiable, arranged into primary, thick fibrin bundles and a fine secondary cross linking structure. Attached to this thrombus is a more aged region, which appears white to yellow. Fibres in this regions have degenerated. In the abluminal region, the thrombus has aged the most, all fibres appear degenerated, and no structure can be recognised (Wang et al., 2001).

Although a thrombus generally exists of luminal, medial and abluminal thrombus, not all the different types are present in each patient. Additionally, some of the layers are not suitable for the harvesting of samples. Samples which are needed for the determination of the mechanical properties, cannot be cut from the abluminal thrombus because it is too degenerated. The abluminal thrombus is therefore not taken into account in the rest of this study.

With respect to transitions from luminal to medial tissue the thrombi used in this study can roughly be divided into a discrete transition group and a continuous transition group. In the discrete transition group the luminal, medial and abluminal thrombus are not or at most weakly attached to each other. The luminal thrombus appears very red and weak, while the medial thrombus is a yellow gel-like structure (Fig.

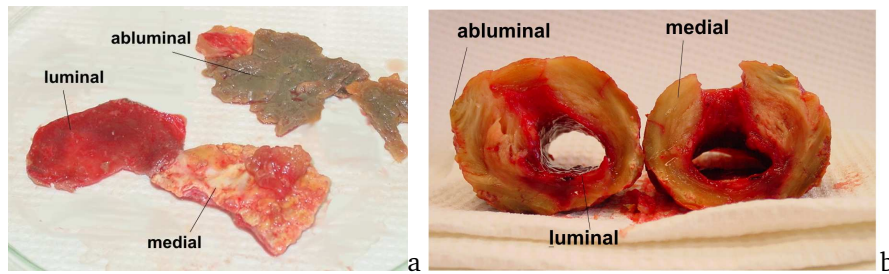


Figure 2.1: Discrete (a) and continuous (b) material transitions in a thrombus. In the discrete situation luminal (left), medial (bottom) and abluminal (top right) regions are clearly identifiable. The transversal cross-section of continuous thrombus shows that there is a gradual change in the tissue type.

2.1a). The mechanical properties of the luminal and medial tissue of this type of thrombus are expected to differ considerably, as was already reported for tensile testing by Wang et al. (2001).

Thrombi that show a continuous transition (Fig. 2.1b) consist of multiple layers that still form a single structure. The layers of this type of thrombus are firmly attached to each other and the transition of the luminal to the medial region is spread over several layers. The differences in mechanical properties between luminal and medial regions are expected to be smaller for the continuous transition thrombus than for the discrete transition thrombus. In the continuous transition thrombus the mechanical properties are expected to change gradually. The transition from medial to abluminal regions is also continuous and the amount of the abluminal tissue, which is not studied in this work, is in general less than in the discrete transition thrombus.

In the *in vivo* situation thrombi undergo large deformations and it would therefore be necessary to study nonlinear behaviour, which would require performing large strain experiments. Before doing so, in this work the applicability of rheometry to obtain the viscoelastic properties of thrombus is evaluated by studying the linear viscoelastic behaviour. To achieve this goal, oscillatory shear experiments are applied to samples from thrombi with either a discrete or continuous tissue transition. Since shear experiments are sufficient to determine the linear viscoelastic properties our study was limited to these measurements. The differences in mechanical properties between the distinct layers in the discrete transition thrombus are studied as well as the changes of the properties throughout the layers of the continuous transition thrombi. Finally, the results from the discrete and continuous groups will be compared.

2.2 Methods and Materials

2.2.1 Methods

To determine the linear viscoelastic properties, shear experiments were performed. Experimental methods are based on standard procedures and on previous research in our group on the viscoelastic properties of other soft tissues, such as brain (Brands et al., 1999; Hrapko et al., 2006) and muscle (van Turnhout et al., 2005). All experiments were performed using a Rheometrics rotational rheometer (Advanced Rheometric Expansion System (ARES), Rheometrics Scientific, USA) with controlled strain mode with a parallel plate geometry in combination with a Peltier environmental control and a fluid bath.

Linear viscoelastic material behaviour is described by a multi mode Maxwell model (Macosko, 1994):

$$\dot{\tau}_i + \frac{1}{\lambda_i}\tau_i = G_i\dot{\gamma}, \quad (2.1)$$

where τ_i is the shear stress contribution of mode i with the relaxation time λ_i and modulus G_i . $\dot{\gamma}$ is the applied strain rate. The total stress (τ) is the sum of the stress contributions of all (n) modes:

$$\tau = \sum_{i=1}^n \tau_i, \quad (2.2)$$

A frequency (ω) dependent input $\gamma = \gamma_0 \sin \omega t$ will lead to a sinusoidal shear stress

$$\tau = G_d \gamma_0 \sin(\omega t + \delta), \quad (2.3)$$

where G_d is the dynamic modulus and δ the phase shift. The response can be written in an in-phase and out-of-phase wave: $\tau = \tau' + \tau'' = \tau'_0 \sin \omega t + \tau''_0 \cos \omega t$. From this one can compute the moduli

$$G' = \tau'_0 / \gamma_0 = \sum_{i=1}^n G_i \frac{\lambda_i^2 \omega^2}{1 + \lambda_i^2 \omega^2} \quad (2.4)$$

$$G'' = \tau''_0 / \gamma_0 = \sum_{i=1}^n G_i \frac{\lambda_i \omega}{1 + \lambda_i^2 \omega^2} \quad (2.5)$$

where G' is the storage modulus, representing the elastic part of the behaviour and G'' is the loss modulus, representing the viscous part of the behaviour. The two moduli, G' and G'' , form the complex dynamic modulus $G_d = G' + iG''$. The phase shift δ is a measure of viscous versus elastic material behaviour and is related to Eqn. (2.4) and (2.5) as follows

$$\tan \delta = \frac{G''}{G'}. \quad (2.6)$$

All shear experiments should be performed in the linear viscoelastic regime of the tissue. The linear regime is the strain range in which the material properties are assumed to be constant. This regime is determined using oscillatory shear experiments with constant frequency and varying strain (strain sweep). A constant strain within this linear regime is chosen for the subsequent frequency sweeps. The frequency in the latter experiments is increased stepwise from 0.1 to 100 rad/s.

2.2.2 Discrete transition group

All thrombi were obtained from patients undergoing elective surgical AAA repair. Because this material is normally discarded and it is anonymised after the procedure, making it impossible to trace it back to the patient, informed consent was not required. The procedure was in conformity with the code of conduct for use of human material as stated by the Dutch federation of Biomedical Scientific Societies.

Tissue was stored in saline at 4°C immediately after being removed from the patients and tested within 24 hour after harvesting. The thrombus was peeled into thin layers (about 2 mm thickness). Cork drills of 10 and 14 mm diameter were used to cut samples from both the luminal and medial thrombus layers, from regions with (as far as could be determined) constant thickness. Thrombus in the discrete transition group was obtained from 4 different patients (referred to as patients 1 through 4). A total of 7 luminal samples from these 4 patients was obtained, while a total of 4 medial samples from 3 patients (patient 1, 3 and 4) was used. From patient 2 no sufficiently flat medial thrombus samples could be produced. Frequency sweeps were applied to the samples from patient 1 and 2. The initial intention was to perform all experiments at 37°C, but due to failing temperature control equipment at the time the tissue was available, only one measurement was performed at 37°C. The rest of the experiments was performed at room temperature.

When the Time-Temperature Superposition (TTS) principle is applicable to the tissue, data can be shifted to and from a reference temperature (Macosko, 1994). The isothermal characteristic, G_d (and also G' and G''), can be shifted along the horizontal and vertical axis to a reference temperature T_0 :

$$G_d(\omega, T) = \frac{1}{b_T} G_d(a_T \omega, T_0). \quad (2.7)$$

with the horizontal shift factor a_T and vertical shift factor b_T . The TTS principle is valid when one smooth curve mastercurve can be obtained by shifting the frequency sweep curves obtained at different constant temperatures horizontally and vertically to the curve obtained at the reference temperature until all curves overlap. When no smooth master curve can be obtained the TTS principle is invalid.

The frequency shift used to shift each dataset to the mastercurve can be plotted against the temperature at which the dataset was acquired. The result can be described with an Arrhenius function:

$$a_T = A e^{-E_a/RT} \quad (2.8)$$

where A is a constant, E_a is the activation energy, R is the universal gas constant and T the temperature. This results in the horizontal shift factor a_T . The vertical shift factor, b_T , is obtained in a similar way. After obtaining the shift factors the TTS principle can be used to shift data sets to or from a reference temperature by shifting them along the horizontal and vertical axes, applying horizontal shift factor a_T and vertical shift factor b_T according to (Eqn. 2.7).

To show the applicability of the TTS principle to thrombus tissue a total of 6 samples from 2 patients (patients 3 and 4) was used, 3 samples of which were from the luminal region, and 3 from the medial region. After repair of the temperature control equipment, frequency sweeps for these samples were measured at 5°C, 20°C, 35°C and 40°C. Room temperature (20°C) was chosen as the reference temperature for the mastercurve. Samples from 1 patient were also measured at 10°C, 15°C, 25°C and 30°C.

The frequency sweep curves of patient 3 and 4 performed at 20°C were added to the data in the discrete transition group. The shift factors a_T and b_T obtained were used to shift all data sets in the discrete transition group to 37°C.

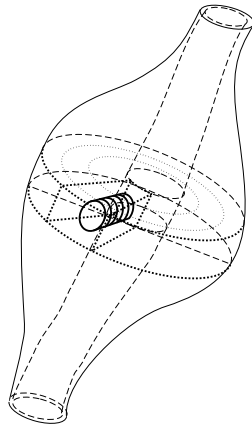


Figure 2.2: Schematic view of the sample orientation in the continuous transition thrombus.

2.2.3 Continuous transition group

Since the layers of thrombus of the continuous transition type are hard to classify in the luminal and medial regions, slices of 0.5 mm thickness were cut from the thickest part of the thrombus using a vibratome (VS1000s, Leica microsystems, Germany), going from the abluminal to the luminal side of the thrombus (Fig. 2.2). Cork drills, 10 mm diameter, were used to cut samples from all slices. Since this sample preparation is time-consuming, measurements had to be postponed and samples were stored temporarily at -80°C. To verify that the storage did not influence the mechanical prop-

erties, 6 fresh samples from 2 patients were tested both before and after freezing. The samples were thawed in a lukewarm bath before experiments at 37°C were performed. Because the original position of the samples within the thrombus is known, a possible gradual change of the mechanical properties throughout the thrombus can be studied. For this purpose G' and G'' were measured for samples of all slices.

2.3 Results

The results for the discrete and the continuous transition group will be presented successively. The elastic modulus G' will be shown for all experiments. G'' shows similar trends as G' and is not presented for all measurements to limit the number of figures. The values of G'' do, however, represent the viscous part of the viscoelastic behaviour and are shown for the frequency sweep tests that are needed to determine the viscoelastic behaviour of the thrombus.

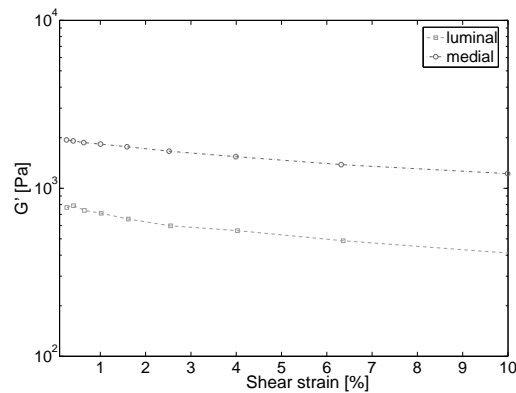


Figure 2.3: Strain sweep: mean G' of luminal and medial layers. The behaviour is assumed (within good approximation) to be linear at 3% strain.

2.3.1 Discrete transition

In figure 2.3 typical curves for luminal and medial strain sweep curves are shown. The behaviour of both luminal and medial samples is assumed to be linear at strains higher than 2%. G' decreases slowly and to assure measurements are done within the linear regime, a constant strain of 3% has been chosen for the frequency sweep measurements.

To test the applicability of the Time Temperature Superposition principle, the G' curves for different temperatures were shifted to the reference curve at 20°C. The resulting curves of G' have well overlapping areas and form a smooth master curve.

It can be readily assumed that the Time-Temperature Superposition principle is applicable to thrombus tissue. The shifting required a vertical (Fig. 2.5b) and a horizontal (Fig. 2.5a) shift factor. The vertical shift factor, b_T , was always close to 1 and therefore will be assumed to be 1 in the rest of this study. The mean value of the horizontal shift factor a_T was fitted with an Arrhenius function (Eqn. (2.8)), which yielded $a_T = 0.29$. Data obtained at 40°C were excluded from further examination because of errors caused by possible protein degradation at this temperature. All frequency sweeps performed at room temperature were shifted to 37°C by multiplying the frequencies by the fitted horizontal shift factor.

In figure 2.6 the results of the frequency sweep test on luminal thrombus are shown.

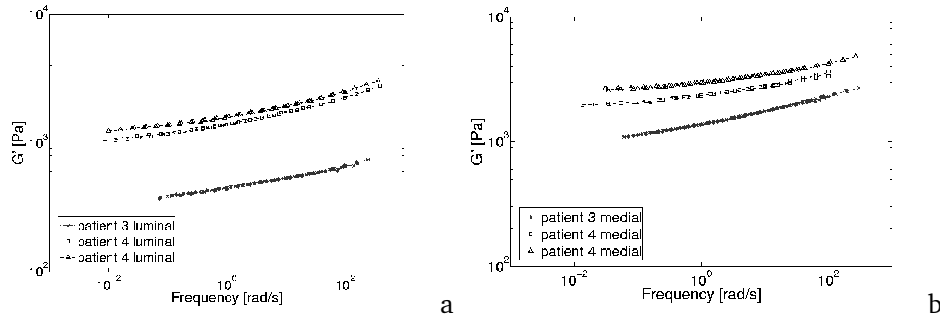


Figure 2.4: Time Temperature Superposition: G' Master curve for luminal (a) and medial (b) thrombus.

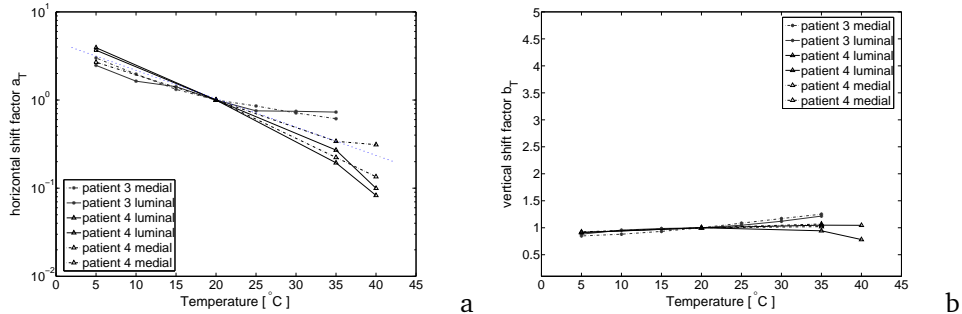


Figure 2.5: Time Temperature Superposition: horizontal shift factor a_T (a) with the fitted Arrhenius function (dotted line) and vertical shift factor b_T (b).

For all the samples from 4 different patients G' increases with frequency in a similar manner (Fig. 2.6a). Typically, the minimal and maximal values differ by ≈ 1 kPa. G'' (Fig. 2.6b) also increases with frequency for all samples and the slope is similar to

that for G' , but the level is considerably lower (<300 Pa). G' for the medial samples (Fig. 2.7a) ranges between 1-3 kPa. Again, G'' increases similarly (Fig. 2.7b) at a level which is equal to that of G'' in luminal thrombus.

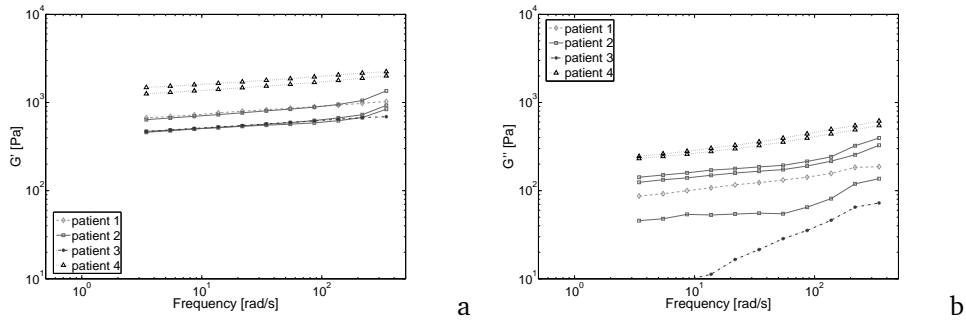


Figure 2.6: Luminal thrombus: frequency dependency of G' and G'' .

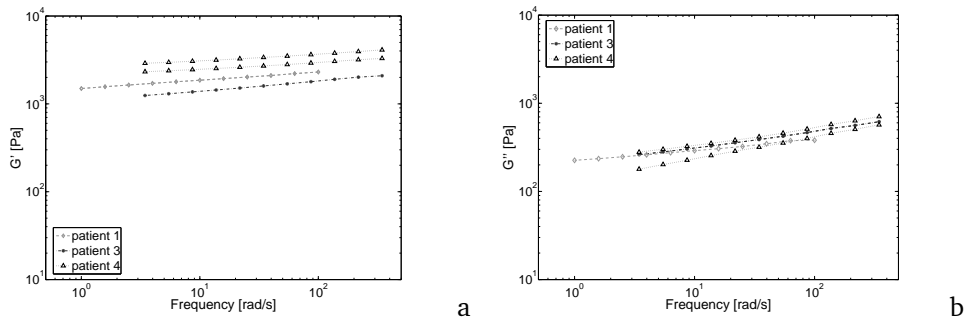


Figure 2.7: Medial thrombus: frequency dependency of G' and G'' .

2.3.2 Continuous transition

The effect of freezing was tested for 6 samples of 2 patients. Although the value for G' changes for all samples we have tested before and after freezing (Fig. 2.8), they are all of the same order of magnitude. Mean G' before freezing was 1.8 ± 0.5 kPa. After the freezing and thawing it was 2.2 ± 0.8 kPa. The maximum change of G' was -1.4 kPa (Fig. 2.8, sample 1), the minimum change was -0.14 kPa (Fig. 2.8, sample 5). The frequency dependency was not affected by the freezing. The observed variations are acceptable considering the variations between thrombi.

In figure 2.9 the results for G' at 10 rad/s for 3 patients are plotted against the relative position of the sample in the thrombus. 10 rad/s is the logarithmic mean

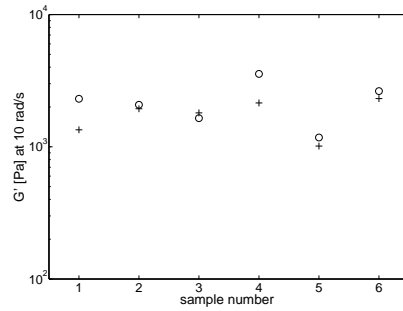


Figure 2.8: Effect of freezing and thawing. G' at 10 rad/s of fresh samples(+) and after freeze storage (o). Samples 1 to 3 are from a different patient as samples 4 to 6.

of the frequency range, which covers the entire physiological frequency range. In the relative position of the sample in the thrombus, position 0 corresponds to the abluminal side, while position 1 indicates the luminal side. Except for one datapoint in the curve of patient 6 (at a relative position of approximately 0.6), G' changes smoothly throughout the thrombus. For all 3 patients the G' values are of the same magnitude and show a similar decline towards the luminal side. The values for G'' do not change throughout the thrombus.

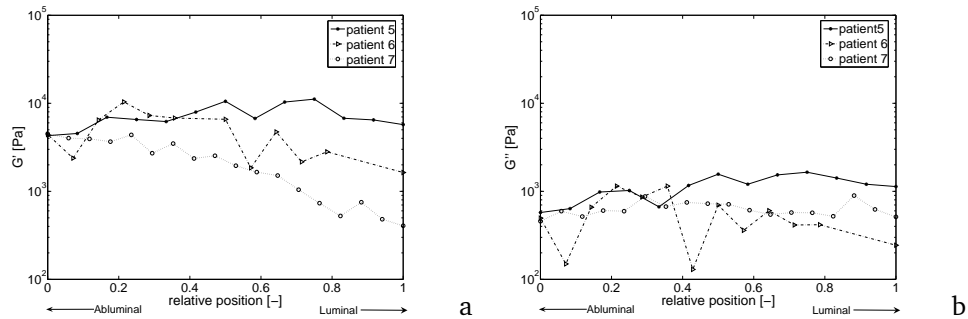


Figure 2.9: Continuous transition thrombus: Gradual change in G' throughout the thrombus. G' (a) and G'' (b) is plotted against the dimensionless position of the sample within the thrombus, 0 indicates the abluminal side, 1 indicates the luminal side of the thrombus.

2.4 Discussion

In most patients intraluminal thrombus is a layered structure. The tissue was divided into three groups, the luminal thrombus, the medial thrombus and the degenerated

abluminal thrombus. This last type of thrombus shows no structure at all, is not suited for preparation of samples and is for that reason not included in this work. In some thrombi the luminal and medial thrombus are clearly recognisable as separate layers with different structures. This type of thrombus is defined as a discrete transition thrombus. The thrombus that consists of one layered piece of tissue is called a continuous transition thrombus.

Although the mechanical properties of the abluminal thrombus may be negligible compared to those of the luminal and medial thrombus, abluminal thrombus is an important factor in the mechanics of the vessel wall-thrombus interaction. It is responsible for the attachment of the thrombus to the wall. The nature of the thrombus-vessel wall contact is unclear to the authors, and will be a subject of further study.

Although the discrete and continuous transition thrombi are treated as separate groups, the results of the two groups show identical trends. In figure 2.10 the mean \pm standard deviation of G' values of all luminal (Fig. 2.6) and all medial (Fig. 2.7) samples of the discrete transition group at 10 rad/s are depicted. When these are compared to G' values for the continuous transition group, it is clear that G' tends to be lower for samples near the lumen in both groups. Although the average values for the discrete group are lower than for the continuous group they are all in the same order of magnitude. This could suggest that the application of the same material model for both groups would be sufficient. More data, however, are needed to support this idea.

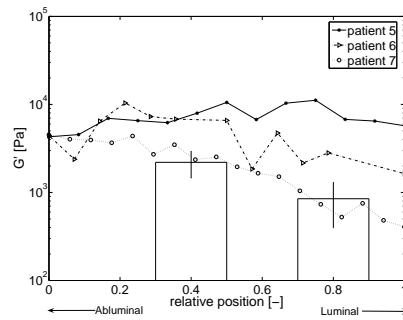


Figure 2.10: Discrete and continuous transition thrombus. A combination of figure 2.9 and G' values at 10 rad/s from the discrete transition group. The luminal layer error bar is plotted at distance 0.8 (near the lumen), the medial layer at 0.4.

The phase angle, δ , is a measure for viscous versus elastic material behaviour and is related to G' and G'' (Eqn. 2.6). In purely elastic behaviour, δ is 0° , whereas δ is 90° in purely viscous behaviour. For the discrete and the continuous thrombus, the mean and standard deviation of δ was 8.9 ± 4.2 and 14.7 ± 13.1 respectively. It can be concluded that the elastic part of the behaviour dominates the viscous part. Although the viscous part is small compared to the elastic part it may play an important role in the attenuation of pressure waves travelling through the arterial system.

For the continuous thrombus the G' at 10 rad/s was shown to change gradually

throughout the thrombus. For 1 patient one solitary jump in G' can be seen in the curve. Because of the solitary character of the point in the curve, it is assumed that the deviation is caused by a measurement error.

The expected differences between the material properties of the luminal and medial layers of the discrete transition thrombus are confirmed by results obtained from frequency sweep experiments. It was found that the storage modulus G' for luminal discrete transition thrombus within each patient is lower than for the medial region. In contradiction to our results, Wang et al. (2001) concluded from uniaxial tensile testing that luminal thrombus is significantly stiffer. They related this to the structural state of the tissue. Differences in the division of tissue in the medial or luminal region would account for some differences in the observed mechanical properties but do not explain the opposite relation of mechanical properties found in the luminal and medial regions. In their study (Wang et al., 2001) the thrombus was clamped and uniaxially stretched up to a ratio of 2.5, a value that will not be reached physiologically and makes a comparison to our 3% strain experiments meaningless. Furthermore, the inaccuracy that rises from measuring width and thickness of the sample in uniaxial testing does not occur in the shear measurements we performed. Additional advantages of our method are the facts that no clamping is required, and that the temperature can be controlled during the experiments.

The measurements at the limiting temperatures of the chosen range (5-40°C) in the time-frequency superposition measurements sometimes lead to unreliable results and, therefore, these 40°C-measurements have not been considered further. Moreover, the measurement at 5°C had to be discarded. The applicable temperature range is physically bounded by phase transitions at low temperatures and the solidifying of proteins above 41°C. Results have, however, shown that the applicable temperature range is more narrow. Mechanical properties measured at any temperature can be shifted to 37°C by applying the Time-Temperature Superposition principle. It is, however, strongly recommended to avoid the boundaries of the temperature range.

The variation on results between patients, which is not unexpected, can be attributed to several factors. First of all, the age of the thrombus is not known. During ageing the initial platelet rich blood clot is first enmeshed by a fibrin structure, followed by degradation of this fibrin structure (Falk, 1992). For the luminal thrombus, it is only known that it is formed most recently, but the actual stage of ageing and the subsequent state of the structure is expected to have a great influence on the mechanical properties.

Secondly, the exact shape and thickness of the thrombus is different for each patient and the original position of the thrombus in the aneurysm is not known. To study the influence of shape, thickness and original position it would be interesting to involve CT or MR patient data in to this research. Even if these data were available it should still be remembered that some inter subject variations will always be found.

The computational model of Inzoli et al. (1993) which included the thrombus in the stress calculations of the vessel wall concluded that a thick thrombus with a Young's modulus of 0.2 MPa decreases the peak wall stress most. Mower et al. (1997) varied stiffness from 0.01-2.0 MPa and found that a low thrombus stiffness hardly leads to maximal stress reduction. Values found in this study are, however, lower and it

will therefore be interesting to study whether the presence of a thrombus with the measured viscoelastic properties will influence the wall stress. Before thrombus can be included in our patient specific model (Wolters et al., 2005), the actual mechanical properties need to be described for the entire relevant bandwidth. This can be done by fitting a multi-mode Maxwell model to the experimental results. To obtain statistically tested model parameters the methodology first needs to be applied to a sufficient number of thrombi.

Since the experimental methods are known to lead to reproducible results, the method may, in future work, be extended to the non-linear regime to deal with the large strains that appear in a thrombus (Vorp et al., 1996).

2.5 Conclusion

It has been shown that determination of the viscoelastic properties of thrombus is possible. Time-Temperature Superposition is applicable to thrombus tissue. Although not statistically proved, it is suggested that in a discrete transition thrombus, the mechanical properties of luminal and medial areas cannot be assumed to be equal. In the continuous transition thrombus the changes in mechanical properties are gradual. Values for discrete transition and continuous transition thrombi are all in the same order of magnitude.

Chapter 3

Non-linear Viscoelastic Behaviour of Abdominal Aortic Aneurysm Thrombus

This chapter is based on: EA van Dam, SD Dams, GWM Peters, MCM Rutten, GWH Schurink, J Buth, FN van de Vosse, *Non-linear Viscoelastic Behavior of Abdominal Aortic Aneurysm Thrombus*, Biomech Mod Mechanobiol, in press, 2007.

3.1 Introduction

Rupture of an abdominal aortic aneurysm (AAA) is a life threatening event, that can, when diagnosed in time, be prevented by either conventional or endovascular repair. Since these corrections are accompanied by mortality rates of 4.0% and 2.9% respectively (Hua et al., 2005), a careful evaluation of the rupture risk versus the risk of surgical intervention is required. Currently, rupture risk prediction is based on the maximum diameter of the aneurysm. However, it has been shown already that small aneurysms do rupture sometimes, while some large aneurysms have not ruptured yet, and therefore the diameter criterion alone may not be sufficient. Since the aneurysm wall ruptures when stress exceeds the strength of the vessel wall (Fillinger et al., 2003), stress analyses of the AAA vessel wall by means of a Finite Element Method (FEM), have become subject of several studies (di Martino et al., 1998; Fillinger et al., 2002; Inzoli et al., 1993; Mower et al., 1997; Raghavan et al., 2000; Thubrikar et al., 2001a; Wang et al., 2002; Wolters et al., 2005).

AAAs are lined with intraluminal laminated thrombus to a varying extent. The effect of the presence of thrombus on the wall stress has been studied on both idealised (di Martino et al., 1998; Inzoli et al., 1993; Mower et al., 1997) and patient specific geometries (di Martino and Vorp, 2003; Wang et al., 2002). Thrombus is found to reduce and redistribute wall stress. The size of the effect is dependent on the geometry and the mechanical properties of the thrombus.

Thrombus is a fibrin structure infiltrated with blood cells, blood proteins and cellular debris (Falk, 1992). Observation of thrombus (van Dam et al., 2006; Wang et al., 2001) reveals that three types of thrombus exist (Fig. 1.2). New thrombus is formed at the luminal side and appears red. Fibrin fibres are clearly identifiable and arranged into primary, thick fibrin bundles and a fine, secondary, cross linked structure. Attached to this thrombus is a more aged region, which appears white. Fibrin fibres in this regions have degenerated. In the abluminal region, the thrombus has aged most and all fibres appear degenerated, no structure can be recognised (Wang et al., 2001).

Figure 3.1b shows ESEM images, obtained in our lab, of the transversal plane through three different human AAA thrombi. The abluminal thrombus is at the right side of the image, luminal at the left side of the images. In the first thrombus, the local differences in structure are large. The structure is very dense in some positions, whereas it is very loose in others. The structure of the other two thrombi seems to be much more homogeneous, but still differences between areas can be pointed out. Wang et al. (2001) related the mechanical properties of the luminal and medial thrombus to their structural state and reported a difference between the layers. The ESEM images in figure 3.1b, however, do not show clear distinction between the luminal, medial and abluminal layers, but do show large local variations. This may indicate that local variations can also occur in the mechanical properties.

The effects of local differences in structure were, however, neglected in the wall stress analyses concerned. The thrombus was modelled as an isotropic homogeneous material in all studies; the mechanical properties were either assumed (Inzoli et al., 1993; Mower et al., 1997) or were determined by fitting tensile testing data to a linear

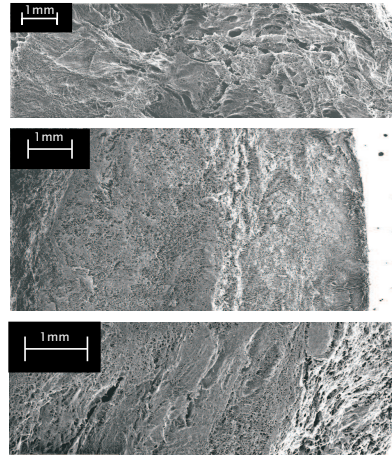


Figure 3.1: In ESEM images of thrombus of 3 patients no large structural change can be found throughout the thrombus. At the left the luminal thrombus, at the right the abluminal thrombus.

elastic model (di Martino et al., 1998) or to a two-parameter, hyper-elastic, isotropic and incompressible model (Wang et al., 2001, 2002). An ideal model for calculating AAA wall stresses would include loading with a dynamic pressure and applying a proper constitutive model that also incorporates the position dependent viscoelastic properties of the thrombus.

It has been shown in previous studies that rheological measurements yield reproducible results for linear viscoelastic behaviour, which is valid for small strains up to 5% (Hinnen et al., 2007; van Dam et al., 2006). Large strains can, however, appear in thrombus (Vorp et al., 1996). When the change of shape of *in vivo* AAAs during systole was studied based on MR images inner, circumferential strains up to 15% were revealed. Since linear viscoelastic behaviour is only applicable to small strains, the goal of this study is to determine the non-linear viscoelastic behaviour of the thrombus and to study the changes in mechanical properties throughout the thickness of the thrombus caused by structural changes as described by Wang et al. (2001).

To achieve this goal, first a non-linear viscoelastic material model is presented that can capture the phenomena observed experimentally. To obtain the model parameter values, results of experiments in both the linear and the non-linear regime are needed. The changes in the linear behaviour throughout the thickness of the thrombus, that may be caused by structural changes, will be shown. Although the oscillatory shear experiments were performed earlier (van Dam et al., 2006), they were repeated for a larger number of samples and the experimental methods were extended to the non-linear regime. Stress relaxation experiments are performed to obtain the non-linear model parameters.

3.2 Methods

3.2.1 Kinematics

The changes of volume and shape of an arbitrary solid material are described by the deformation gradient tensor \mathbf{F} . \mathbf{F} is split (Fig. 3.2) into an elastic part, \mathbf{F}_e , and an inelastic part \mathbf{F}_p :

$$d\mathbf{x} = \mathbf{F} \cdot d\mathbf{x}_0; \quad \mathbf{F} = \mathbf{F}_e \cdot \mathbf{F}_p, \quad (3.1)$$

where $d\mathbf{x}_0$ represents a material line element in the undeformed state, C_0 , and $d\mathbf{x}$ represents it in the deformed state, C_t . The inelastic part of \mathbf{F} , \mathbf{F}_p , transforms the undeformed state, C_0 , to a relaxed stress-free configuration, C_p . This is a fictitious state that would be recovered instantaneously when all loads were removed from the material line-element. The elastic part, \mathbf{F}_e , of \mathbf{F} transforms the stress-free state, C_p , elastically into the deformed state, C_t . Next, the elastic Finger tensor, \mathbf{B}_e , can be introduced:

$$\mathbf{B}_e = \mathbf{F}_e \cdot \mathbf{F}_e^T \quad (3.2)$$

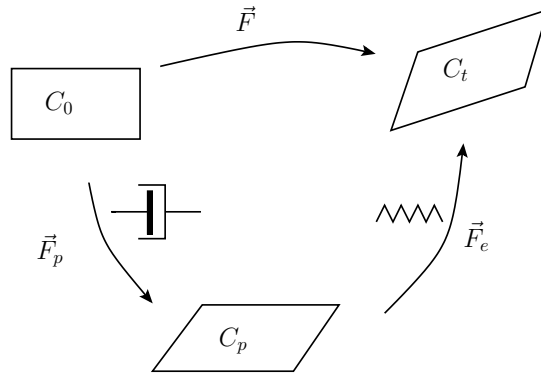


Figure 3.2: The inelastic part of \mathbf{F} , \mathbf{F}_p transforms the undeformed state C_0 to a relaxed stress-free configuration, C_p and is modelled by a dashpot. C_p is a fictitious state that would be recovered instantaneously when all loads were removed from the material element. The elastic part, \mathbf{F}_e , of \mathbf{F} transforms the stress-free state C_p elastically into the deformed state C_t . This part is modelled by a spring.

The velocity gradient tensor can be defined as:

$$\mathbf{L} = \dot{\mathbf{F}} \cdot \mathbf{F}^{-1}. \quad (3.3)$$

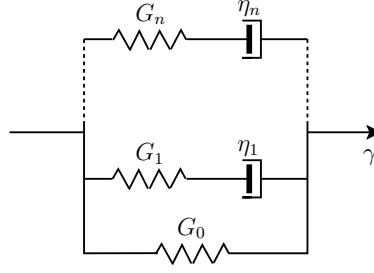


Figure 3.3: A spring-dashpot model as a mechanical analog of the constitutive model. The springs G_1 through G_n and the dashpots in the viscoelastic modes are linear. The equilibrium mode is modelled by a non-linear spring G_0 .

Using Eqn. (3.1) and (3.3) an additive decomposition of \mathbf{L} is defined:

$$\mathbf{L} = \mathbf{L}_e + \mathbf{L}_p,$$

$$\mathbf{L}_e = \dot{\mathbf{F}}_e \cdot \mathbf{F}_e^{-1}, \quad \mathbf{L}_p = \mathbf{F}_e \cdot \dot{\mathbf{F}}_p \cdot \mathbf{F}_p^{-1} \cdot \mathbf{F}_e^{-1}. \quad (3.4)$$

Both parts of the velocity gradient can be decomposed in:

$$\begin{aligned} \mathbf{L}_e &= \mathbf{D}_e + \boldsymbol{\Omega}_e, & \mathbf{D}_e &= \frac{1}{2}(\mathbf{L}_e + \mathbf{L}_e^T), & \boldsymbol{\Omega}_e &= \frac{1}{2}(\mathbf{L}_e - \mathbf{L}_e^T) \\ \mathbf{L}_p &= \mathbf{D}_p + \boldsymbol{\Omega}_p, & \mathbf{D}_p &= \frac{1}{2}(\mathbf{L}_p + \mathbf{L}_p^T), & \boldsymbol{\Omega}_p &= \frac{1}{2}(\mathbf{L}_p - \mathbf{L}_p^T) \end{aligned} \quad (3.5)$$

where \mathbf{D}_e and \mathbf{D}_p are the symmetric rate of deformation tensors and $\boldsymbol{\Omega}_e$ and $\boldsymbol{\Omega}_p$ are the skew-symmetric spin tensors. To obtain a unique fictitious stress free state, \mathbf{C}_p , the inelastic deformation is assumed to occur spin free:

$$\boldsymbol{\Omega}_p = 0. \quad (3.6)$$

The elastic part of the deformation must then account for all rotations:

$$\boldsymbol{\Omega}_e = \boldsymbol{\Omega}. \quad (3.7)$$

3.2.2 The constitutive model

The constitutive model proposed is based on previous research on the viscoelastic properties of brain tissue (Hrapko et al., 2006).

Since thrombus can be assumed to be incompressible (Hinnen et al., 2007), the Cauchy stress can be split:

$$\boldsymbol{\sigma} = \boldsymbol{\sigma}^d + \boldsymbol{\sigma}^v, \quad (3.8)$$

where σ^v is the volumetric part, that only depends on the hydrostatic pressure ($p = -\frac{1}{3}\text{tr}(\sigma)$), and $\sigma^d = \sigma - p\mathbf{I}$ is the deviatoric part. The latter part is decomposed into an elastic part, σ_0^d and into n viscoelastic modes (Fig. 3.3):

$$\sigma^d = \sigma_0^d + \sum_{i=1}^n \sigma_i^d. \quad (3.9)$$

The elastic behaviour of the viscoelastic modes is modelled as being Neo-Hookean :

$$\sigma_i^d = G_i \mathbf{B}_{e,i}^d, \quad (3.10)$$

where $\mathbf{B}_{e,i}^d$ is the deviatoric part of the elastic Finger tensor \mathbf{B}_e of mode i . The time dependent behaviour of the viscoelastic modes is described by the inelastic rate of deformation, \mathbf{D}_p :

$$\mathbf{D}_{p,i} = \frac{\sigma_i^d}{2\eta_i} \quad (3.11)$$

with $\eta_i = G_i \lambda_i$. This is equivalent to a Leonov model; a nonlinear model that is fully characterised by the linear parameters G_i and λ_i only. In the limits of small strains this model reduces to a Maxwell model.

A non-linear equilibrium mode is added to the viscoelastic modes. This mode is described by a Mooney-Rivlin-type model, modified with a damping function:

$$\sigma_0^d = 2 \frac{\partial W}{\partial I_1} \mathbf{B}^d - 2 \frac{\partial W}{\partial I_2} (\mathbf{B}^{-1})^d, \quad (3.12)$$

with $W = W(I_1, I_2)$ the strain energy function, where I_1 and I_2 are the first and second invariants of the Finger tensor:

$$I_1 = \text{tr}(\mathbf{B}); \quad I_2 = \frac{1}{2} [\text{tr}(\mathbf{B})^2 - \text{tr}(\mathbf{B}^2)]. \quad (3.13)$$

The shape of the partial derivatives of the strain energy function is chosen based on the non-linear strain-dependency of the equilibrated response as is observed in shear relaxation tests:

$$W = G_0 \left\{ -\frac{1-A}{C^2} [(Cx+1)\exp(-Cx) - 1] + \frac{1}{2} Ax^2 \right\}, \quad (3.14)$$

with

$$x = \sqrt{bI_1 + (1-b)I_2 - 3} \quad (3.15)$$

and A , C and b material specific parameters. With this strain energy function, the constitutive relation for the equilibrium mode can be written as:

$$\sigma_0^d = G_0 [(1-A) \exp(-C\sqrt{bI_1 + (1-b)I_2 - 3}) + A] [b\mathbf{B}^d - (1-b)(\mathbf{B}^{-1})^d]. \quad (3.16)$$

The parameter b distinguishes between the contribution of the first and second invariant of \mathbf{B} to the strain energy and cannot be determined in shear experiments. This parameter is, in absence of other than shear experimental data, set to $b = 1$. Determination of b will be subject of future research by adding compression tests to the experimental methods. Eqn. (3.16) then can be simplified:

$$\sigma_0^d = G_0[(1 - A) \exp(-C\sqrt{I_1 - 3}) + A]\mathbf{B}^d. \quad (3.17)$$

The constitutive model, Eqn. (3.10), (3.11) and (3.17), describes the material behaviour of the individual elements, i.e. the springs and dashpots. In each mode, the behaviour of the springs is described as a function of the isochoric elastic Finger tensor $\mathbf{B}_{e,i}^d$, while the dashpots are described as a function of the inelastic deformation rate, $\mathbf{D}_{p,i}$. For numerical implementation, the kinematics is used to write the behaviour in terms of the inelastic right Cauchy-Green tensor for each mode \mathbf{C}_p :

$$\mathbf{C}_p = \mathbf{F}_p^T \cdot \mathbf{F}_p = \mathbf{F}^T \cdot \mathbf{B}_e^{-1} \cdot \mathbf{F}. \quad (3.18)$$

Taking the time derivative of \mathbf{C}_p and using the requirement of spin-free inelastic deformation, Eqn. (3.6), provides an evolution equation for large rigid-body rotation and translation:

$$\dot{\mathbf{C}}_p = 2\mathbf{C}_p \cdot \mathbf{F}^{-1} \cdot \mathbf{D}_p \cdot \mathbf{F}. \quad (3.19)$$

In the time integration procedure (Brands, 2002), the evolution equation, $\dot{\mathbf{C}}_p$ is used to numerically update \mathbf{C}_p , Eqn. (3.19), in the following way: At each new time increment the updated elastic Finger tensor follows from \mathbf{F} at that time increment and Eqn. (3.18): $\mathbf{B}_e = \mathbf{F} \cdot \mathbf{C}_p^{-1} \cdot \mathbf{F}^T$. Application of \mathbf{B}_e in constitutive equation, Eqn. (3.10), yields an updated σ_i^d . Finally, the inelastic rate of deformation \mathbf{D}_p is determined from Eqn. (3.11) and the subsequently updated $\dot{\mathbf{C}}_p$, Eqn. (3.19), serves as the basis for proceeding to the next step. The evolution equation, $\dot{\mathbf{C}}_p$, is insensitive for large-body rotations (Brands, 2002) and is therefore used to numerically update \mathbf{C}_p . The material parameters, G_0 to G_n , λ_1 to λ_n , A and C , are determined by fitting the proposed model to experimental data as will be described in the next section.

3.2.3 Determination of material parameters

Sample preparation

Thrombus tissue was obtained from seven patients undergoing elective surgical AAA repair. Because this material is discarded in the normal clinical setting and it is anonymised after the procedure, making tracing back to the patient impossible, informed consent was not required. The procedure was in conformity with the code of conduct for use of human material as stated by the Dutch federation of Biomedical Scientific Societies. Directly after harvesting of the tissue, it was stored in Phosphate Buffered Saline (PBS). The thickest part of the thrombus was selected for preparation

of samples for mechanical testing. A vibratome (VS1000s, Leica microsystems, Germany) with a sapphire knife was used to cut a radially oriented stack of slices (Fig. 2.2), each with a thickness of 0.5 mm. For experiments performed on a plate rheometer, the samples need to be parallel. A cork drill with a diameter of 10 mm was used to cut a sample out of each slice. Since this sample preparation is time-consuming, measurements had to be postponed and samples were stored at $-80\text{ }^{\circ}\text{C}$. In a previous study it was verified that this storage did not influence the mechanical properties (van Dam et al., 2006). Before testing, the samples were thawed in a bath with lukewarm water.

Experimental setup

All small strain and large strain experiments were performed on a Rheometrics rotational rheometer (ARES, Advanced Expansion System) with parallel disk geometry in combination with a Peltier Environmental control and a fluid bath. All measurements were performed at $37\text{ }^{\circ}\text{C}$ in a PBS saturated humid environment.

To avoid compression to be applied during the shear experiments, the exact thickness of each sample was determined. The gap between the plates needs to be equal to this thickness. To this end, the upper plate is positioned above the sample and is then lowered with a constant velocity, while measuring the normal force. A typical representation of this procedure, called the force gap test, is given in figure 3.4, where the normal force is plotted as a function of the gap width during the force gap test. Samples are saturated with PBS, which will form a layer of liquid on top of the sample. When the upper plate nearly contacts the fluid, capillary effects will cause a negative normal force. When the plate is lowered further and reaches the sample top, the normal force will have increased again to zero. Evidently, the normal force will increase rapidly when the upper plate is lowered even further and compresses the sample.

Small strain experiments

For small strains, the non-linear viscoelastic model proposed in the previous paragraphs, reduces to a multi mode Maxwell model. A n -mode Maxwell model is fully determined by the relaxation time λ_i and moduli G_i ($i=1,\dots,n$) and can be presented in terms of the storage modulus G' and the loss modulus G'' ,

$$G' = G_0 + \sum_{i=1}^n G_i \frac{\lambda_i^2 \omega^2}{1 + \lambda_i^2 \omega^2}, \quad G'' = \sum_{i=1}^n G_i \frac{\lambda_i \omega}{1 + \lambda_i^2 \omega^2} \quad (3.20)$$

where λ_i and G_i are a set of the relaxation time and shear modulus for the i^{th} mode. For a given number of modes the values for G and λ can be acquired by a dynamic frequency sweep test (DFST). In a DFST, harmonic oscillations with a varying frequency at a constant strain are applied. DFSTs were performed with a frequency range of 1 rad/s (0.16 Hz) to 100 rad/s (16Hz) and a constant strain of 3%, which is within

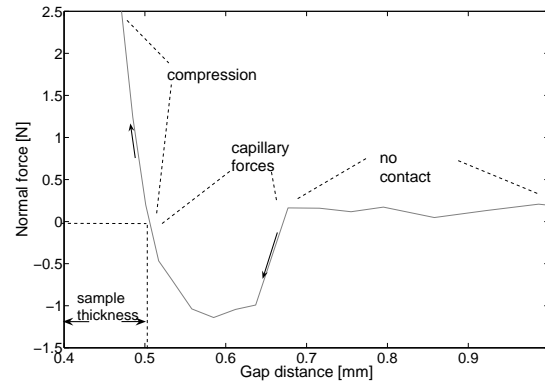


Figure 3.4: Force Gap Test: The gap distance versus the normal force. When the gap distance is decreased, capillary forces will lead to a negative force. When the gap is decreased even further the force will rise through zero and the sample will be compressed. The sample thickness is taken equal to the smallest gap distance at which the normal force equals zero, in this case 0.5 mm.

the linear viscoelastic regime of the thrombus. The applicability of these small shear experiments was shown in previous work (van Dam et al., 2006). In this study, new samples were used to determine the non-linear parameters and to obtain complete datasets these new samples were also tested in the small strain regime. The obtained G' and G'' were used to study the variations within and between thrombi. The original position within the thrombus of each slice plotted against the G' and G'' provide information about the changes of the viscoelastic properties throughout the thrombus. To obtain the differences between thrombi, the mean and standard deviation of G' per thrombus were used. To obtain the general model parameters λ_1 through λ_n and G_0 through G_n , all G' and G'' curves were averaged. Eqn. (3.20) was fitted to these mean G' and G'' curves, with $n=3$, using a least squares estimation algorithm.

Large strain experiments

To determine the model parameters of the non-linear material model described in the previous section, oscillatory experiments can be used. These experiments should then be done at a certain number of frequencies. When, however, stress relaxation experiments are performed information is gathered about all frequencies present within the limits of the experimental setup. During the stress relaxation experiments, a theoretical step in strain is imposed on the sample. Since this is not possible in reality, stress relaxation strain ramps with increasing magnitude (1, 5, 10, 15 and 20%) are imposed with a strain rate of 1s^{-1} (Fig. 3.5). Strain is kept constant thereafter for a loading time of 10 seconds ($\omega < 2\pi/10\text{s} \approx 0.5$). After this loading phase the strain is released and the sample is left to recover at zero strain for 10 times the loading time. Besides the facts that we explore the nonlinear regime and a range of frequencies,

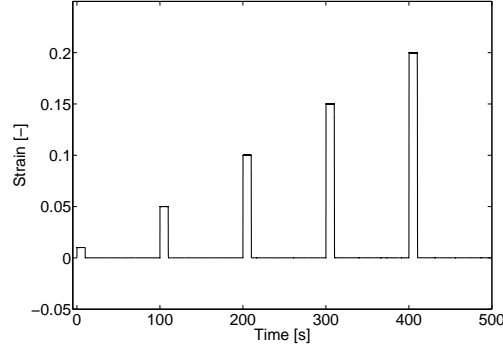


Figure 3.5: Stress relaxation experiments: strain ramps with increasing magnitude are imposed.

these experiments also provide information about reproducibility and the relaxation behaviour.

The evolution equation (3.19) was implemented numerically as described in section 3.2.2 and the model then was fitted to the results from the stress relaxation experiments using a least squares estimation algorithm. The stress responses to the applied strain (Fig. 3.5) of all samples were averaged and the resulting mean stress response was used in the fitting procedure.

Moduli G_1 through G_3 and relaxation times λ_1 through λ_3 , as determined for the linear regime are assumed to be true for the non-linear case as well. Relaxation, however, continues up to 10 seconds, but the small strain experiments do not include such low frequencies. The large relaxation time that is expected from the stress-relaxation experiment can therefore not be found by fitting it solely to the small strain results. A fourth viscoelastic mode, with G_4 and λ_4 , is therefore introduced. Addition of a viscoelastic mode will influence the total G' and G'' (according to Eqn. (3.20)) and therefore G_0 is fitted again. Since G_0 also influences the nonlinear regime (according to Eqn. (3.17)), the fitting routine simultaneously evaluates the parameters for small strains, (Eqn. 3.20), and large strains, (Eqn. 3.19) with the objective function:

$$\epsilon = \frac{1}{n} \sum_{i=1}^n \left(\frac{(G'_{mod}(i) - G'_{exp}(i))^2}{G_{exp}^{\prime 2}(i)} + \frac{(G''_{mod}(i) - G''_{exp}(i))^2}{G_{exp}^{\prime\prime 2}(i)} \right) + \frac{1}{m} \sum_{j=1}^m (\sigma_{mod}(j) - \sigma_{exp}(j))^2 \quad (3.21)$$

where G'_{mod} , G''_{mod} and σ_{mod} are the modelled values and G'_{exp} , G''_{exp} and σ_{exp} the experimental values. G' and G'' are measured (and modelled) at n points, σ is measured at m points. In this objective function errors between the modelled and measured linear data are normalised to experimental values, whereas the non-linear error is not normalised. Normalisation of the non-linear error to the measured value is impossible

because at some measurements points it will lead to divide-by-zero.

3.3 Results

3.3.1 Small strain experiments

To determine the thickness of each sample the force gap test was performed before further testing. The thickness of the samples varied between 0.4 and 0.6 mm. The frequency sweep results show the variations of material properties within and between patients. G' and G'' at 10 rad/s are plotted against the relative position of the sample in the thrombus (Fig. 3.6). Position 0 corresponds to the abluminal side, while position 1 indicates the luminal side. The G' values are all in the same order of magnitude and are within a range of 1.7 ± 1.3 kPa. When studying the change of G' throughout the thickness of each thrombus no similar trend for all patients can be found. The results for G'' are similar: all values are in the same order of magnitude (0.2 ± 0.1 kPa) and no similar trends can be found throughout the thrombus for the different patients. G' of patient 1, e.g., increases towards the abluminal side while G' of patient 2 decreases.

Figure 3.7 depicts the mean and standard deviation of G' and G'' over all samples separately. The values G' and G'' do not differ significantly between patients.

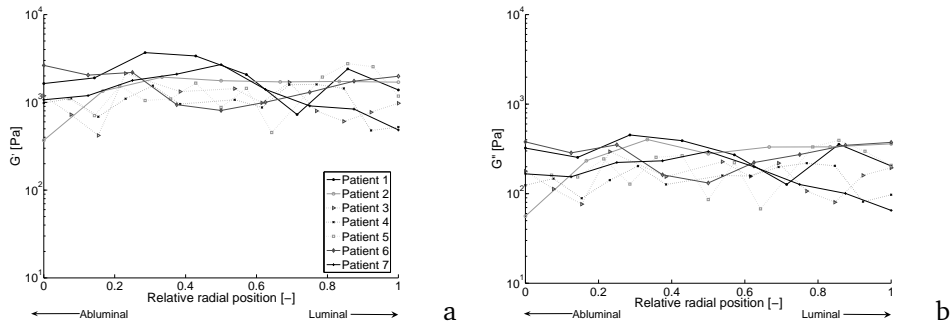


Figure 3.6: G' (a) and G'' (b) at 10 rad/s versus the relative position of each sample in the thrombus: 0 indicates the abluminal side, 1 indicates the luminal side of the thrombus.

The mean and standard deviation of all samples are given versus the frequency in figure 3.8. G' increases with frequency for all samples in a similar way. A Maxwell model with 3 viscoelastic modes and an equilibrium mode was fitted to the mean of all samples. The values for λ_i and G_i are given in table 3.1, the resulting G' and G'' are plotted in figure 3.8. Both fitted G' and G'' are well within the standard deviation of the measured values and the multi mode Maxwell model is therefore assumed to describe the linear material behaviour in a satisfying way.

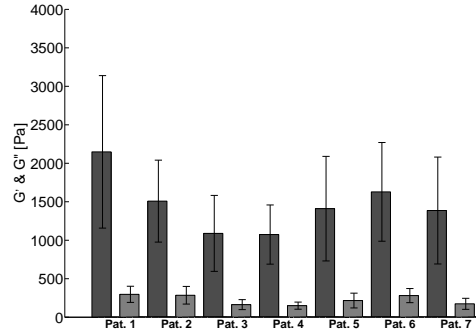


Figure 3.7: The mean and standard deviation of G' and G'' at 10 rad/s of all samples of each patient.

G_0 [Pa]	G_1 [Pa]	G_2 [Pa]	G_3 [Pa]	λ_1 [s]	λ_2 [s]	λ_3 [s]
$9.5 \cdot 10^2$	$5.7 \cdot 10^2$	$2.7 \cdot 10^2$	$2.6 \cdot 10^2$	$9.5 \cdot 10^{-3}$	$9.6 \cdot 10^{-2}$	$9.1 \cdot 10^{-1}$

Table 3.1: Linear model parameters that describe the average G' and G'' .

3.3.2 Large strain experiments

To obtain the parameters for the large strain regime, the stress relaxation experiments as described in section 3.2.3 have been performed. The mean stress response of all samples has been used to obtain the model parameters.

In figure 3.9a the mean stress responses for the 1, 5, 10, 15 and 20% strain are given (from bottom to top respectively). Datapoints in the loading phase and the relaxation were used simultaneously to fit to the model. In the unloading phase too few datapoints were gathered, due to experimental limitations, to determine material properties.

In figure 3.9b, the same experimental data are presented as in figure 3.9a as a stress-strain curve. It can be seen that the model can describe the behaviour in the loading and relaxation phase rather good, however, the unloading phase is not described very well. The predicted relaxation is faster than the measured relaxation. Since a fourth viscoelastic mode is added and G_0 is estimated again, the values for G' and G'' have changed. In figure 3.9c, the mean and standard deviation of G' and G'' are shown together with the newly calculated value for G' and G'' according to Eqn. (3.20). G' is overestimated after fitting the stress relaxation data, but is still within the standard deviation of the measured data.

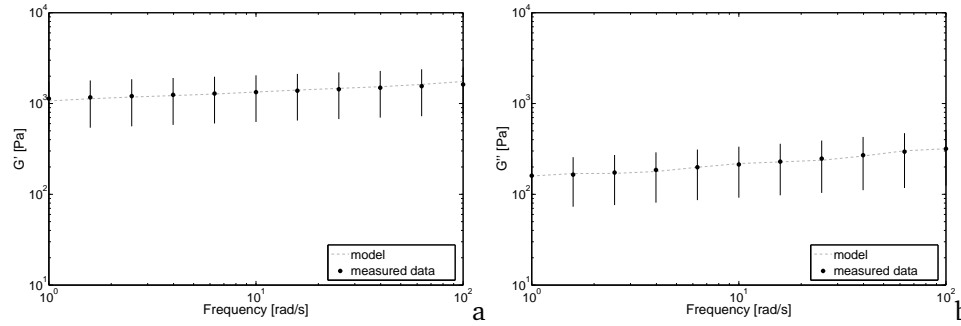


Figure 3.8: Mean G' (a) and G'' (b) with the standard deviation over all samples. The mean value was fitted to a multi mode Maxwell model.

3.4 Discussion

In this work the non-linear viscoelastic properties of thrombus are studied. In previous research we did show that rheometry is a useful method to determine linear viscoelastic properties (van Dam et al., 2006). Since thrombus experiences large strains in vivo, the characterisation of the material behaviour has been extended to the non-linear regime. A non-linear multi mode model to describe the viscoelastic behaviour of the thrombus is chosen. This model consists of a number of non-linear viscoelastic modes, described by linear viscoelastic parameters G_i and λ_i only, and a non-linear equilibrium mode, described by a non-linear spring. The linear viscoelastic modes and the non-linear equilibrium mode were based on experimental data. If it is assumed that the loading time is long enough for the sample to relax completely, the coefficient in Eqn. (3.17) can be taken as the last response before the load is released (Fig. 3.10a). If this coefficient is extracted for each strain and plotted against the strain, it is clear that it is decreasing with increasing strain (Fig. 3.10b). Thus, it is strain dependent in a non-linear way. When the response for each strain amplitude is normalised to the strain and the accompanying value for the coefficient of Eqn. (3.17), it can be seen that the shape of the responses is equal for all strains (Fig 3.10c). The relaxation behaviour is strain dependent in a linear way. Therefore, linear springs and dashpots were chosen for the viscoelastic modes, whereas the equilibrium mode is described by a non-linear spring. To obtain the linear model parameters, shear experiments in the linear strain regime were performed on thrombi from seven patients. As has been described earlier (van Dam et al., 2006) samples cannot be gathered from all parts of the thrombus. The tissue at the abluminal side of the thrombus is too degenerated to cut samples from. The abluminal thrombus is, however, responsible for the attachment of the thrombus to the wall. The nature of the thrombus-vessel wall contact is unclear to the authors, and will be a subject of further research. When studying the change of G' and G'' throughout the thickness of the thrombus, each thrombus shows its own behaviour. No general curve can be recognised that describes a gradual change of material properties throughout all dif-

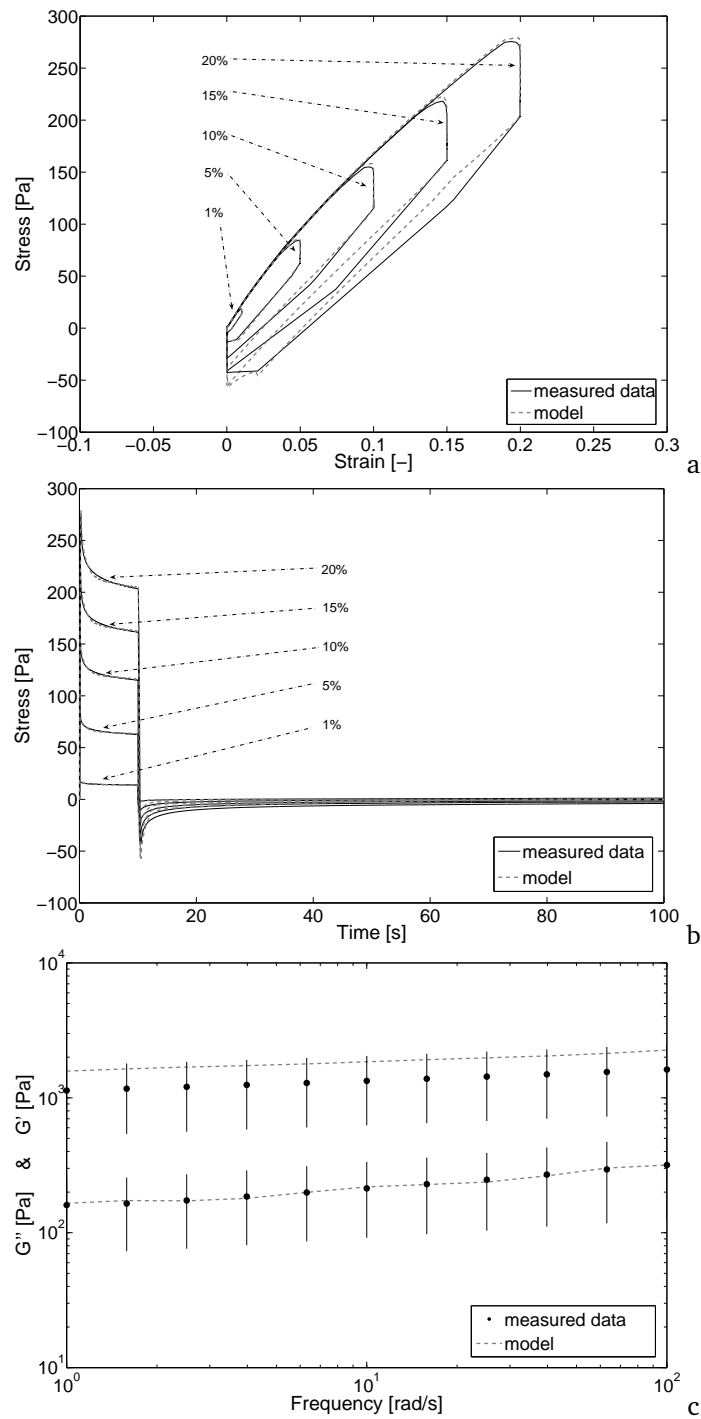
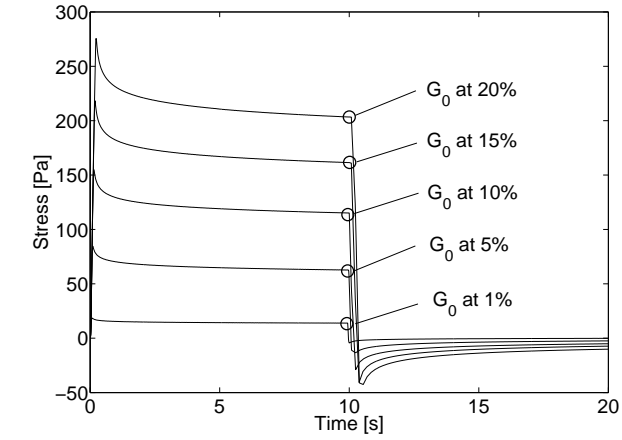
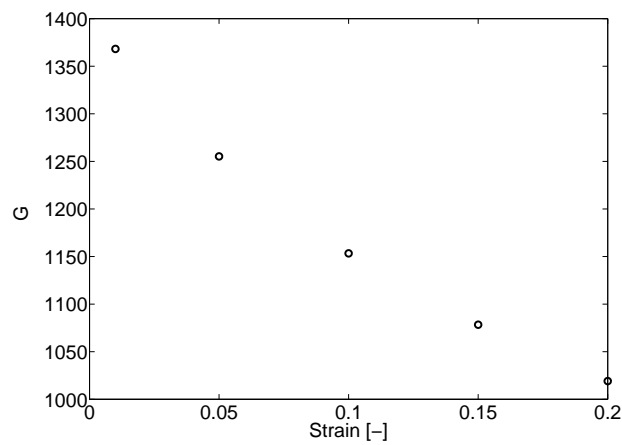


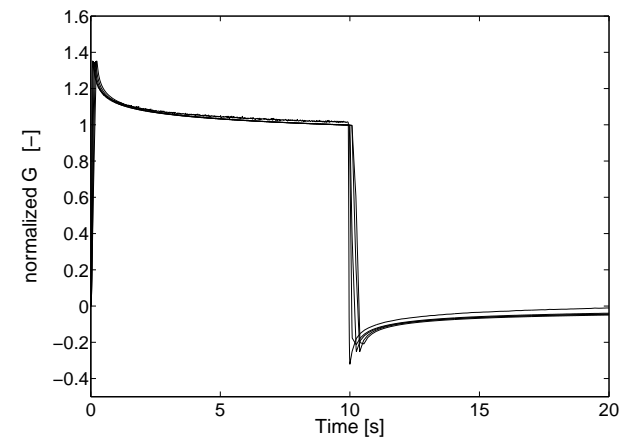
Figure 3.9: Stress strain relation (a), the stress relaxation (b) and the linear parameters, G' and G'' (c), for the mean response together with the model description.



a



b



c

Figure 3.10: When the coefficient of (3.17) is extracted from the stress relaxation responses (a), and plotted against the strain ($G = G_0 f(I_1)$) it can be seen that it is strain dependent (b) in a non-linear way. When the stress responses are normalised to strain amplitude and the accompanying value for the coefficient, it is clear that the relaxation is linear dependent on the strain (c).

ferent thrombi. Values found are all in the same order of magnitude. The mean value for G' and G'' does not differ significantly between patients.

Values for G' and G'' we have reported in earlier work (van Dam et al., 2006), were approximately three times higher than reported in this study. A possible reason for this is the use of a moisture chamber in this study. Dehydration of the sample could lead to altered mechanical properties. Hinnen et al. (2007) performed dynamic mechanical experiments on thrombus in the linear regime. They reported mean G' and G'' of 35 and 8 kPa, which is an order of magnitude higher than the values reported in this work. The results by Hinnen et al. (2007), may be influenced by their experimental method which included glueing of the sample.

Responses in the large strain regime have been studied by performing stress relaxation experiments. Since the loading phases of all curves, with increasing strain, overlap well, it can be concluded that the samples were not damaged during the experiments. Mechanical damage would have led to an immediate change in the response. To describe the behaviour, model parameters were obtained from the experimental data. The fitting procedure resulted in a unique parameter set as long as the initial guesses for G and λ are within the same range as the experiments.

All the non-linear parameters play a specific role. Parameter b allows for weighting between the invariants I_1 and I_2 and, therefore, distinguish between the non-linear behaviour in shear and extension ($I_1 = I_2$ in shear, $I_1 > I_2$ in extension). The non-linear behaviour is fully captured with the parameters A and C . The strength of the non-linearity is described by C , while A weights the non-linearity with the linear part. Most parameters, linear and non-linear, are only weakly correlated except for those that determine the level of the stress, i.e. A , G_0 and G_4 (the mode with the highest relaxation time and thus the most elastic mode).

It has been shown that the mean response of all samples can be described by the non-linear multi mode model, as described in section 3.2.2, in a satisfying way. Whereas the stress relaxation is described very well, G' is overestimated by the model. This is the result of the objective function in which the non-linear error is weighted heavier than the non-linear error because of absence of normalisation of the non-linear error. The overestimation can be prevented by applying normalisation of the non-linear error to the mean value of the non-linear experimental data. The objective function then changes to:

$$\epsilon = \frac{1}{n} \sum_{i=1}^n \left(\frac{(G'_{mod}(i) - G'_{exp}(i))^2}{G'_{exp}(i)^2} + \frac{(G''_{mod}(i) - G''_{exp}(i))^2}{G''_{exp}(i)^2} \right) + \frac{1}{m} \sum_{j=1}^m \frac{(\sigma_{mod}(j) - \sigma_{exp}(j))^2}{\sigma_{exp}^2} \quad (3.22)$$

Figure 3.11 depicts the results of such a model fit. The description of G' has indeed improved, but the relaxation is now described poorly. When this model is to be implemented in a finite element model, the model parameters as described in the results section can best be chosen. A model for describing relaxation and stress-strain rela-

tion well is more relevant in the physiological situation than a model describing G' and G'' well. The model parameters have been obtained for the mean response of all samples. Thrombi whose response level is extremely high or low may, however, have a pronounced influence on rupture risk prediction using finite element stress analysis. Therefore, the highest and lowest stress responses were fitted to the model proposed. The measured relaxation and the fitted model for these samples is depicted in figure 3.12. It can be seen that the model can describe these outliers well. The model parameters for these extreme experimental results and the mean response are given in table 3.2. It is found that G_0 is an important parameter in describing the behaviour. The non-linear parameters C are all in the same order of magnitude. The variation in parameter A cannot clearly be related to either a high or low response. In the model used the parameter b is set to 1. Experiments other than shear experiments, such as compression tests, are necessary to be able to determine b . Since G' seems to be the major player in describing the thrombus behaviour, only small differences are expected to be found for b . It would, however, be an interesting subject for further research.

The influence of the non-linear viscoelastic behaviour can be studied by implementing the material model into finite element AAA stress calculations (Wolters et al., 2005). Although the moduli found are very low, the viscoelastic behaviour may play a role in the attenuation of pressure waves travelling through the arterial system. When implementing the parameters found for the highest and lowest stress response leads to large variations in wall stress and its distribution, a method has to be developed to obtain the mechanical properties of thrombus in a patient-specific way. When the resulting variations in wall stress, however, are small, one may assume that all thrombi may be described with the same parameter set.

	mean		highest		lowest	
mode	G [Pa]	λ [s]	G [Pa]	λ [s]	G [Pa]	λ [s]
1	$5.7 \cdot 10^2$	$9.5 \cdot 10^{-3}$	$1.1 \cdot 10^3$	$1.0 \cdot 10^{-2}$	$1.6 \cdot 10^2$	$1.0 \cdot 10^{-2}$
2	$2.7 \cdot 10^2$	$9.6 \cdot 10^{-2}$	$5.6 \cdot 10^2$	$9.3 \cdot 10^{-2}$	$9.7 \cdot 10^1$	$1.0 \cdot 10^{-1}$
3	$2.6 \cdot 10^2$	$9.1 \cdot 10^{-1}$	$5.3 \cdot 10^2$	$8.7 \cdot 10^{-1}$	$1.1 \cdot 10^2$	$1.1 \cdot 10^0$
4	$1.7 \cdot 10^2$	$2.8 \cdot 10^1$	$1.1 \cdot 10^3$	$1.1 \cdot 10^2$	$1.2 \cdot 10^{-9}$	$1.2 \cdot 10^2$
G_0 [Pa]	$1.3 \cdot 10^3$		$2.7 \cdot 10^3$		$4.4 \cdot 10^2$	
A [-]	$5.7 \cdot 10^{-1}$		$2.8 \cdot 10^{-2}$		$4.6 \cdot 10^{-1}$	
C [-]	$5.8 \cdot 10^0$		$2.4 \cdot 10^0$		$8.7 \cdot 10^0$	

Table 3.2: Model parameters that describe mean response and the highest and lowest stress response.

Wang et al. (2001) related the mechanical properties of luminal and medial thrombus to the structural state of the tissue. To study the relation between mechanical properties and structure of the tissue, ESEM images were also included in this work (Fig 3.1b). On a global scale structural changes can be seen, but these differences cannot be found consistently in the material behaviour. Local differences in struc-

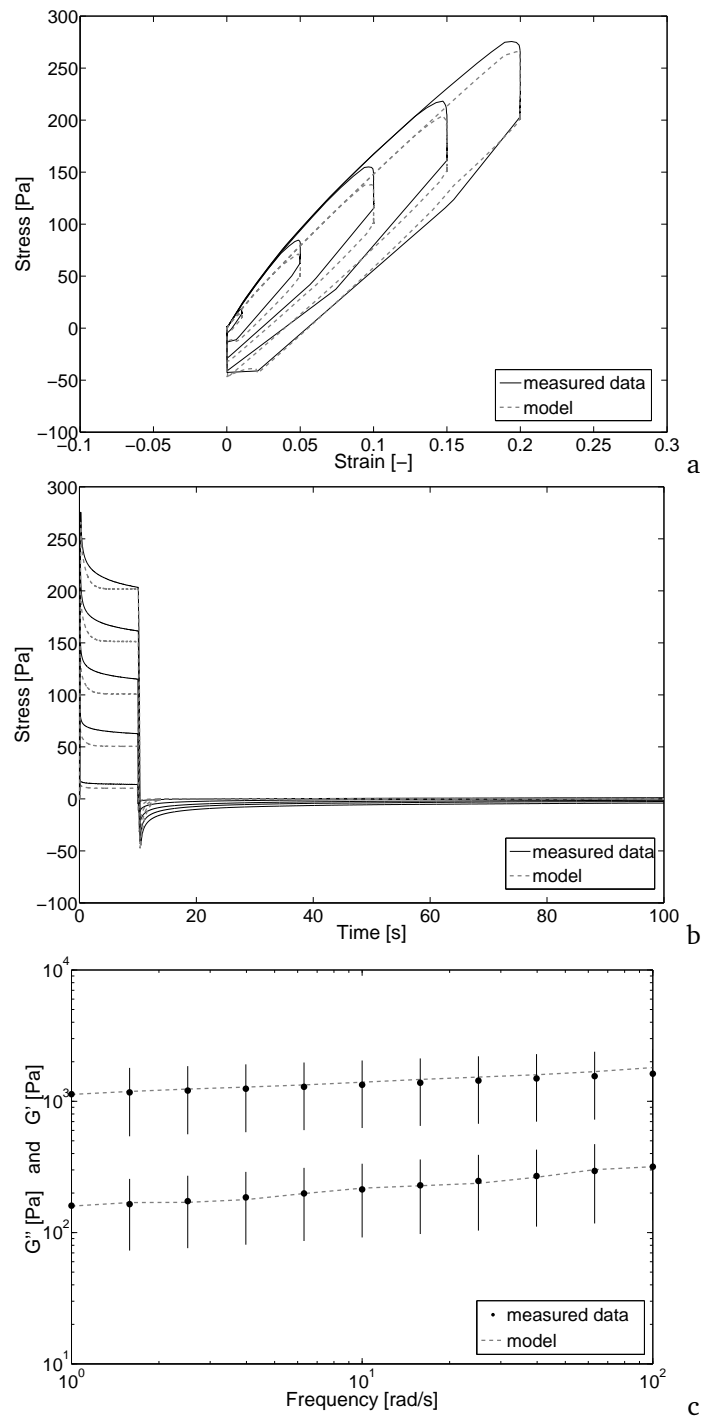


Figure 3.11: Stress strain relation (a), the stress relaxation (b) and the linear parameters, G' and G'' , for the mean response together with the model description. G' and G'' were weighted heavily by using the objective function (3.22) for fitting the model parameters.

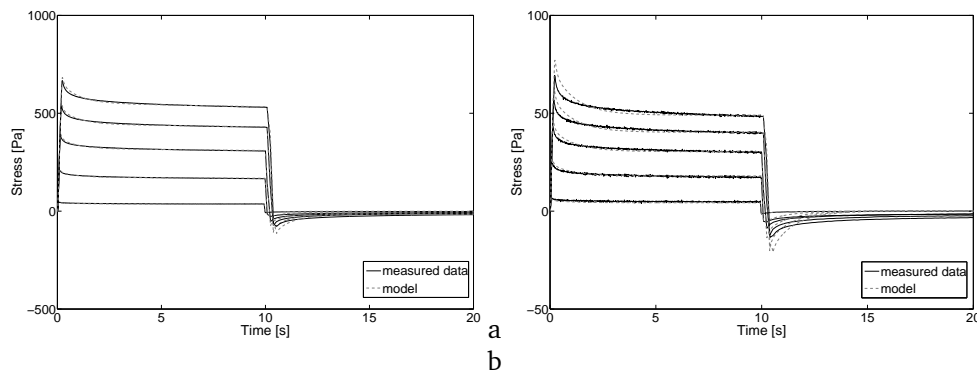


Figure 3.12: The stress relaxation as measured together with the model description for the samples with the largest (a) and smallest (b) response.

ture could lead to the local effects in properties that we found. The structure seen in ESEM images and the mechanical properties of samples taken from an adjacent slice of thrombus cannot be related directly. This would probably require ESEM images of each rheological sample.

3.5 Conclusion

From experimental data it is concluded that the change of properties throughout the thrombus is different for each thrombus. The variations found within one thrombus are of the same order of magnitude as the variation between patients. This suggests that the same material parameters may be used to describe all thrombi.

The multi mode viscoelastic model proposed can be used to describe the linear and the non-linear viscoelastic properties of intraluminal thrombus. The parameters can be obtained successfully by fitting it to the experimental data. The model cannot only describe the average stress response but also the highest and lowest stress responses. These may play an important role in rupture risk prediction using finite element stress analysis and implementation of the model is needed to determine the influence on the wall stress of responses found.

Chapter 4

Discrimination of Components of AAA Vessel Wall by Multi Contrast MRI

4.1 Introduction

Rupture of an abdominal aortic aneurysm (AAA) is a major cause of death in the Western world. When the AAA is diagnosed timely, rupture can be prevented by conventional surgical or by endovascular repair. Since mortality rates of these interventions are as high as 4.0% and 2.9% respectively (Hua et al., 2005), the decision to operate should only be made when rupture risk exceeds the risks of intervention. Nowadays, this decision is based on the maximum diameter of the aneurysm, but it has already been suggested that wall stress would be a better predictor than the maximum diameter (Fillinger et al., 2003). Patient specific computational models have been developed to calculate this wall stress (Fillinger et al., 2003; Inzoli et al., 1993; Hua and Mower, 2001; di Martino and Vorp, 2003; Mower et al., 1997; Papanicolaou et al., 2007; Raghavan et al., 2005; Scotti et al., 2005; Stringfellow et al., 1987; Vorp et al., 1996, 1998; Venkatasubramanian et al., 2004; Wang et al., 2002; Wolters et al., 2005). Although it is known that the aneurysm vessel wall is not a homogeneous tissue, these models only assume homogeneous vessel wall properties. It has, however, already been shown that inhomogeneities such as atherosclerotic plaques and calcifications have large effects on the maximum wall stress and wall stress distribution (de Putter et al., 2006b; Inzoli et al., 1993; Speelman et al., 2007). The presence and distribution of inhomogeneities is highly patient specific and should therefore be dealt with accordingly. Although histological staining is a sound method to determine tissue composition and structure, its highly invasive character prevents it from being suitable diagnostic tool. A non-invasive imaging tool should therefore be used to obtain tissue morphology.

Although CT images can provide information about calcification of the vessel wall they do not provide information about other inhomogeneities due to CT's limited abilities in imaging soft tissues. Another noninvasive imaging method, magnetic resonance imaging (MRI) has already been shown to be useful in obtaining the dimensional and compositional properties of carotid arteries (Clarke et al., 2003; Itskovich et al., 2004; Morrisett et al., 2003; Shinnar et al., 1999). Multiple MR contrast weightings are required for identification of plaque components. Since there is a strong clinical and histopathological association between AAA development and atherosclerosis, multi contrast MR may also be valuable tool to study AAA vessel wall inhomogeneities. It is, however, difficult to employ the method as described for the carotids by different groups in the AAA research for several reasons. First of all, each research groups described the carotid plaques by different tissue types. Clarke et al. (2003) suggest that the plaques can be adequately described with the use of only four tissue classes: fibrous tissue, necrotic core, calcification and loose connective tissue. Thrombus is then not taken into account, but is included in other work (Morrisett et al., 2003; Shinnar et al., 1999). Furthermore, Itskovich et al. (2004) report differences in MR properties between loose fibrous and dense fibrous tissue. Besides the different types of tissue that are classified, the results are sometimes in contradiction. Clarke et al. (2003) report that the necrotic core is bright in diffusion weighted MR, while Shinnar et al. (1999) found that only thrombus is bright in the diffusion weighted MR image. According to Morrisett et al. (2003) thrombus has a long T2,

which is in contradiction with the result of Itskovich et al. (2004) who reports that thrombus appears dark in the T2 weighted image, indicating a low T2 value. Part of these differences can be explained by the differences in MR field strength and sequences that were used. The lack of consensus makes it impossible to extrapolate the results from literature to the results that could be expected from multi contrast imaging of the AAA vessel wall imaging.

The degrading vessel wall is likely to show the same types of tissue as the carotids. Fibrous tissue, calcifications, connective tissue, thrombus and even areas with atherosclerotic plaques do occur in AAA vessel wall, and multi contrast MR might be a useful tool to determine the heterogeneity of the vessel wall. The value of the multi contrast MR weightings for determination of AAA vessel morphology will be studied in this chapter.

High resolution multi contrast MRI is applied to ex vivo AAA vessel wall samples. To enable automatic image segmentation and objective classification of vessel wall components a clustering algorithm will be introduced. μ CT is used as a golden standard for the detection of calcium deposits and histological examination is used as a golden standard for tissue composition.

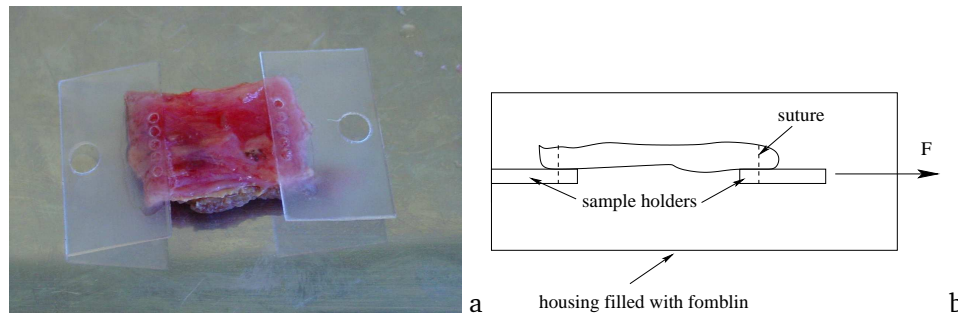


Figure 4.1: the samples were glued and sutured to two holders (a). To stretch the sample a force was applied to one sample holder, while the other was fixed to the housing (b). The housing was filled with fomblin.

4.2 Methods and Materials

4.2.1 Multi Contrast MRI

AAA tissue was obtained from patients undergoing elective surgical AAA repair. Because this material is discarded in the normal clinical setting and it is anonymised after the procedure, making tracing back to the patient impossible, informed consent was not required. The procedure was in conformity with the code of conduct for use of human material as stated by the Dutch federation of Biomedical Scientific Societies. Samples were stored at -80°C . Before imaging the samples were thawed in a

bath with lukewarm water. Of each sample a strip, with a size of approximately 15 mm \times 30 mm, was used for imaging. The sample was attached at two sides to a sample holder. Each sample holder was first glued to the sample and to prevent tearing of the sample, several sutures were made through the sample and the holder. One sample holder was fixed to the housing, while a load was applied to the other. To avoid curling, the sample was stretched slightly by application of a small load. The samples were immersed in fomblin (Solvay Solexis, Milano, Italy). Since fomblin has no MR signal, the sample can easily be segmented from the background. The entire set-up was mounted inside a 6.3T MR scanner with a Bruker Biospec imaging console. To enable MRI-measurements the housing was encompassed by an 8-legged low-pass birdcage RF coil (RAPID biomedical, Würzburg, Germany).

Three different MR contrast, T1-weighted (T1w), T2 weighted (T2w) and diffusion weighted (Dw) Spin Echo (SE) were used. The in-plane resolution was 117 $\mu\text{m} \times$ 117 μm , and the slice thickness was 1 mm. In the T2w SE 10 echos were acquired. The series of echos can be used to obtain a T2-map of the samples. Further acquisition parameters are given in table 4.1.

	T1w	T2w	Dw
Repetition Time (ms)	626	4000	4000
Echo Time (ms)	10.2	10.2, 20.4 ... 102.0	40
Field of view (mm)	30	30	30
Matrix size	256	256	256
Number of averages	4	2	1
b-value			568 s/mm ²

Table 4.1: MR acquisition parameters.

4.2.2 μCT & histology

Several histological stainings are used as golden standards for tissue morphology. Because calcium is removed during the histological processing, μCT images were obtained as the golden standard for calcium deposits. After MR imaging, the samples were mounted in a custom-made holder, in which the configuration of the sample during MR imaging could be mimicked. The sample was then immersed in PBS and imaged with a Scanco μCT -80 scanner (Scanco Medical, Bassersdorf, CH). The voxel size was 60 $\mu\text{m} \times$ 60 $\mu\text{m} \times$ 60 μm .

After μCT and Multi contrast MR imaging the samples were decalcified, embedded in paraffin and were cut into 5 μm thick slices. The stainings performed were based on the tissue types expected in the AAA vessel wall. The morphology of the vessel wall of AAA has changed severely compared to a healthy vessel wall. The wall of a healthy aorta consists of three layers. The tunica internica or intima is the innermost layer, lined by endothelium. The thick elastic layer is called the tunica media and consists of elastic fibres (elastin) and smooth muscle cells (SMC). SMCs synthesise the components of the extracellular matrix. The tunica externa or adventitia is the

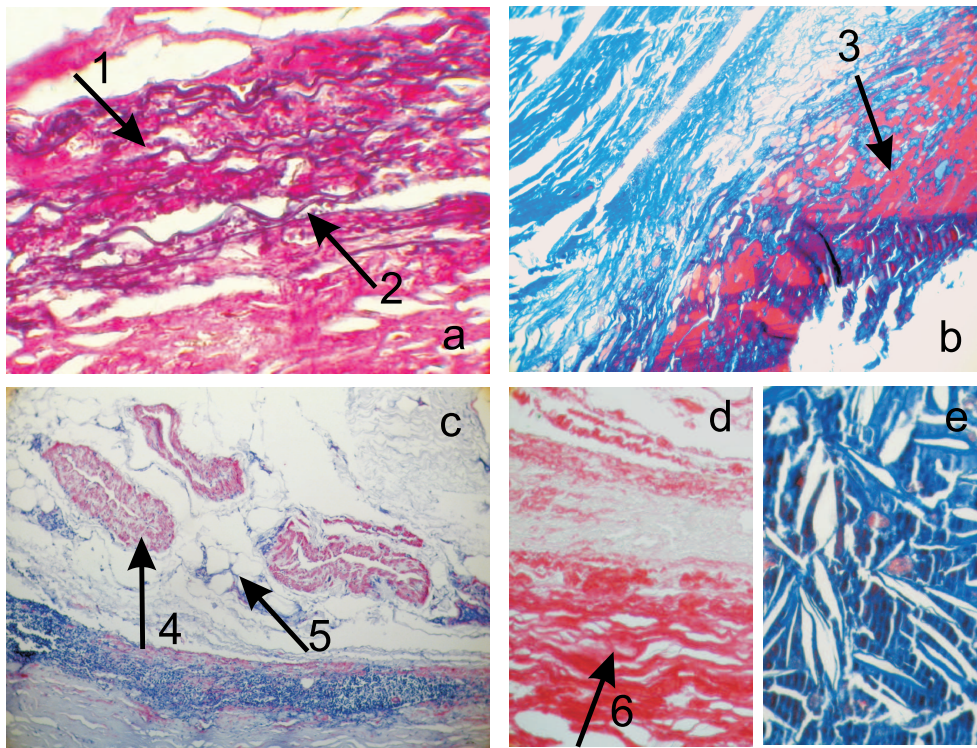


Figure 4.2: The components that can be found in the AAA with the proposed stainings. In a EvG staining (a) collagen is pink and elastin black. Fragments of elastin can be found in AAA tissue (arrow 1 & 2). The MSB staining (b) shows a clear difference between collagen (blue) and fibrin (red, arrow 3). In the ASMA staining (c) SMCs appear red. The vasa vasorum that may occur in the adventitia (arrow 4) can be seen clearly. Fat cells can be recognised by their typical morphology (arrow 5). Sirius red stain (d) is mainly used to stain collagen red. Cholesterol crystals can be recognised in any staining by their typical shape (e).

tough outer layer, which consists mainly of collagen fibres. Adventitial fibroblasts also have the capacity to synthesise extra cellular matrix components. In the aneurysm wall this three layer structure is destroyed and can no longer be recognised. Elastin content decreases (Dobrin, 1989; He and Roach, 1994; Sumner et al., 1970) and elastin fibres that are found are often fragmented (Kazi et al., 2003). An Elastin van Gieson staining (Fig. 4.2a) shows the elastin fragments in the media. Collagen appears blue in the MSB (Martius-Scarlet-Blue) staining (Fig. 4.2b), which can be positively affirmed by a Sirius red staining (Fig. 4.2d). To determine SMC location an ASMA (α -Smooth-Muscle-Actin) staining (Fig. 4.2c) is used. The SMCs in the vasa vasorum serve as an internal positive control for the staining. Other components that can be found in the AAA vessel wall are fibrin, cholesterol crystals and fat cells. Fibrin is stained red in the MSB staining (Fig. 4.2b). Cholesterol crystals are not stained but

can be recognised by the remaining 'tears' in the tissue (Fig. 4.2e). Fat cells always occur in the adventitia and can be recognised by their morphology. (Fig. 4.2c). Vasa vasorum can best be seen in the ASMA staining. The SMCs in the small vessel appear red (Fig. 4.2c). The stainings performed are summarised in table 4.2.

staining	stained tissue	colour
ASMA	Smooth muscle cells	brown/red
Sirius red	Collagen	red
MSB human	Nuclei	black
	Erythrocytes	yellow
	Fibrin	red
	collagen	blue
	Elastin van Gieson	Elastic fibres
	Collagen	red
	Muscle and cytoplasm	yellow

Table 4.2: Stainings used for the AAA wall samples

4.2.3 Image analysis

Prior to further analysis all the grey values of all MR images were normalised to values between 0 and 1. μ CT and histological images were manually registered to the MR images. The influence of cholesterol crystals, thrombus or calcium on MR images will be shown by use of three samples. Additionally, two complete data sets of two other samples will be shown.

The different components in the vessel wall may be automatically extracted from the multi-contrast images using image analysis. A standard k-means cluster algorithm (Lloyd, 1982) will be used to assign each image pixel to a cluster. The clustering procedure is schematically given in figure 4.3. First, a 3 dimensional feature space is built with the normalised grey values of the individual contrasts (T1w, T2w, Dw) along the axes. For each pixel position a data point is put in the feature space at the position determined by the grey values at the pixel position in the T1w, T2w and Dw image. Next, for each cluster a random seeding point is chosen and all data points are assigned to the nearest seeding point. Points that are assigned to the same seeding point form a cluster. An iterative procedure calculates the mean position of all the points in each cluster and moves the seeding points towards those mean values. The points in the feature space are then individually reassigned to the nearest seeding point. This is repeated until the position of the seeding points does not change anymore. Each cluster then consists of pixels with the same characteristics and represents one type of tissue. All image analyses of the MR data were performed using Matlab (Mathworks, Massachusetts).

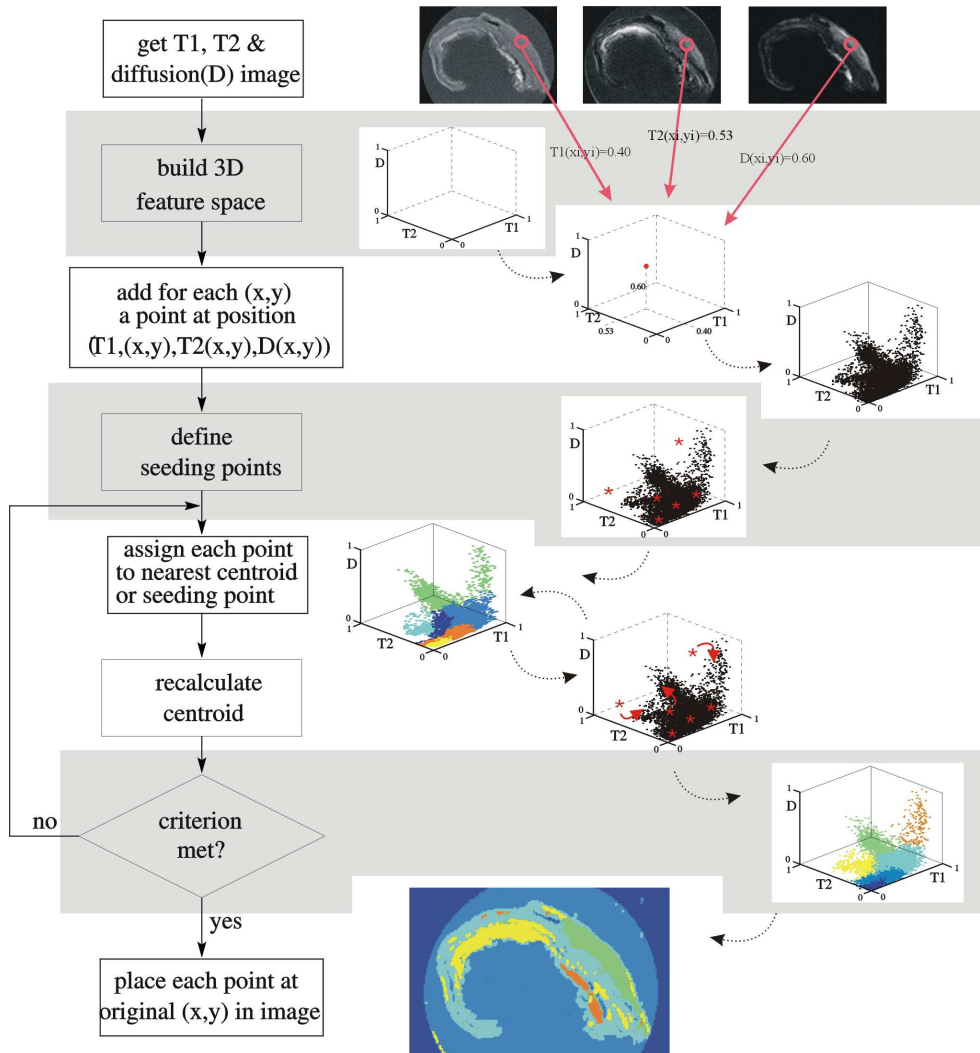


Figure 4.3: Flowchart of k-means clustering algorithm. MR data is converted to a 3D feature space and k-means clustering is applied resulting in an image in which each pixel is assigned to one of 6 clusters.

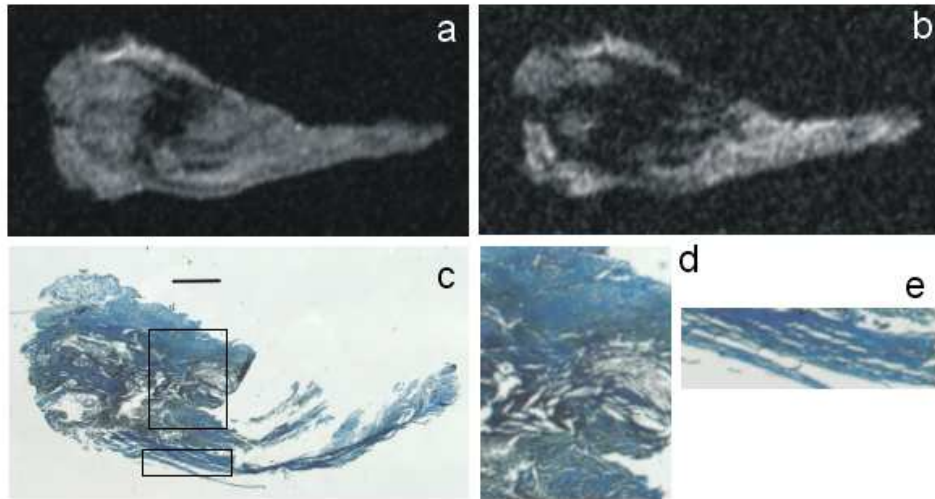


Figure 4.4: T1w (a) and T2w (b) images of sample that contains cholesterol. MSB staining (c) and indicated enlargements of cholesterol and collagen structure of adventitia (d) and collagen in media (e). The horizontal bar (c) corresponds to 1 mm.

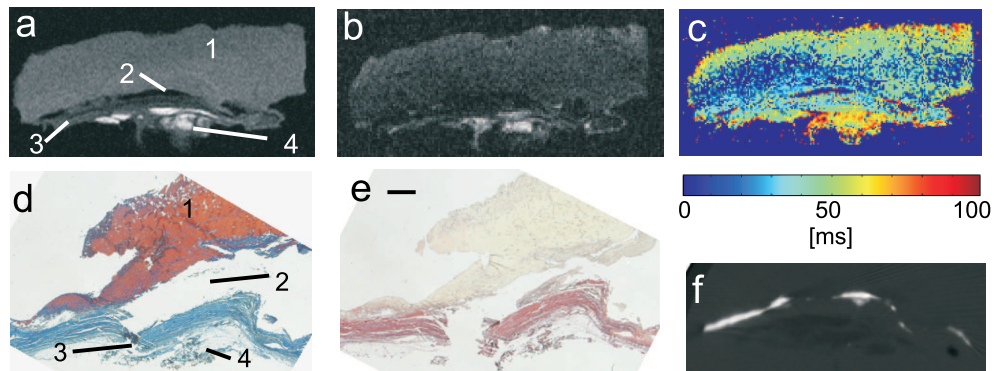


Figure 4.5: Sample with thrombus attached. Multi contrast results in the T1w (a) and Dw (b) images and the T2 map (c). Corresponding histology: a MSB staining (d) and a Sirius red staining (e). The presence of calcification is verified with μ CT (f). Tissue morphology is destructed by the histological procedure. The sample tears at the calcification (2). A thick layer of thrombus is present (1), and a collaganeous media (3) and fatty adventitia (4). The horizontal bar (e) corresponds to 1 mm.

4.3 Results

Figure 4.4 shows the T1w and T2w images of a sample that contains a pool of cholesterol crystals (Fig. 4.4c and d). The area appears dark in both MR images. The sample shows no signs of an intima. The media and adventitia can be recognised by their collagen structure.

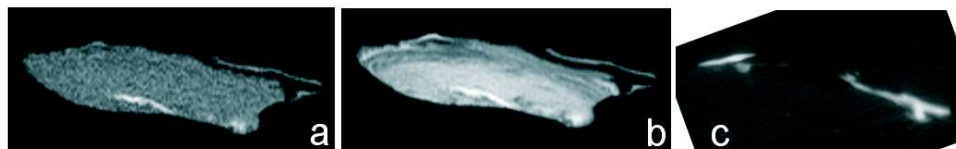


Figure 4.6: T1w (a), T2W(b) and μ CT (c) image of a sample of which only the media and calcifications can be recognised.

Part of the thrombus was still attached to the sample shown in figure 4.5. In the MR images the thrombus appears homogeneous. The calcified deposits can be clearly identified in the μ CT images. The adventitia is bright in all MR images and contains loose connective tissue and fat cells. The morphology of the sample is desctructed during the histological procedure. When cutting slices, the decalcified tissue tears at the former side of the calcification.

Another sample shows a lot of calcifications. The μ CT (Fig. 4.6c) images show the calcium deposits are positioned in a layer, that can be easily depicted in the MR images (Fig. 4.6a and b). Two complete datasets are shown in figure 4.7 and 4.8. Some pieces of thrombus are still present, which again can be recognised in the MR images as a homogeneous tissue (arrow 1). A large amount of loose connective tissue is present at the adventitial side (arrow 2). The collageneous media shows as a dark band in the MR images (arrow 3). Small calcified deposits (arrow 4) were found in the μ CT, but were hard to recognise in the MR images of the sample in figure 4.7.

4.4 Discussion

In this work it has been shown that the degenerated structures of a AAA vessel wall correspond to findings in MR and μ CT results. Comparison of the different modalities is a difficult task for several reasons. Structures that can be recognised on the high resolution histological photographs such as elastin fragments are too small to be recognised in the MR images. Furthermore, histological sections were 5 μ m thick, while the MR slices had a thickness of 1 mm. Partial volume effects result in occasional blurring of regions that are evident in the histological images.

Automatic registration of the MR images to the histological images would provide a way to compare MR values with histological findings on pixel-based way. The tissue is, however, fixed in formalin for the histological procedure and AAA vessel wall samples curve in the opposite way when fixed in formalin. Another source of loss

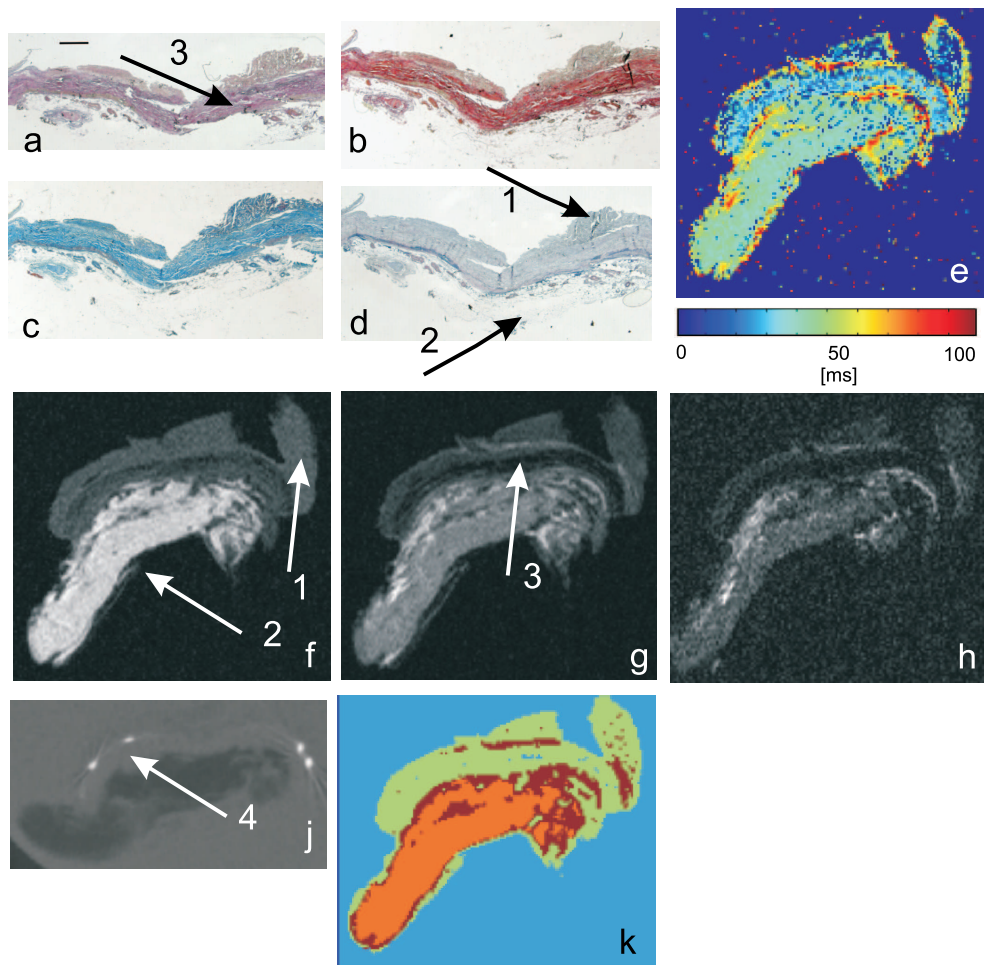


Figure 4.7: Complete data set of AAA sample: EvG (a), sirius red (b), MSB (c) and ASMA (d) staining and MR images: T2 map (e), T1w (f), T2w (g) and Dw (h) images. Calcium is bright in the μ CT image (j) and the results of k-means clustering algorithm (k). Thrombus (arrow 1), adventitia (arrow 2), media (arrow 3) and calcification (arrow 4) can be recognised. The horizontal bar (a) corresponds to 1 mm.

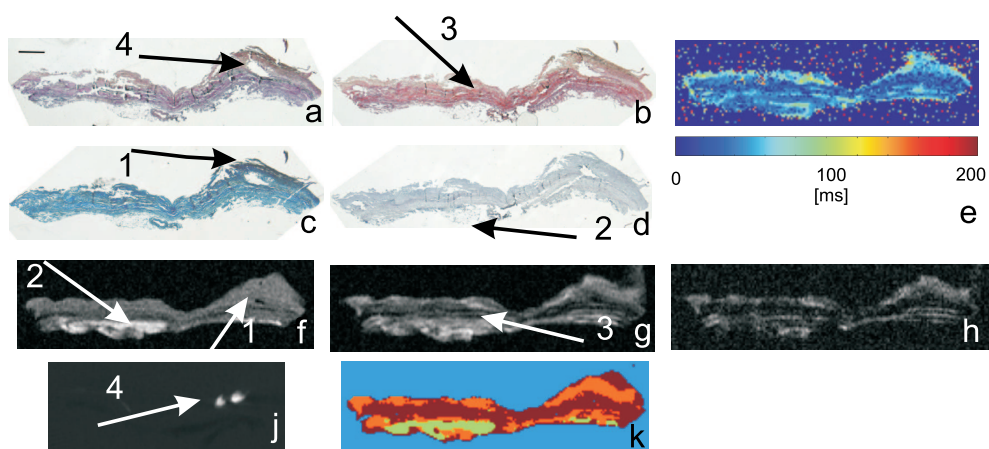


Figure 4.8: Complete data set of AAA sample: EvG (a), sirius red (b), MSB (c) and ASMA (d) staining and MR images: T2 map(e), T1w (f), T2w(g) and Dw(h) images. Calcium is bright in the μ CT image (j) and the results of k-means clustering algorithm (k). Thrombus (arrow 1), adventitia (arrow 2), media (arrow 3) and calcification (arrow 4) can be recognised. The horizontal bar (a) corresponds to 1 mm.

of morphology is the decalcification in the histological preparation. When a sample contains a lot of calcium (Fig. 4.6 and 4.7) the histological sections tears at the side of the former calcium. Correcting these deformations with image analysis techniques is not straightforward and outside the scope of this work.

Multi contrast MR as a tool for characterisation of atherosclerotic plaques in the carotids has been reported by several research groups, but there is lack of consensus in the results. Although the results for the carotids may not directly relate to those of the aortic wall, a comparison of our data with the reported results is plausible. We found that an area with a lot of cholesterol crystals, which might be compared to necrotic core, was dark in all weightings. Thrombus was a little brighter in the T1 images than the media. T2 of thrombus could only be determined in one sample. Values varied between 30 and 60 ms. This is in agreement with the findings of Itskovich et al. (2004) but in disagreement with the findings of Morrisett et al. (2003). The opposite holds for the media. In all the images a dark band was found that corresponds to the collagenous media, which is in agreement with Morrisett but in disagreement with the findings of Itskovitch. The loose connective tissue at the adventitial side was very distinctive in almost all images as was also reported before (Clarke et al., 2003). It should be noted that the results in this work were obtained with a 6.3T scanner, while none of the other studies was performed at this field strength.

Automatic classification can be performed in several ways. Shinnar et al. (1999) determined grey values in 3 modalities for all tissue classes and used these to segment the images. Clarke et al. (2003) extended such a method with a k-means algorithm. Even more complex, Anderson et al. (2007) used a neural network for predictive modelling and found that the results were 25% to 30% better compared to clustering.

All these methods, however, require training data. To obtain these data regions of the images needed to be selected that convincingly belong to a certain tissue class. Mistakes in the training data lead to structural errors in the automatically classified results. Furthermore, all tissue classes need to be abundantly present in the training data.

In this work, only a limited number of samples was available and some tissue classes (like thrombus) only are present in two datasets. Therefore we have chosen for an unsupervised k-means clustering algorithm, that does not take advantage of expert experience. The results of the k-means clustering algorithm are, however, disappointing. Figure 4.7k and 4.8k show that the thrombus is in the same cluster as part of the media. The adventitial loose connective tissue is classified as a separate tissue, but the small calcified deposits merge in the media clusters. A problem with the unsupervised clustering is the choice of the number of clusters that are needed to classify the tissue. An increase in clusters does not improve the results in this study (Fig. 4.9). To improve classification results a more complex clustering algorithm needs to be developed. The results reported in this work indicate that multi contrast MR images



Figure 4.9: The results of the clustering algorithm for a chosen number of 3 (a), 4 (b) or 5 (c) clusters.

correspond to the histological findings and that multi contrast imaging is a promising tool for characterisation of the AAA vessel wall. To quantify the agreement between histology and MR images, however, more images should be acquired. These result could then be used as input for a supervised classification algorithm.

Implementing the inhomogeneous structure found in FE models would not only require knowledge about the morphology of the vessel wall, but also about the mechanical properties of the components present in the vessel wall. In this work a first step towards including inhomogeneities is made by studying the possibilities of multi contrast MRI to obtain information about the components and morphology of the AAA vessel wall. Determination of the mechanical properties of the components found will be presented in the following chapters.

Chapter 5

A Mixed Numerical Experimental Method for Mechanical Characterisation of AAA Vessel Wall

5.1 Introduction

Predicting Abdominal Aortic Aneurysm (AAA) rupture using patient specific wall stress analysis has the potential to be superior to the currently used maximum diameter criterion. Wall stress studies using idealised geometries showed that the wall stress distribution of an aneurysm depends on the wall thickness (Scotti et al., 2005), diameter (Stringfellow et al., 1987; Vorp et al., 1998) and shape (Hua and Mower, 2001; Scotti et al., 2005; Stringfellow et al., 1987; Vorp et al., 1998). Since geometries of aneurysms are widely complex (Sacks et al., 1999), several studies focused on patient specific models. Wall stress turned out to be complexly distributed and to show large regional variations (Raghavan et al., 2000; Thubrikar et al., 2001a). Peak wall stress was correlated to the site of rupture (Venkatasubramaniam et al., 2004) and was suggested to be a superior rupture risk predictor compared to diameter (Fillinger et al., 2002, 2003; Raghavan et al., 2005; Venkatasubramaniam et al., 2004).

In several patient specific models the mechanical properties of the vessel wall are assumed to be linear elastic (Inzoli et al., 1993; Hua and Mower, 2001; di Martino et al., 2001; Mower et al., 1997; de Putter et al., 2006a; Scotti et al., 2005; Stringfellow et al., 1987; Vorp et al., 1996, 1998; Wolters et al., 2005). The Young's modulus is either estimated or experimentally determined (di Martino et al., 2001). Alternatively, the stress-strain curve resulting from such experiments can be described by an exponential function (He and Roach, 1994; Thubrikar et al., 2001b) or by a two parameter, hyper elastic, isotropic, incompressible model (Raghavan and Vorp, 2000). The latter has been implemented in several studies on the wall stresses in AAA (Fillinger et al., 2003; di Martino and Vorp, 2003; Papaharilaou et al., 2007; de Putter et al., 2007; Raghavan et al., 2000; Raghavan and Vorp, 2000; Raghavan et al., 2005; Venkatasubramaniam et al., 2004; Wang et al., 2002). These models all assume the vessel wall to consist of a homogeneous, isotropic material.

The composition of the AAA vessel wall shows signs of tissue degeneration and reorganisation (chapter 4 and (Kazi et al., 2003)). Since mechanical properties and composition are strongly related, together with variations in composition variations in mechanical properties are expected in the vessel wall. A study on atherosclerotic plaques in an idealised model (Inzoli et al., 1993) revealed that plaques, modelled as an area with a higher stiffness than the vessel wall, causes stress concentrations and a significant increase in maximum stress. The effect of calcifications is similar. Speelman et al. (2007) reported that not only the relative amount but also location and shape of the calcified regions influence the wall stress. de Putter et al. (2006b) showed that peak wall stress is sensitive to the material properties of the calcification. In a literature review by de Putter et al. (2006b) it was reported that the elastic moduli for calcified tissue of coronaries and iliac arteries range from 1.5 MPa to 19 MPa. The mechanical properties of isolated calcified deposits haven been by studied and were found to be in the range of cortical bone, 20 GPa (Marra et al., 2006).

No research has focused yet on the variations of the mechanical properties within the degrading vessel wall. Regions that consist of cholesterol crystals or large amounts of fat cells are likely to show a large difference in mechanical properties compared

to normal vessel wall and therefore have an influence on the stress distribution. The mechanical properties of these tissues need to be determined with a method that does not require the isolation of the individual components.

In this work the feasibility of a mixed numerical experimental method to obtain the mechanical properties of different components in one sample from one single uniaxial tensile test is studied. To develop the method a simplified sample with controllable mechanical properties has been used. A uniaxial load is applied to a sample while the resulting displacement of the sample is recorded in 3 dimensions using MRI. This experiment is simulated numerically and the material properties are optimised in an iterative procedure until the computational results match the experimental results. First an overview of the mixed numerical experimental method is given, followed by an elucidation of the separate methods. Then the feasibility of the method is tested in two steps. First, simulated experiments are used to test the accuracy of the estimation algorithm and the influence of noise on the estimated material properties. Second, it will be shown that the mechanical properties of a non-homogeneous hydrogel sample can be obtained with the mixed numerical experimental method proposed.

5.2 Mixed numerical experimental method

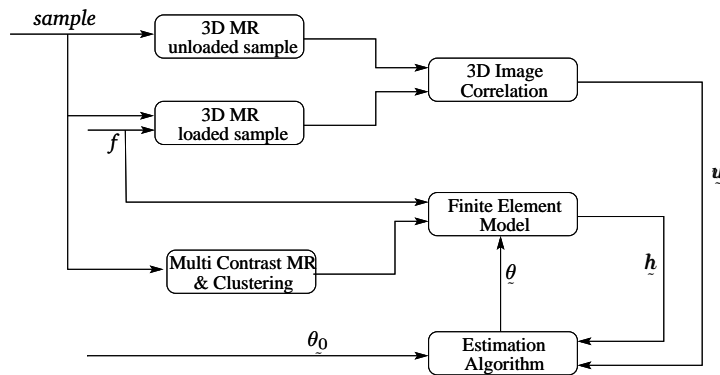


Figure 5.1: Schematic of the mixed numerical experimental method.

The mixed numerical experimental method (Fig. 5.1) used to estimate material parameters (Cox et al., 2006; Meuwissen, 1998) is based on the displacement that results from application of an uniaxial load, f , to a sample under investigation. Before applying the load, a 3D MR image of the sample is acquired. After application of the load, the deformed sample is imaged again. Then, 3D digital image correlation of these two images provide displacements, \underline{u} in 3 dimensions. Next, the experiment is simulated numerically with a finite element computation. The mesh and distribution of the different components are defined based on the MR images. The force that is applied in the experiment is also applied to the sample in the numerical simulation

and the resulting displacement, h_c , is calculated. The difference between the experimental results u , and the computational results, h_c , is minimised by the estimation algorithm that iteratively adjusts the material properties, θ , used in the finite element computation.

The individual elements of the mixed numerical experimental method will be described below.

5.2.1 Load protocol and MR imaging

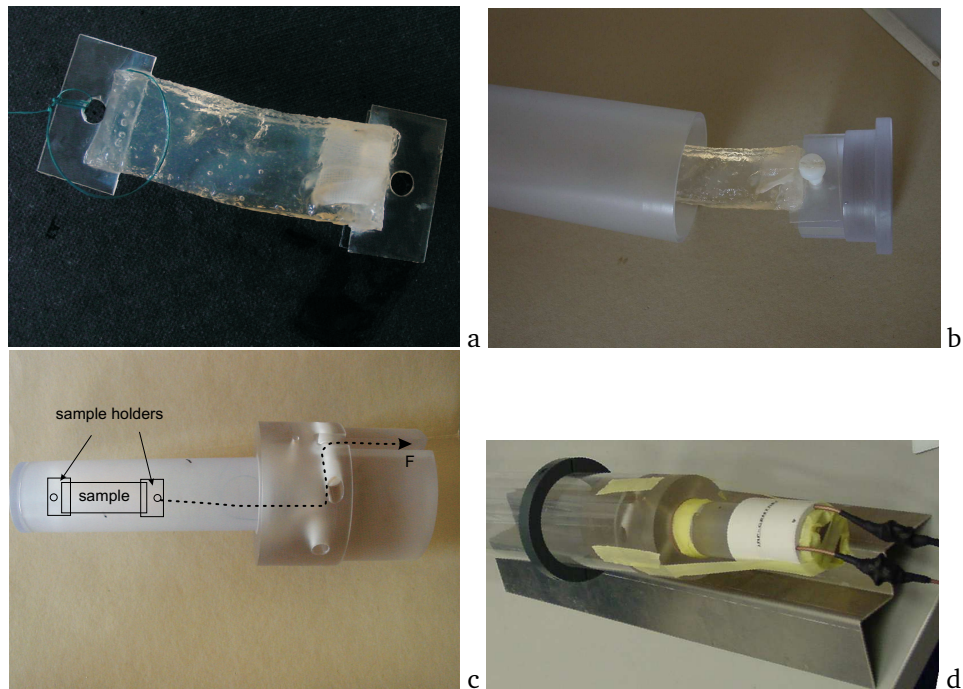


Figure 5.2: The sample attached to the holders (a). Both hydrogels are transparent and cannot be distinguished from each other in this figure. One sample holder is fixed in the set-up (b) while a load can be attached to string attached to the other holder (c). The housing is encompassed by a birdcage RF coil (d).

The sample used in this feasibility study is a polyHEMA hydrogel sample, consisting of two components and MR properties. Both parts were polyHEMA gels, but by changing the composition of the gel, the mechanical and MR relaxation properties of the two parts were adapted. Since the image correlation (section 5.2.2) is based on the presence of contrast distribution, silica beads, with a diameter between 180 and 210 μm , were mixed into both hydrogels. The material behaviour is assumed to be incompressible linear elastic. The Young's moduli, determined for both hydrogels

	T1 3D	T1 2D	T2 2D
Repetition Time [ms]	500	500	4000
Echo Time [ms]	10.2	10.2	30.6
Field of View [mm ³]	30 × 30 × 30	35 × 35 × 40	35 × 35 × 40
Voxel size [mm ³]	0.23 × 0.23 × 0.23	0.14 × 0.14 × 1	0.14 × 0.14 × 1
Averages	2	4	2

Table 5.1: MR parameters of the performed Spin Echo sequences.

separately by uniaxial tensile testing, are $E_1 = 0.38 \pm 0.06$ MPa and $E_2 = 0.25 \pm 0.01$ MPa, respectively.

Each side of the sample is glued to a sample holder (Fig. 5.2a). One sample holder is fixed in the set-up, while a load can be applied to the other (Fig. 5.2b,c,d). The set-up is oriented horizontally to fit into a 6.3T MR scanner with a 120 mm horizontal bore with a Bruker biospec imaging console. To enable MRI-measurements the housing was encompassed (Fig. 5.2d) by an 8-legged low-pass birdcage RF coil (RAPID Biomedical, Würzburg, Germany).

To eliminate the deformation caused by gravity on the sample a load of 0.4 N is applied in the reference state. The T1 weighted images were gathered with a spin echo sequence. Two images were obtained and averaged to increase the signal to noise ratio. The MR parameters are given in table 5.1.

The sample is then loaded with an additional load of 1 N and again a 3D MR image is recorded. Digital image correlation is then used to obtain the 3D displacement field of the sample (section 5.2.2).

Furthermore, to determine the components present in the sample and their distribution multi contrast MR imaging is used. When images from different modalities are combined it is possible to determine the composition of tissues. In this study T1 and T2 weighted images were acquired. To reduce imaging time these images were not gathered 3D but slice-wise. 40 slices, perpendicular to the loading direction, with a thickness of 1 mm covered the entire area used in the 3D T1 imaging. Further details can be found in table 5.1.

5.2.2 Digital Image Correlation

Digital Image Correlation is a method to determine a displacement field by comparing two images of one volume. The technique does not require external markers but is based on the contrast distribution in the images (Meuwissen, 1998; Sutton et al., 1986; Verhulp et al., 2004).

To calculate the displacement of an arbitrary material point (x, y, z) in the first image, a rectangular window A needs to be chosen around this point (x, y, z) (Fig. 5.3). In the deformed situation a search volume, V is defined. In this search volume the window B, which is located around (x', y', z') and is related to A, has to be identified. Window B is found by comparing the contrast distribution for all possible window positions in the search volume, V and finding the maximum correlation. This is done

in two steps. In the first step window B is only translated, and the second step window B is linearly deformed to find maximum correlation. For each correlated window the correlation coefficient (Between 0 and 1, 1 for perfect correlation) is recorded. When no displacement is found, a value of -1 is assigned to this coefficient. For more detail the reader is referred to Verhulp et al. (2004).

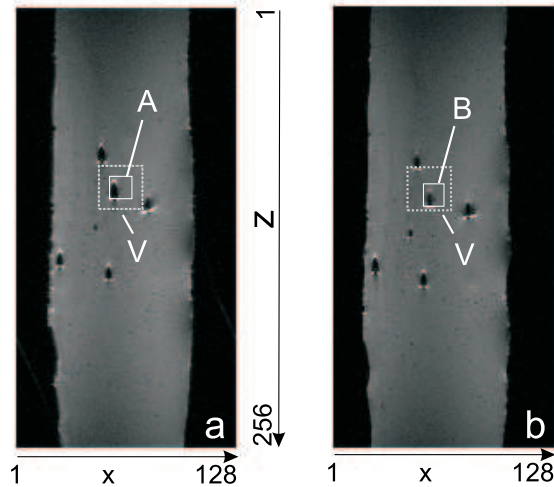


Figure 5.3: Intersection of the 3D T1 data in reference (a) and loaded (b) situation. Window A and B (solid white line) and the search volume V (dashed line) indicated.

When the window is chosen too large it will contain a unique contrast distribution pattern, but the linear deformations of the window are not likely to be near the actual deformation. When the window is too chosen small the linear deformations will be accurate but is unlikely that the contrast distribution pattern is unique.

The silica beads mixed in the hydrogel have a size of 1 to 2 voxels in the MR image. For a unique pattern, the chosen window should include several beads. In this study the window is chosen to be $13 \times 13 \times 13$ voxels. The search volume is $25 \times 25 \times 25$ voxels large and is based on the maximum displacements expected, as determined from a preliminary review of the results. Each voxel within the sample can be chosen as image correlation points, (x, y, z) , the centre of such a window. Due to limitations in computational resources, only 10% of the voxels were used as the centre of a window. The positions of these windows are chosen uniformly distributed over the volume of the sample. The positions of image correlation points, (x, y, z) , always coincide with the position of a voxel, resulting in 256 possible positions in z-direction and 128 in x and y direction.

Image correlation points for which the digital image correlation procedure cannot find a displacement, and thus the correlation coefficient is -1, are discarded from the

data set also. To reduce noise, the outliers need to be discarded from the data set. Since the largest displacements are expected in the direction of the load the results are sorted by their position in that (z) direction. The mean and standard deviation of the displacement for each of the 256 possible positions in the z-direction is determined and points of which the displacements are not within two standard deviations from the mean are discarded from the data set. The computational sources for the parameter estimation are limited and preliminary tests showed that an image correlation data set of approximately 4000 points is sufficient for the parameter estimation. Therefore, approximately 4000 image correlation points are selected for the parameter estimation, based on their correlation coefficients.

5.2.3 Mesh generation and Finite Element Modelling

The 3D T1 image is used to generate a tetrahedron mesh using a marching cubes algorithm (Lorenson and Cline, 1987). This algorithm creates a surface of triangles with the position of the nodes of the surface depending on a specified threshold for the voxel grey-scale (Fig. 5.4b). The volume enclosed by this surface is then filled with tetrahedra (Frey et al., 1994; Verhulst et al., 2004).

A mesh is made of only the central 20 mm of the 3D MR image, in axial direction. In figure 5.4a the part that is used is indicated. The low MR signals at the edges of the field of view in the axial directions are avoided this way. This leads to two well defined surfaces, S_1 and S_2 , that are used to apply boundary conditions to (see section 5.3). The mesh created exists of 21606 tetrahedral linear elements (Fig. 5.4b). In a preliminary study, increasing the total number of elements, did not induce significant changes in the numerical results.

Initial estimated material properties need to be assigned to each nodal point of the generated mesh. Different material properties will be assigned to the different components found within a sample. A standard k-means clustering algorithm ((Lloyd, 1982), chapter 4) is used to automatically determine the position of components from the multi contrast MR images (section 5.2.1). The distribution was corrected manually to correct for artefacts in the results from the k-means algorithm.

The finite element package SEPRAN (Ingenieursbureau Sepra, Leidschendam) was used to calculate the displacement field corresponding to the experiment. The material was assumed to be nearly incompressible, with a Poisson ratio of $\nu = 0.49$.

5.2.4 Parameter estimation

The difference between the experimental results and the computational results is minimised by the estimation algorithm that iteratively adjusts the material properties, used in the numerical experiment.

3D digital image correlation provide displacements in 3 dimensions at N measurement points, that are stored in a column $\underline{u} = [u_1, \dots, u_N]^T$. Given a set of P material parameters $\underline{\theta} = [\theta_1, \dots, \theta_P]^T$, and the prescribed force, f , the response \underline{h} is calculated. The estimation algorithm is aimed at minimising the difference between $\underline{h}(\underline{\theta}, f)$ and \underline{u} . The relation between the measured displacements \underline{u} and the calculated displacements

\underline{h} can be written as:

$$\underline{u} = \underline{h}(\underline{\theta}, \underline{f}) + \underline{\xi} \quad (5.1)$$

where $\underline{\xi}$ is an error column, that may consist of measurement errors and modelling errors. To quantify the quality of this agreement an objective function of a quadratic form is defined:

$$J(\underline{\theta}) = [\underline{u} - \underline{h}(\underline{\theta}, \underline{f})]^T \underline{V} [\underline{u} - \underline{h}(\underline{\theta}, \underline{f})] + [\underline{\theta}^{(0)} - \underline{\theta}]^T \underline{W} [\underline{\theta}^{(0)} - \underline{\theta}] \quad (5.2)$$

The first term in the right hand side accounts for the difference between measured and calculated response, while the second term accounts for the difference between the initial and the current parameter. \underline{V} and \underline{W} are two positive definite symmetric weighting matrices in which the confidence in respectively the measurements and the initial estimates is represented. Since in this study it is assumed no a priori information is known, \underline{W} is set to zero.

For the minimisation of this objective function a Gauss-Newton algorithm is applied. The iterative procedure is continued until parameter changes are smaller than a critical value

$$\sqrt{\delta \underline{\bar{\theta}}^{(i)T} \delta \underline{\bar{\theta}}^{(i)}} < \delta_{\theta}, \quad (5.3)$$

where δ_{θ} is set to 10^{-3} and $\delta \underline{\bar{\theta}}^{(i)T}$ is defined as

$$\delta \underline{\bar{\theta}}^{(i)T} = [\delta \underline{\bar{\theta}}_1^{(i)}, \dots, \delta \underline{\bar{\theta}}_P^{(i)}], \quad \delta \underline{\bar{\theta}}_j^{(i)} = |\delta \underline{\bar{\theta}}_j^{(i)}| / |\underline{\bar{\theta}}_j^{(i)}|, \quad j = 1, \dots, P \quad (5.4)$$

For more details about the estimation algorithm the reader is referred to Meuwissen (1998) and Cox et al. (2006).

5.3 Validation

The validation procedure is split into two steps. In the first step an experiment is simulated. This controlled situation is used to study the influence of noise on the parameter estimation procedure. In the second step the experimental data from a uniaxial load test on the hydrogel sample are used to estimate the material properties of the hydrogels.

5.3.1 Simulation

In the first step of the validation experimental results are generated using a finite element computation. The mesh is based on the experimental MR images (Fig. 5.4b). The displacements of boundary surface, S_1 , is fixed to zero in all directions, while a uniformly distributed force of 1N in z-directions is applied to boundary surface S_2 .

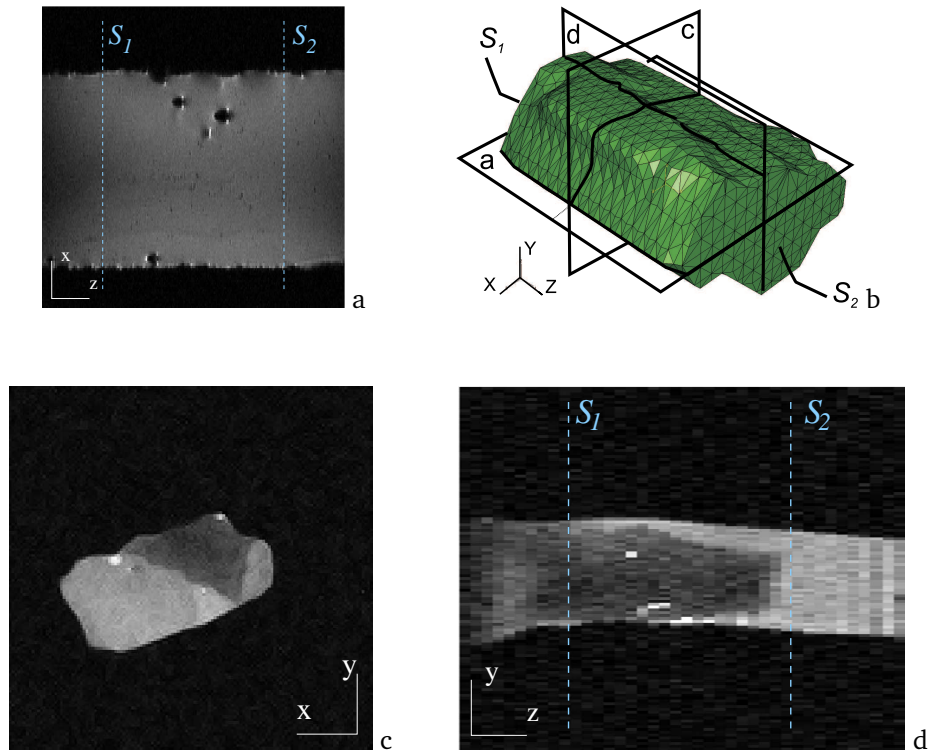


Figure 5.4: T1 image in which the area used to create a mesh is indicated(a). Image of the created mesh (b) and the two cross sections (c,d) obtained from the T2 image set indicated in (b) to show the position of the embedded hydrogel

The Young's modulus of material 1, E_1 is set to 0.5 MPa and of material 2, E_2 is set to 0.2 MPa. The displacement fields are calculated and used in the parameter estimation.

Three different parameter estimations are performed. First, the artificially obtained displacements are used directly. Second, the displacements are disturbed with normal distributed uncorrelated noise with a standard deviation of 10% of the maximum displacement. Finally, the displacements are disturbed with normal distributed uncorrelated noise with a standard deviation of 25% of the maximum displacement.

Initial guesses for the parameters are 1.0 MPa and 0.1 MPa for E_1 and E_2 respectively.

5.3.2 Results simulation

Both the initial and final parameter estimates and the estimation errors are summarised in table 5.2.

In the 0% noise situation, the final estimates of the parameters are equal to the exact values. The parameters converge to the exact values within 3 iterations. Errors in the estimated parameter values result from noise disturbance of the displacements. For the 10% noise situation a small error is found. Within 4 iterations convergence was obtained. The error increases when 25% noise is introduced, but still the value is reached within 4 iteration steps.

The estimated standard deviations of the displacement residuals for the 10% and 25%, divided by the maximum displacement, are 0.071 and 0.251 respectively and are close to the standard deviations of the artificial noise .

Input value	Initial guess	0% noise	10% noise	25% noise
		Final estimate	Final estimate	Final estimate
0.5	1.0	0.500	0.498	0.511
0.2	0.1	0.200	0.199	0.197

Table 5.2: Results for the simulated experiment.

5.3.3 Experiment

The boundary conditions as described in section 5.3.1 cannot be applied in this situation. The mesh made from the central 20 mm of the 3D MR image (section 5.2.3) is used. The parts that are not meshed do however deform in the loaded state (Fig. 5.5). This results in a deformation of the surfaces S_1 and S_2 . In the computations these deformations, as a result of the applied force, should be used. This can be done by applying the deformation at the surfaces S_1 and S_2 as the boundary conditions and calculate the force needed to achieve that deformation. The displacement and deformation of both surfaces are obtained from the image correlation data and are described as a function of the x and y coordinates.

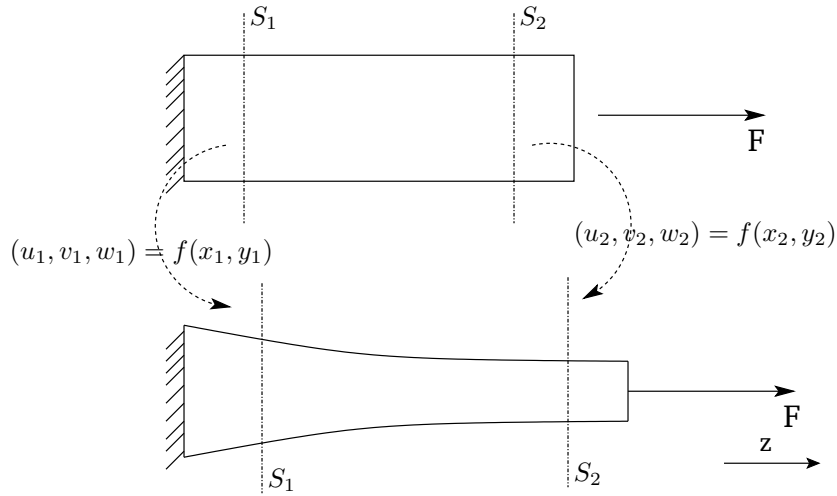


Figure 5.5: Boundary conditions for the finite element model of the hydrogel experiment.

When these boundary conditions are applied, an infinite number of solutions for the set of Young's moduli $E_{calc,i}$ exists, where $i = 1, \dots, N$ with N the number of materials. For each of these solutions the ratio between $E_{calc,i}$ and $E_{calc,j \neq i}$ will be the same. This holds only for small deformation and linear elastic material behaviour. The absolute value of the Young's moduli is determined by use of the resulting force on the load surface F_{calc} . Since the force, applied in the experiment, F_{exp} is known, the Young's moduli of the experimental sample, the absolute $E_{exp,i}$ can be obtained by

$$E_{exp,i} = E_{calc,i} \cdot \frac{F_{exp}}{F_{calc}} \quad (5.5)$$

To have an infinite number of solutions, however, leads to numerical instabilities and therefore one of the Young's moduli is set to a fixed value, leaving only one solution remaining. The ratio between the Young's moduli found is independent of the fixed value.

To test the systems robustness, the Young's moduli, $E_{exp,i}$, have been determined for two different initial guesses for $E_{calc,1}$ ($E_{calc,1} = 0.1$ MPa and $E_{calc,1} = 1.0$ MPa). The fixed value for $E_{calc,2}$ was set to 0.5 MPa. Additionally, the fixed value $E_{calc,2}$ was changed to 0.1 MPa and the estimation algorithm was applied with in initial guess of $E_{calc,1} = 0.1$ MPa. The results of these three calculations should be equal.

5.3.4 Results experiment

The parameters $E_{exp,1}$ and $E_{exp,2}$ were determined with two different initial guesses for $E_{calc,1}$. The results (E_{calc} , F_{calc} and $E_{exp,i}$) are shown in table 5.3. In both situations the same result for $E_{calc,1}$ is reached. $E_{exp,1}$ and $E_{exp,2}$ were determined with

Fixed value	initial guess	final			
$E_{calc,2}$	$E_{calc,1}$	$E_{calc,1}$	Fz [N]	$E_{exp,2}$	$E_{exp,1}$
0.5	0.1	1.45	2.2	0.23	0.67
0.5	1.0	1.45	2.2	0.23	0.67
0.1	0.1	0.29	0.43	0.23	0.67

Table 5.3: Estimated moduli [MPa] for hydrogel experiment determined using Eqn. (5.5).

Eqn. (5.5). When a different fixed value for $E_{calc,2}$ is chosen, the resulting force is different, but $E_{exp,1}$ and $E_{exp,2}$ do not differ from the first two tests.

To give an indication of the fit results the displacements u observed in the experiment are given in figure 5.6. Displacements in x, y and z direction are plotted (grey line) against their z-position in the sample. In the same figures the corresponding fitted displacements \hat{h} are plotted in black lines. Although the experimental data shows more noise, the fitted parameters describe the displacement field in a satisfying way. Convergence of the estimation algorithm was reached within 6 iterations.

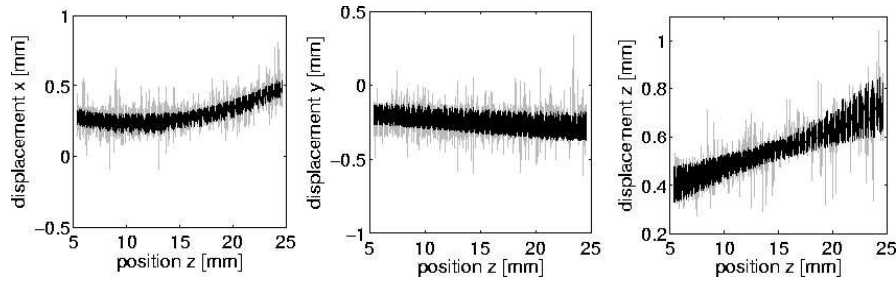


Figure 5.6: Observed (Grey line) and calculated (black line) displacements in x, y and z directions plotted at the z position in the sample.

5.4 Discussion

A simulated experiment has been used to show that the parameters estimation algorithm is capable of fitting the Young's moduli well even when noise is present. The Young's moduli, that were to be fitted in the validation, were both chosen in the same order of magnitude (0.5 MPa & 0.2 MPa). This method is developed for determination of the local mechanical properties of AAA vessel wall in which one might encounter calcified deposits. Marra et al. (2006) reported shear moduli for isolated calcifications of 23 GPa whereas the Young's modulus of vessel wall is estimated to be 0.5-1 MPa (Inzoli et al., 1993; Mower et al., 1997; Wolters et al., 2005). Elasticity coefficients for calcified tissue (no isolation of the deposits) of coronaries and iliac arteries range

from 1.5 MPa to 19 MPa (de Putter et al., 2006b). These values are still about two orders of magnitude larger than the vessel walls modulus.

To ensure that a large difference in magnitude of the parameters is not a problem for the estimation algorithm a second experiment has been simulated (as described in section 4.1). In this experiment the entire mesh was assigned to be material 1, with $E_1 = 0.2$ MPa, except for a small strip of material 2 with $E_2 = 20$ MPa (Fig. 5.7). The influence of noise was studied in a way similar to that described earlier. The results in table 5.4 show that the estimation algorithm has no problem determining such large differences in mechanical properties even when the initial guess for Young's modulus of the calcified area is chosen in the range of average vessel wall Young's modulus.

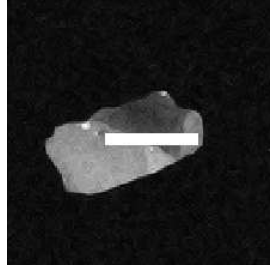


Figure 5.7: A small strip in the sample is set to a Young's modulus that might be expected for a calcified area of a AAA vessel wall.

		0% noise	10% noise	25% noise
Input value	Initial guess	Final estimate	Final estimate	Final estimate
0.2	0.5	0.200	0.200	0.200
20	0.5	20.00	18.896	19.015

Table 5.4: Results for simulated experiment 2: calcified area in tissue

The parameter estimation of the experimental data leads to $E_{exp,1} = 0.67$ MPa and $E_{exp,2} = 0.23$ MPa, whereas the values determined from normal tensile testing was $E_1 = 0.38$ MPa and $E_2 = 0.25$ MPa. Although the order of magnitude does agree $E_{exp,2}$ is slightly lower, while $E_{exp,1}$ is higher than determined in the tensile test. This could be a result of an inaccuracy of the mixed numerical experimental method, but it is also likely that the Young's moduli of the two merged hydrogels do not agree with their individual moduli. The material properties of hydrogels are determined by their amount of water. When one hydrogel is embedded in the other, transport of water between them is possible. Transport of water would change the amount of water in both hydrogels and therefore change their mechanical properties. Dehydration is another possible reason for the increase in stiffness.

Incompressibility is assumed in the parameter estimations. The Poisson ratios were set to 0.49. When the Poisson ratios are estimated as well, they change to $\nu_1 = 0.47$ and $\nu_2 = 0.39$. Young's moduli are influenced by this change and changed to $E_{exp,1} = 0.64$ MPa and $E_{exp,2} = 0.28$ MPa. The difference in Poisson ratio between the two hydrogels could be the result of a difference in water content of the two hydrogels. Although the Young's moduli are influenced by the fitted Poisson ratio, it might not be possible to fit the Poisson ratio in AAA vessel wall. Estimation of the Poisson ratio takes more effort than the estimation of the Young's moduli. After 25 iterations the changes in parameters per iteration were larger than $1 \cdot 10^{-3}$, while this was reached for the Young's moduli estimations within 4 iterations.

The displacements in the transversal direction are important for the determination of the Poisson ratio. These displacements are small compared to the displacements in the axial directions and therefore have a poorer signal to noise ratio. This effect can be demonstrated by fitting the Poisson ratio on the displacement data of the simulated experiment of section 5.3.1 in which 10% noise was added. Poisson ratios do not converge to the value of 0.49 used in the initial simulation, but to $\nu_1 = 9.2 \cdot 10^{-2}$ and $\nu_2 = 0.499$. Although this second value is near the actual value, the limit for this parameter was set to 0.499. Because of the difficulties in fitting the Poisson ratios, they can best be set to a reasonable value.

In the current work linear elastic material parameters are determined for all materials. The method could be extended to other material models. This would require implementation of the desired material model in the numerical part and replacement of the uniaxial tensile test by a test that would provide the information to obtain the subsequent material parameters.

Vande Geest et al. (2006) used biaxial tensile tests to show that the degeneration of AAA vessel wall is associated with an increase in anisotropy. Since 3D data is available after the experiment as proposed in this work, implementing anisotropy in the model would suffice to draw conclusion about local anisotropy. When needed the experiment could be extended to biaxial testing. The small bore of the 6.3T scanner used restricted the experiments to uniaxial testing in this work. Furthermore, when the deformation is followed over time, it might be possible to draw conclusions about the non-linear or time dependent behaviour of the material.

It has been shown that the mixed numerical experimental method proposed is a robust way to estimate the order of magnitude of material parameters. The method is insensitive to initial estimates of the parameters.

Chapter 6

Local Mechanical Properties of Abdominal Aortic Aneurysms

6.1 Introduction

Rupture risk of abdominal aortic aneurysms based on wall stress analysis has been suggested to be superior to the currently used rupture risk prediction based on the maximum diameter (Fillinger et al., 2002, 2003; Raghavan et al., 2005; Venkatasubramaniam et al., 2004). When such wall stress analysis are performed using patient specific computational models, the shape and diameter of the aneurysm are obtained from CT or MR images. Although it was already shown that wall thickness influences the wall stress distribution, wall thickness is assumed to be homogeneous. In addition to wall thickness also mechanical properties need to be assigned to the vessel wall in such a model. In several studies on patient specific models, the mechanical properties of the vessel wall are assumed to be linear elastic (Inzoli et al., 1993; Hua and Mower, 2001; di Martino et al., 2001; Mower et al., 1997; Scotti et al., 2005; Stringfellow et al., 1987; Vorp et al., 1996, 1998; Wolters et al., 2005). The Young's modulus is either estimated or determined experimentally (di Martino et al., 2001). Alternatively, the stress-strain curve resulting from such experiments can be described by an exponential function (He and Roach, 1994; Thubrikar et al., 2001b) or by a two parameter, hyper elastic, isotropic, incompressible model (Raghavan and Vorp, 2000). The latter also holds for large strains and has been implemented in several studies on the wall stresses in AAA (de Putter et al., 2007; Fillinger et al., 2003; di Martino and Vorp, 2003; Papaharilaou et al., 2007; Raghavan et al., 2000; Raghavan and Vorp, 2000; Raghavan et al., 2005; Venkatasubramaniam et al., 2004; Wang et al., 2002). These models all assume the vessel wall to consist of a homogeneous, isotropic material.

In this work we take into account that AAA vessel wall is not a homogeneous tissue. In chapter 4 it was shown that the vessel wall contains large collagenous areas, but also shows calcified deposits, areas with cholesterol crystals and an adventitial area with large amounts of fat cells. It is likely that the mechanical properties of these tissue types are not the same. Little is known about the mechanical properties of the individual components. Only the mechanical properties of calcifications have been studied. A literature review of de Putter et al. (2006b) shows that the elasticity coefficients for calcified tissue of coronaries and iliac arteries range from 1.5 MPa to 19 MPa. The mechanical properties of isolated calcified deposits have been by studied and were found to be in the range of cortical bone, 20 GPa (Marra et al., 2006).

No research has focused yet on the differences in mechanical properties of the components present within the degrading AAA vessel wall. The material properties of the individual components need to be determined with a method that does not require the isolation of the individual components. For clinical implementation it is of great importance to find a relationship between the MR grey values and the local mechanical properties. Local mechanical properties could then be assigned to the vessel wall in the patient specific wall stress analyses based on the MR findings alone. In chapter 5 it was shown that using the proposed mixed numerical method the mechanical properties of the different components in a sample can be estimated successfully without isolation of the components.

In this chapter the mixed numerical experimental method as described in chapter

5 will be used to determine local mechanical properties of AAA vessel wall samples. First, the distribution of the different tissue types in each sample has been determined with the multi contrast MR sequences as described in chapter 4. Next, a load has been applied to the sample. The deformation of the sample is recorded with 3D MR imaging and image correlation. Next, each experiment is simulated numerically incorporating the tissue type distribution. The material properties of the tissue types are optimised in an iterative procedure until the computed deformations match the deformations recorded in the experiment. An estimation will be given for the Young's moduli of the different components found in the AAA vessel wall.

6.2 Methods

AAA tissue was obtained from 4 patients undergoing elective surgical AAA repair. Because this material is discarded in the normal clinical setting and it is anonymised after the procedure, making tracing back to the patient impossible, informed consent was not required. The procedure was in conformity with the code of conduct for use of human material as stated by the Dutch federation of Biomedical Scientific Societies. Samples were stored at -80°C . Before imaging the samples were thawed in a bath with lukewarm water. Of each vessel wall sample a strip, with a size of approximately $15\text{ mm} \times 30\text{ mm}$, was used for imaging. The sample is attached at two sides to a sample holder (Fig. 4.1). Each sample holder is first glued to the sample and to prevent tearing of the sample, several sutures are made through the sample and the holder. One sample holder is fixed, while a load can be applied to the other. The set-up is oriented horizontally to fit into a 6.3T MR scanner with a 120 mm horizontal bore with a Bruker biospec imaging console. To enable MRI-measurements the housing was encompassed by an 8-legged low-pass birdcage RF coil. To eliminate the deformation caused by gravity on the sample a load of 1N is applied in the reference state.

3D T1 images of the sample are acquired in the reference state, according to the MR sequence parameters in table 5.1. Next, a load of 1.2 N is applied and again a 3D image is acquired. The displacement of the sample, as a result of the applied force, is acquired by digital image correlation of the two MR images (Section 5.2.2). The window size and search area were chosen to be $13 \times 13 \times 13$ voxels. The search volume is $25 \times 25 \times 25$ voxels large and is based on the maximum displacements expected. Displacement of approximately 4000 points is taken into account. The selection procedure is described in section 5.2.2.

The 3D image of the reference state was used with the marching cubes algorithm to generate a mesh (Section 5.2.3). To avoid the possible effects of the holders on the tissue deformation, the mesh edges are positioned 2 mm from the sample holders. The position of the holders was determined from the MR images.

Mechanical properties should be assigned to each node of the mesh, based on the tissue type in the sample at the position of the node. As was concluded in chapter 4, a clustering algorithm alone is not sufficient to determine the distribution of the different tissue types. In this work the samples were manually divided into 'clusters'

of materials based on T1w and T2w MR images. A custom made routine first puts the entire vessel wall in one cluster. Then it allows the user to select, in each MR slice, areas of voxels that should be in one cluster and assign a cluster number to this area. Of each such a cluster the Young's modulus is to be estimated.

	media	adventitia	thrombus	calcification	cholesterol
T1w	+	+	+	--	-
T2w	-	+	+	--	-

Table 6.1: Appearance of the selected components in T1w and T2w MR images

Table 6.1 summarises the brightness of the components in T1w and T2w images. First the T2 images were reviewed and the dark band that forms a major part of the media is selected to be the second cluster. Although it is not certain that this dark band is the entire media, it is entitled 'media' from now on. Then the T1 images are reviewed. The adventitial side of the vessel wall, that is more bright than the media in the T1 images is assigned to a separate cluster. Again, it is not certain that this bright area is the entire adventitia but it is located at the adventitial side of the media and is thus named 'adventitia' in this work. In sample 1 (Fig. 6.1a and b) the dark area that was found to exist of cholesterol crystals (chapter 4) is selected as a separate cluster. The area has a dark cloudy structure in the T1w and T2w images which distinguishes it from the calcified areas. A calcification can be recognised as a completely dark layer in the media. Sample 2 (Fig. 6.1c and d) shows a layered structure, with (from top to bottom) remains of thrombus, media, a region that is more bright than the media and probably part of the adventitia (the adventitia side in Fig 6.1e), and an even more bright area that probably only exists of fat cells (adventitia). In parts of the sample small calcified deposits were found. Although the MR appearance of thrombus is similar to that of the adventitial area it can be distinguished by the position in the sample. In sample 3 (Fig. 6.1e and f), the calcified area is a separate cluster. In sample 4 (Fig. 6.1g and h), the intimal side of the vessel together with the remains of thrombus form a cluster.

For each sample the average Young's modulus was estimated. To do so, all clusters were merged into one. The Young's moduli of all clusters in a sample were estimated. To check the reliability of the estimates and to check the influence of the surrounding tissue on the estimated values, three additional tests were done. In these tests, 2 clusters were merged and an average of these two was estimated together with the Young's modulus of the remaining, separate cluster. When the sample is divided into three clusters, the merging of two clusters can be done in three different ways. All tissue types were assumed to be linear elastic, nearly incompressible with a Poisson's ratio of 0.45. The finite element package SEPRAN (Ingenieursbureau Sepra, Leidschendam) was used to calculate the displacement field corresponding to the experiment, using tetrahedral linear elements. The displacement and deformations of the surfaces S_1 and S_2 (Fig. 6.2) were obtained from the image correlation data and described by a surface as described in figure 5.5. For each sample the average Young's modulus was estimated. To do so, all clusters were merged into one.

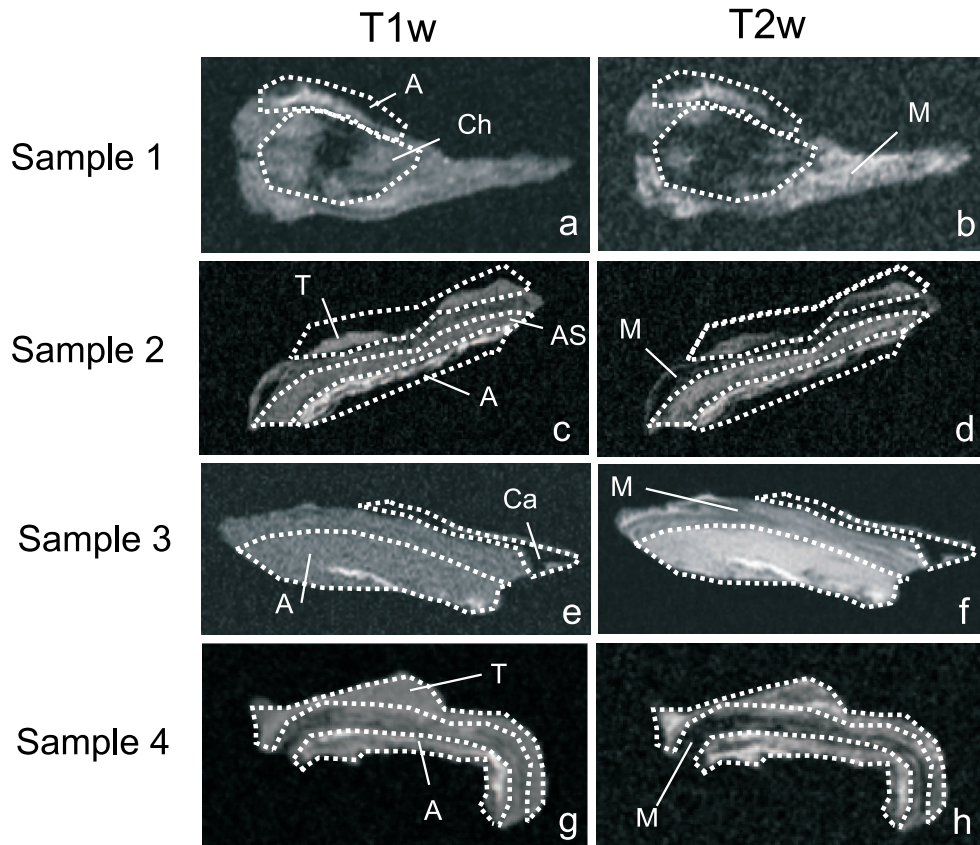


Figure 6.1: Example T1w (a,c,e,g) and T2w(b,d,f,h) slices of the assignment of different tissue types in sample 1 (a,b), sample 2(c,d), sample 3(e,f) and sample 4(g,h). A=adventitia, M=media, Ch=cholesterol, T=thrombus, As=adventitial side, Ca=calcification.

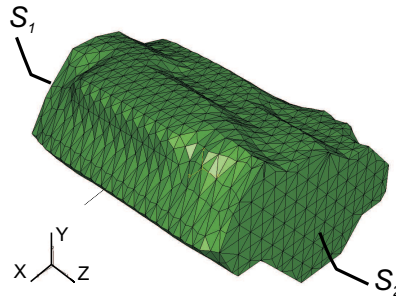


Figure 6.2: Schematic view of a sample with the surfaces S_1 and S_2 at which the boundary conditions are applied

6.3 Results

Per sample, the results of the different estimations are given in table 6.2 to 6.5. For each cluster the percentage of volume of the entire sample is estimated based on the number of nodes in each cluster.

When the Young's moduli for all three tissue types in sample 1 are fitted, cholesterol is found to be approximately 7 times stiffer than the media and adventitia. Adventitia is found to be slightly stiffer than the media (1.37 MPa vs 1.02 MPa). When the media is merged with the adventitia a value is found between their individual values (1.12 MPa). The value for cholesterol does not change a lot, indicating a close fit. When the stiffer cholesterol is assigned to the same cluster as the adventitia (2.68 MPa), also the fitted stiffness of the media increase (1.53 MPa). The stiffness assigned to the neighbouring tissues does influence the values found.

When two or more tissue types were assigned in sample 2, the estimation reached convergence after the first step, regardless the initial guess for the Young's moduli. The dataset is clearly not suitable for the estimations and no further results were obtained. This unsuitability probably originates from bad image correlation results. These may be caused by noise in the MR images or a lack of contrast in the sample.

When three Young's moduli (media, adventitia and calcification) of sample 3 are fitted, the media is found to be less stiff than adventitia (0.27 MPa vs 1.49 MPa). The Young's modulus of the calcification exceeds these values about 50 times (56.1 MPa). When the results for the merged clusters are studied, the modulus of the calcification increases to 94.3 MPa when the media and adventitia are merged. When the calcification is merged with either adventitia or media, the estimated modulus evidently increases; for media merged with calcification $E = 1.69$ MPa, for adventitia merged with calcification $E = 2.28$ MPa.

Sample 4 contains remains of thrombus. For this sample the estimation with 3 separate clusters did not converge. From the results of the merged clusters it is, however, clear that the stiffness of thrombus is a lot lower than the media and adventitia; $E=1.94$ MPa for media and adventitia, while for thrombus $E = 0.04$ MPa. When thrombus is merged with any of the other cluster the fitted, average Young's mod-

ulus of that cluster is influenced by the thrombus and decreases; for media merged with thrombus, $E = 0.16$ MPa, adventitia merged with thrombus $E = 1.03$ MPa. The modulus of cluster that did not contain thrombus increases with respect to the value for the merged media/adventitia; for media separately, $E = 1.49$ MPa, for adventitia separately, $E = 3.4$ MPa.

A coarse estimation was made for the Young's moduli by assuming the samples only consisted of one tissue type. The moduli range from 1.15 MPa to 1.91 MPa.

sample 1	media	adventitia	cholesterol
volume %	77.6%	9.7%	12.7%
1 cluster	1.91		
2 clusters, media merged with adventitia	1.12		7.41
2 clusters, media merged with cholesterol	1.64	2.61	1.64
2 clusters, cholesterol merged with adventitia	1.53	2.68	
3 clusters	1.02	1.37	7.51

Table 6.2: estimated Young's moduli (MPa) for sample 1.

sample 2	media	adventitial side	adventitia	intima/thrombus	calcification
volume %	25.1%	27.3%	23.0%	23.2%	1.5%
1 cluster	1.44				

Table 6.3: estimated Young's modulus (MPa) for sample 2.

sample 3	media	adventitia	calcification
volume %	43.0%	49.3%	7.7%
1 cluster	1.35		
2 clusters, media merged with adventitia	0.59		94.3
2 clusters, media merged with calcification	1.69	0.98	1.69
2 clusters, adventitia merged with calcification	0.34	2.28	
3 clusters	0.27	1.49	56.1

Table 6.4: estimated Young's moduli (MPa) for sample 3.

6.4 Discussion

A mixed numerical experimental method was used to determine the Young's modulus of different tissue types, found in the AAA vessel wall. The average Young's moduli for

sample 4	media	adventitia	intima/ thrombus
volume %	23.6%	31.4%	45%
1 cluster	1.15		
2 clusters, adventitia merged with thrombus	1.49	1.03	
2 clusters, media merged with thrombus	0.16	3.40	0.16
2 clusters, media merged with adventitia	1.94		0.04
3 clusters	no convergence		

Table 6.5: estimated Young's moduli (MPa) for sample 4.

the sample varied from 1.15 to 1.91 MPa. Calcification was found to be two orders of magnitude stiffer than the average vessel wall. A cholesterol rich area was one order of magnitude stiffer. Conversely, thrombus is at least one order of magnitude less stiff than the vessel wall. The low value for the Young's modulus of thrombus is confirmed by earlier work (van Dam et al., 2006, 2007). The Young's moduli of isolated calcifications were estimated to be around 20 GPa (Marra et al., 2006), which is two orders of magnitude higher than the values reported in this work (50 MPa). The area that was defined as calcification in this work is, however, likely to contain some surrounding tissue with a much lower stiffness. The resulting Young's modulus will then be an average of the modulus of the calcified deposits and the surrounding tissue and would explain the value of the calcifications in this work. A similar but opposite effect influences the value found for thrombus. The Young's modulus reported for thrombus was ≈ 40 kPa, while the shear modulus reported in chapter 3 was even an order of magnitude lower. The value reported in this work is likely to be influence by surrounding tissue that was assigned the thrombus cluster.

Errors from several different sources influence the experimental results. Noise that occurs in the MR images influences both the image correlation resolution, the meshing algorithm and determination of the morphology of the samples. Although only points with a high correlation are selected from all the positions in the original image that were searched in the loaded image, one cannot be sure that all image correlation data are correct. The contrast distribution of the samples that are degenerated most leads to better results than image correlation of well-structured vessel wall. In the latter the structure does not change much in the direction of the applied force and the uniqueness of contrast distribution in the selected windows becomes a problem. An example of such a sample, which was an additional fifth sample in this study, is given in figure 6.3. Three adjacent slices are very similar and the lack of contrast in the direction of the applied force results in bad image correlation results (Fig. 6.4). Hardly any displacement can be distinguished from the image correlation data in the z direction, the direction of the applied force.

The resolution of the mesh should be chosen carefully. Some tissue types, like the calcified deposits, only take up a small volume. To be able to determine the mechanical properties the mesh resolution should be sufficiently high, but to reduce computational time in the iterative fitting procedure mesh resolution should be kept as low

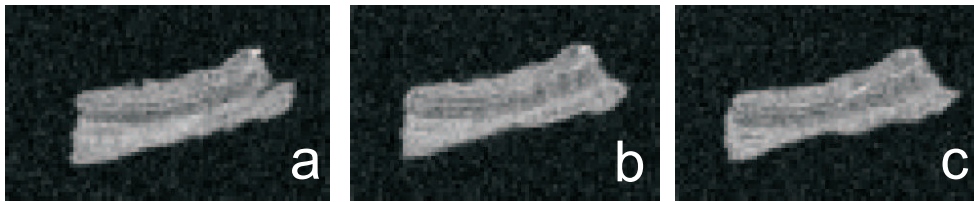


Figure 6.3: Three adjacent slices of a sample in which image correlation did not find any displacement. As can be seen little contrast is present. The slices are 1 mm thick and the three slices cover 3 mm together. The range of the displacement magnitude is expected to be smaller than 3 mm.

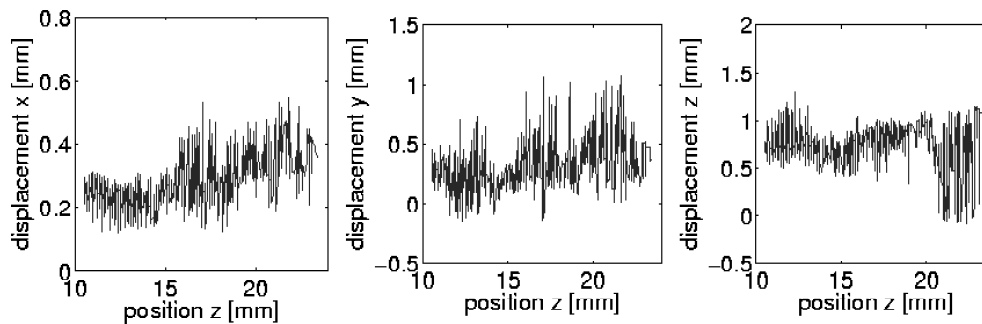


Figure 6.4: The image correlation results for the sample in figure 6.3. Although the force is applied in z direction no displacement in this direction can be distinguished from the noise.

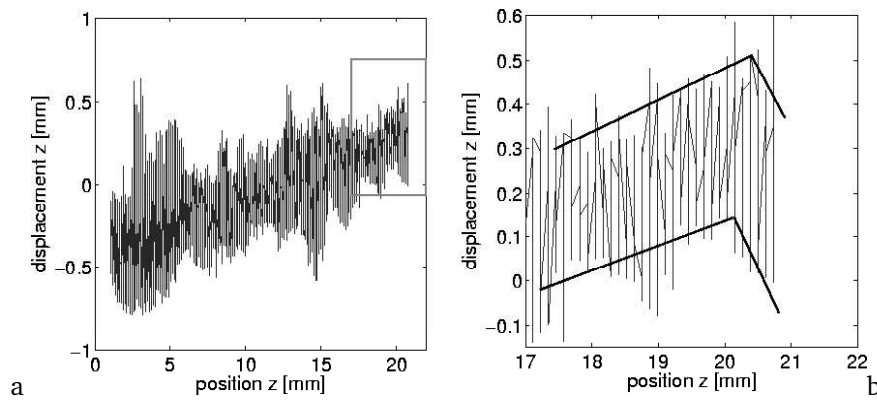


Figure 6.5: The displacement in sample 4 in z direction (a). The boundary conditions are determined from this data. The displacements near the maximum z -positions are enlarged in the right image (b). The sudden decrease in displacement at the maximum z position leads to false boundary conditions. The solid lines indicate the range of displacements at a certain position along the z -axis

as possible. The calcification in sample 3 was only 7.7% of the total volume and was covered by 1320 nodes. The material properties were estimated successfully. The calcification of sample 2 represented only 1.5% of the sample and 119 nodes. This may be too few nodes to accurately describe the actual displacements of the calcification volume. It is plausible that this may lead to errors in the estimation. The estimation of the material properties of sample 2 did, for inexplicable reasons, not lead to unique estimations, even when the calcification was merged with another tissue type. The boundary conditions applied in the computational study are obtained from the image correlation data. At the two boundary surfaces S_1 and S_2 (Fig. 6.2) the displacements are described as a linear function of the image correlation data at that position. The surfaces are, however, near the edges of the 3D MR images. The image intensity is less at the edges and this may lead to decreased image correlation performance. Figure 6.5 depicts such image correlation results. The displacements in z -direction found by image correlation near S_2 suddenly decrease as indicated by the solid lines, that depict the range of displacements found. A decrease in displacement physically means local shrinking of the sample, which is very unlikely. To overcome this problem a new mesh was made for this sample in which the problematic area was omitted and surface S_2 was located at a position within the range of credible image correlation results. For all samples the correctness of the boundary conditions was verified in a similar way.

The tissue is assumed to be nearly incompressible and therefore, the Poisson ratio was chosen to be 0.45. As was described in chapter 5, it is difficult to estimate the Poisson ratio. When a Poisson ratio estimation is attempted for the AAA vessel wall samples the parameter estimation algorithm does not converge. To determine the error that is introduced by assuming a Poisson ratio of 0.45, the Young's moduli of

the components of sample 3 are also estimated with a Poisson ratio of 0.3 for the calcified area. A value of 0.27 for calcified deposits was reported by Marra et al. (2006) and was based on the value of cortical bone. The estimated Young's modulus of the calcification in sample 3 changes to 54.6 which is a difference smaller than 3%. The changes in Young's moduli of the other two components are less than 1%. The error that is introduced by setting the Poisson ratio to 0.45 is negligible.

The samples were divided into several clusters that represent a tissue type based on the T1w and T2w MR images. Table 6.1 indicated that MR appearance alone is not sufficient to make a division into these clusters. Since the clusters are not directly related to MR grey values it is not possible to relate the MR grey values to the material properties found. For clinical implementation it is of great importance to find this relationship. Local mechanical properties could then be assigned to the vessel wall in the patient specific wall stress analyses based on the MR findings alone. The image correlation data of 2 samples was for several reasons not suitable for estimation of the Young's moduli. To apply the method unconditionally, the method requires improvements in the field of the subjects, described in this discussion. It can, however, be concluded that the mixed numerical experimental method as was proposed in chapter 5 can successfully estimate local mechanical properties of inhomogeneous AAA vessel wall.

Figure 6.6 reflects the results obtained in this work. It should be noted, though, that these results were obtained from three samples. Only one sample contained calcifications, and thrombus and cholesterol crystals were also present in only one sample. The Young's moduli of thrombus (T), media and adventitia (M/A), cholesterol (Ch) and calcifications (Ca) are distributed over four orders of magnitude. Since each of these tissue types covers another order of magnitude it is plausible that detection of

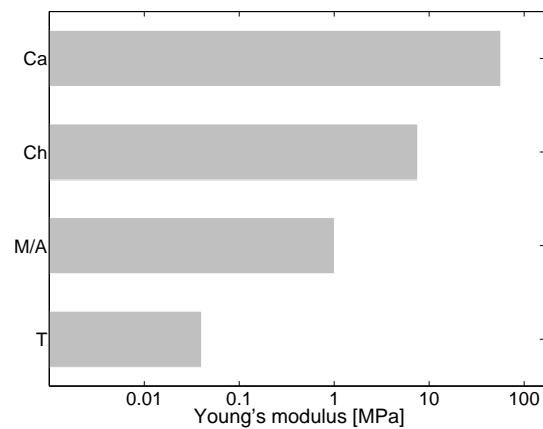


Figure 6.6: The resulting Young's moduli plotted on a logarithmic scale for the different tissue types. Ca=calcification, Ch=cholesterol, M=media, A=adventitia, T=thrombus.

these tissue types in a patient specific way is of great importance for the rupture risk analysis. The implications of these findings on the patient specific wall stress analysis will be studied in the next chapter.

Chapter 7

General Discussion: Towards Rupture Risk Analysis

7.1 Introduction

AAA rupture risk prediction based on wall stress analysis requires a good description of the mechanical properties of the vessel wall and the thrombus. Until now the inhomogeneity of the vessel wall was disregarded, while it was shown that this might have great influence on the resulting wall stress (Inzoli et al., 1993). The objective of this study was to obtain the local mechanical properties of both AAA vessel wall and thrombus.

In chapter 2 thrombus was divided into the luminal, medial and abluminal layers based on their colour and structure. The linear viscoelastic properties of the luminal and medial layer were determined with a rotational rheometer using a parallel plate geometry. The reproducible results confirmed the applicability of the method to thrombus tissue.

In chapter 3 this method was extended to the non-linear strain regime. The changes in mechanical properties throughout the thickness of the thrombus are different for each thrombus and the variations within one thrombus are of the same order of magnitude as the variations between patients. The variations could not be related to the structure of the tissue which was studied by ESEM images. The shear modulus (1.7 ± 1.3 kPa) found is an order of magnitude lower than reported by others in literature. The phenomena observed in the small and large strain experiments were successfully described by a non-linear multi mode model.

Chapter 4 focused on the morphology of the vessel wall and the use of multi contrast MRI to discriminate the components of the vessel wall. Multi contrast MR results were compared to the golden standards, histology and μ CT. Components like the media, calcified deposits, areas containing cholesterol, thrombus and the adventitia containing fat cells and vasa vasorum could be recognised in the MR images. The results obtained so far were not suitable for an automatic classification by an unsupervised clustering algorithm.

To obtain the mechanical properties of the components present in the vessel wall a mixed numerical experimental method was proposed in chapter 5. This method is a robust way to determine the mechanical properties of the individual components without having to isolate them.

In chapter 6 this method was applied to AAA vessel wall samples. The morphology was obtained with multi contrast MR. The Young's modulus of media, adventitia, calcification, an area with cholesterol crystals and thrombus were determined. Although the media is less stiff than the adventitia the moduli were in same the order of magnitude (≈ 1.0 MPa). The stiffness of thrombus was found to be an order of magnitude lower (≈ 40 kPa). An area with a lot of cholesterol is stiffer than the rest of the wall (≈ 7.5 MPa) and a calcified area is even stiffer (≈ 50 MPa).

These results were obtained from a limited number of samples and these were all acquired from patients undergoing elective surgical AAA repair. Since the endovascular repair techniques gain in popularity, the number of open repairs decreases. Patients that do undergo such a surgical repair do not meet the requirements of the endovascular repair and are, in general, the more complex cases. Samples used in this research may not be representative for all aneurysm tissue. Samples of smaller aneurysms

were, however, not available. The material properties reported in this work range from a shear modulus of thrombus of 1.7 kPa to a Young's modulus for a calcified area of 50 MPa. Implementation of these values might have a large influence on the outcome of patient specific wall stress analyses.

7.2 Implication for wall stress analyses

The shear modulus of thrombus reported in this work is an order of magnitude lower than values reported in literature before (chapter 3). To study the effect of thrombus on wall stress analyses, finite element meshes were created with the hemodyn package (de Putter et al., 2005) based on the CT datasets of 2 patients. An average peak systolic pressure of 16 kPa is applied. The wall is assumed to be linear elastic with a shear modulus, G_{wall} of 1 MPa and the wall thickness is assumed to be uniform (2 mm). Since the viscous part of the thrombus behaviour is low compared to the elastic behaviour, linear elastic material properties (shear modulus $G_{\text{thrombus}} = 10$ kPa) are used in this preliminary study. Wall stress distribution for both patients are compared with and without thrombus. An additional analyses was made with a shear modulus of 100 kPa, a value that agrees with those reported in literature, referred to as 'stiff thrombus'. The maximum principal stress distributions are not largely influenced by the presence of thrombus (Fig. 7.1).

The peak stress and the 99 and 95 percentiles (Table 7.1) are influenced for both patients by the presence of thrombus. The effect of the thrombus with $G_{\text{thrombus}} = 10$ kPa, as reported in this work is much lower than the 'stiff thrombus'. These results

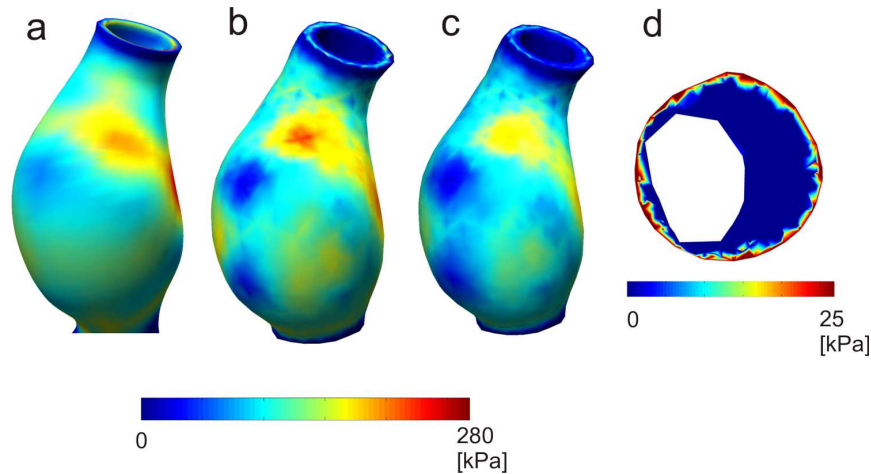


Figure 7.1: Wall stress distributions from patient 1, without thrombus, with thrombus ($G_{\text{thrombus}} = 10$ kPa and with 'stiff thrombus' $G_{\text{thrombus}} = 100$ kPa). A cross section of (b) at the maximum diameter shows that the stresses in the thrombus are very low (d).

Patient 1	No thrombus	thrombus	stiff thrombus
kPa	-	10	100
Peak stress	271	232 (-14%)	203 (-25%)
99 percentile	214	190 (-11%)	165 (-23%)
95 percentile	179	167 (-7%)	145 (-19%)
comp.time	3 hours	10 hours	10 hours
Patient 2	No thrombus	thrombus	stiff thrombus
kPa	-	10	100
Peak stress	592	481 (-19%)	310 (-48%)
99 percentile	254	229 (-10%)	172 (-32%)
95 percentile	211	195 (-8%)	136 (-36%)
comp.time	3 hours	12 hours	11 hours

Table 7.1: Effect of thrombus on peak wall stress and 99 and 95 percentiles

show that the effect of thrombus in the wall stress is overestimated in literature. Since the influence appears to be small it should be considered to neglect thrombus. Computing the wall stresses without thrombus greatly decreases computational time and simplifies mesh generation, which are important benefits when applied clinically. The material properties of the vessel wall may be of greater importance for the peak stress development than the presence of thrombus. In chapter 6 the mechanical properties of several components of the AAA vessel wall were determined. The adventitial side of the thrombus was found to be slightly stiffer than the media, within the same order of magnitude. The stiffness of an area with cholesterol crystals was one order of magnitude higher than the medial and adventitial stiffness. The largest difference with the media and adventitia was found for a calcified area. The high stiffness of calcifications, that comprises only a small part of the vessel wall is expected to have a large influence on the peak stresses in the vessel wall. Calcifications are therefore likely to have larger influence on the wall stress distribution than the other vessel wall tissue types. Furthermore calcifications can, in contrast to the other tissue types, currently be detected in a patient specific way by CT imaging. The implication for the wall stress analysis of the findings for calcification in literature and in this work will be compared.

Marra et al. (2006) isolated the calcified deposits and determined a Young's modulus of 23 GPa with nano-indentation. In chapter 6 of this work the Young's modulus was found to be between 50 and 90 MPa, while the Young's modulus for the media and adventitia was approximately 1.5 MPa. High intensity regions in CT images possibly exist of a complex configuration of multiple calcified deposits that can only be detected by ultra high resolution imaging (de Putter, 2006; de Putter et al., 2006b). This is caused by partial volume effects: per voxel the high CT signal of the calcification overrule the low signal of the surrounding tissue in the same voxel. This results in an overestimation of the volume of the calcification. The material properties that hold for a high intensity region in CT is likely to be a combination of the calcified deposits and its direct surroundings. This would explain why the values in this work are

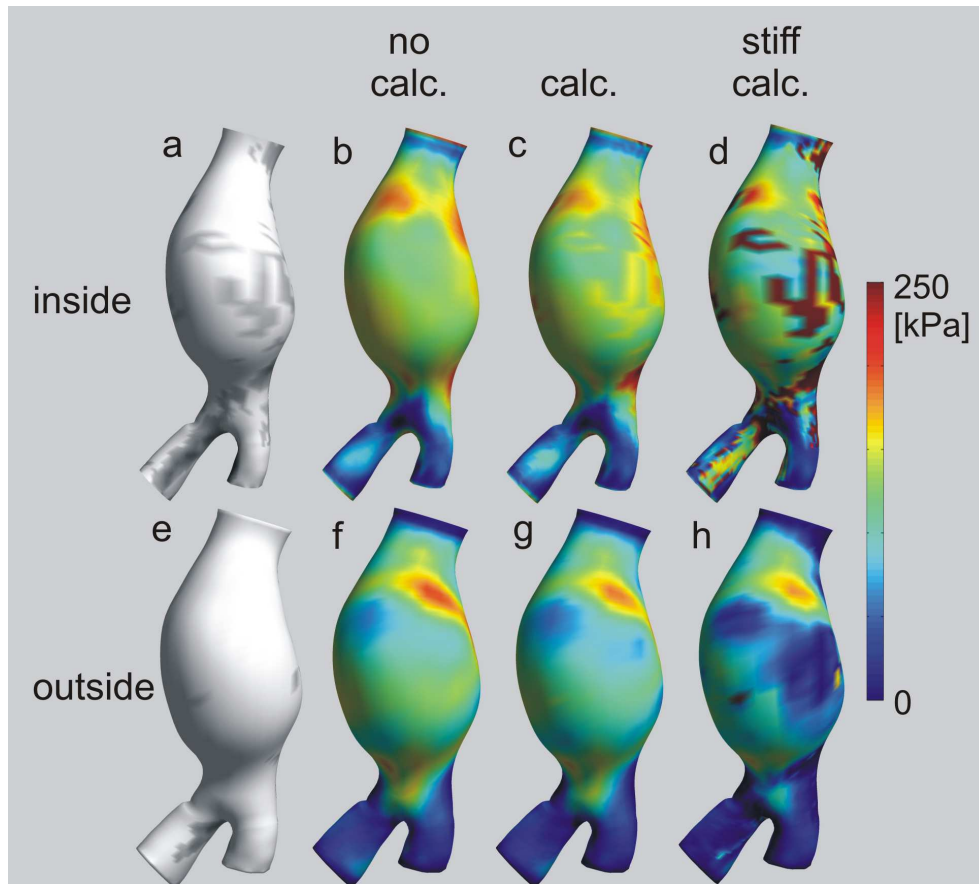


Figure 7.2: Wall stress distributions without calcifications (b,f), with calcifications (c,g) and with 'stiff calcifications' (d,h). The inside (a,b,c,d) and outside (e,f,g,h) layer are depicted separately. The position of the calcification is dark grey in (a) and (e).

lower than those reported by Marra et al. (2006). They used isolated calcifications, while in this work an average value for a calcified area was determined.

To study the influence of calcifications, they are incorporated in the hemodyn model of patient 1 (Fig. 7.1). The vessel wall in this model exists of 2 layers of elements. Each element is assigned to the vessel wall or the calcification based on their brightness in the CT scans. In figure 7.2a the calcifications of the inside layer is depicted; in figure 7.2e the calcification in the outer layer are given. More calcifications are found in the inside layer. This is in agreement with the findings in chapter 4; the calcifications are situated between the media and the intima or thrombus. Wall stress is calculated for a situation without calcification and for two different values for the shear modulus of the calcification, G_{calc} . The first value, $G_{\text{calc}} = 2.75 \text{ MPa}$ is based on

the averaged Young's modulus for the media and calcification. As depicted in figure 6.1, the media and calcification take up the inner half of the sample, while the adventitia takes up the other half. The Young's moduli were estimated for the adventitia and the calcification merged with the media in chapter 6. The Young's moduli are 0.98 MPa for the adventitial side and 1.69 for the medial/calcification side.

The second value implemented, $G_{\text{calc}} = 100$ MPa, is based on the value for the calcified area (chapter 6) and will be referred to as 'stiff calcification'. The shear modulus of the vessel wall is $G_{\text{wall}} = 1$ MPa. The peak wall stress and 95 and 99% percentiles are given in table 7.2. The wall stress distributions are given in figure 7.2 for the inner wall layer (b, c and d) and for the outer wall layer (f, g and h). Near the locations of the calcifications, the effect is very clear. When studying the peak stress and the 95 and 99 percentiles, it is clear that the effect of $G_{\text{calc}} = 2.75$ MPa can be neglected, while for the 'stiff calcification' the peak stress increases enormously. Computational times do not increase when implementing calcifications. When only two layers of

Patient 1	No calcification	calcification	stiff calcification
MPa	-	2.75	100
Peak stress	271	317	2497
99 percentile	214	213	686
95 percentile	179	173	292
comp.time	3 hours	3 hours	3 hours

Table 7.2: Effect of calcification on peak wall stress and 99% and 95 % percentiles

element are used and the stiffness of the calcification is averaged with the media, the effect on the peak stress and 95 and 99 percentiles are very small. When the situation is studied on a local, more detailed scale and the Young's moduli of the media and calcification are not averaged, the stress distribution changes a lot. To study this, the stress distribution in the calcified sample (sample 3 in chapter 6) is studied. The computational experiment that was used in chapter 6 to estimate the material properties is used to show the influence of the effect of calcifications on the stress distribution on a local scale. Two different computational experiments are performed. In the first situation, the 2 layers of the patient specific mesh are mimicked (Fig. 7.3a). The calcifications are merged with the media and the Young's moduli estimated for that situation are assigned (media and calcification $E = 1.7$ MPa; adventitia $E = 0.9$ MPa). The maximum principal stress distribution does not show local effects (Fig. 7.3b). In the second situation 3 clusters (media, adventitia and calcification) are used (Fig. 7.3c). The estimated Young's moduli are assigned to these components. The boundary conditions, as described in section 6.2, are applied. Peak stresses occur near calcifications (Fig. 7.3d).

The presence of calcifications does influence the peak wall stress, but due to the limited resolution of the patient specific meshes the stiffnesses are averaged and the local peak stresses fade. To accomplish a more accurate stress distribution in the vessel wall in case of calcifications the resolution of the mesh should be increased to accurately describe the geometry of the calcification.

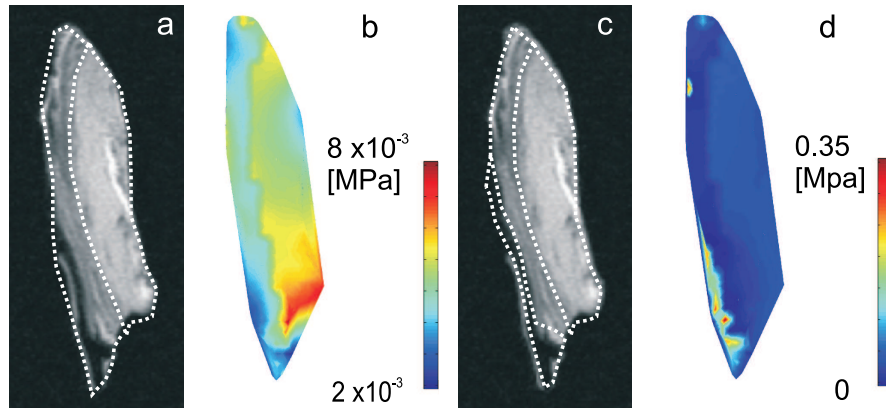


Figure 7.3: The local effect of averaging the calcification with the media (a,b) or incorporating calcification (c,d).

7.3 Limitations for clinical application

Currently, the patient specific models created with the hemodyn package, consist of several thousands of elements (3000-20000, depending on the presence of thrombus). The wall thickness is covered by two elements. In the analysis described in chapter 6 the wall thickness was covered by approximately ten elements. When this kind of detail would be implemented for the entire patient specific model to be able to include calcifications in detail, it would consist of 400 000 to 5 000 000 elements, and computational times would rise immensely.

Resolution is not only a problem in the modelling but also in the imaging of the vessel wall. Images used in this study were acquired with a 6.3 Tesla experimental scanner. Although the available clinical MR techniques still improve, resolutions as used in this study cannot be expected in a clinical setting in the near future. Additionally patient imaging is accompanied by imaging artefacts caused by motion from breathing, heart pulses or general movements.

Even when high resolution imaging would be possible it is clear from chapter 4 that the relationship between MR grey values and tissue type is not clear yet. The results of the clustering algorithm were not satisfying. In chapter 6 the distribution of the tissue types was based on MR grey values but divided into clusters manually. In a clinical setting and with large datasets of the entire aneurysm, manual correction is not feasible.

7.4 Future aspects

Tools have been developed for the determination of local mechanical properties of both AAA thrombus and vessel wall. The results were obtained from a limited number of samples. Especially for the vessel wall more samples should be studied before statistically sound conclusions about the local mechanical properties can be drawn.

In this discussion it was shown that the local mechanical properties are important for the wall stress distribution and that it is technically possible to implement them. It was also shown that implementation in patient specific models is not yet realisable because of limitations in the resolution of both imaging and computing modalities. Besides the resolution problem in the imaging, the image analysis is another problem. Automatic clustering is required for clinical implementation. In chapter 4 a supervised clustering algorithm was suggested as a solution for this problem. A proper algorithm should be chosen and training data should be obtained (Anderson et al., 2007).

The resolution problem in the wall stress computation might be expected to decrease with the development of computational tools. It might be cheaper to implement the local effects of calcifications in a multi level approach. The calcifications should first be studied in detail. Development, morphology, size, position in the tissue and attachment to the tissue are factors that are not understood yet. Possibly, these properties of calcification occur according to predefined patterns. These patterns could be used in a sort of multi-level computation, in which not the actual calcification is implemented but only its effect on the wall stress.

Rupture occurs when wall stress exceeds the strength of the vessel wall. To our knowledge the rupture behaviour of the aneurysm wall has not been described yet. Not only the distribution of the wall stress, but also the strength of the sample is likely to be related to the composition of the sample. In this work the material properties are related to the sample's morphology, but it is also likely that the material strength is related to the morphology. An adapted version of the method proposed in this dissertation could be used in future research on the rupture mechanics of the tissue.

AAA patients do only benefit from this work when the rupture risk prediction based on wall stress analysis improves their treatment and survival rates. Large clinical studies will be needed to determine the relationship between the wall stress and the aneurysm rupture and growth. The results of these studies will determine whether wall stress analysis is a convincing tool for better AAA rupture risk prediction. The contribution of this work consists not only of the reported morphologies and mechanical properties. The observations reported in this work also suggest that effort should be put into development of clinical methods to include the morphology and mechanical properties of the aneurysm into the rupture risk analysis.

References

- R Adolph, DA Vorp, DL Steed, MW Webster, MV Kameneva, and SC Watkins. Cellular content and permeability of intraluminal thrombus in abdominal aortic aneurysm. *J Vasc Surg*, 25:916–926, 1997.
- RW Anderson, C Stomberg, CW Hahm, V Mani, DS Samber, VV Itskovich, L Valera-Guallar, JT Fallon, PB Nedanov, J Huzinga, and ZA Fayad. Automated classification of the atherosclerotic plaque from magnetic resonance images using predictive models. *BioSystems*, in press, 2007.
- DWA Brands. *Predicting brain mechanics during closed head impact -numerical and constitutive aspects-*. PhD thesis, Technische Universiteit Eindhoven, 2002.
- DWA Brands, PHM Bovendeerd, GWM Peters, M Paas, J van Bree, and JSHM Wismans. Comparison of the dynamic behaviour of brain tissue and two model materials. Number 99sc21, pages 57–64. Proc. of the 43th Stapp Car Crash Conference, 1999.
- J Brands. Mechanical characterisation of abdominal aortic aneurysms. Master’s thesis, TUE, 2003.
- M Breeuwer, U Götte, R Hoogeveen, BJBW Wolters, S de Putter, H van de Bosch, J Buth, J-M Rouet, and F Laffargue. Assessment of the rupture risk of abdominal aortic aneurysms by patient-specific hemodynamic modeling - initial results. pages 1090–1095. Proc CARS, International congress series 1268, 2004.
- VC Cappendijk, KBJM Cleutjens, S Heeneman, GW Schurink, R Welten, AGH Kessels, MJAP Daemen, JMA van Engelshoven, and ME Kooi. In vivo quantitative assessment of carotid plaque components with multi-contrast mri. 2002.
- M Carmo, L Colombo, A Bruno, FRM Corsi, L Roncoroni, MS Cuttin, F Radice, E Mussini, and PG Settembrini. Alteration of elastin, collagen and their cross-links in abdominal aortic aneurysms. *Eur J Vasc Endovasc Surg*, 23:543–549, 2002.
- SE Clarke, RR Hammond, JR Mitchell, and BK Rutt. Quantitative assessment of carotid plaque composition using multicontrast mri and registered histology. *Mag Res Med*, 50:1199–1208, 2003.
- LCL Correia, E Atalar, MD Kelemen, O Ocali, GM Hutchins, JL Fleg, G Gerstenblith, EA Zerhouni, and JAC Lima. Intravascular magnetic resonance imaging of aortic atherosclerotic plaque composition. *Arterioscler Thromb Vasc Biol*, 17:3626–3632, 1997.

- MAJ Cox, NJB Driessen, CVC Bouten, and FPT Baaijens. Mechanical characterization of anisotropic planar biological soft tissues using large indentation: a computational feasibility study. *J Biomech Eng*, 128:428,436, 2006.
- S de Putter. *On patient-specific wall stress analysis in abdominal aortic aneurysms*. PhD thesis, Technische Universiteit Eindhoven, 2006.
- S de Putter, M Breeuwer, U Kose, F Laffargue, J-M Rouet, R Hoogeveen, H van den Bosch, J Buth, FN van de Vosse, and FA Gerritsen. Automatic determination of the dynamic geometry of abdominal aortic aneurysm from mr with application to wall stress simulations. volume 1281, pages 339–344. Proc. CARS, 2005.
- S de Putter, M Breeuwer, FN van de Vosse, U Kose, and FA Gerritsen. Patient-specific models of wall stress in abdominal aortic aneurysm - a comparison between mr and ct. volume 6143, pages 111–122. Proc. of SPIE Medical Imaging - Physiology, function and structure from medical images, 2006a.
- S de Putter, FN van de Vosse, M Breeuwer, and FA Gerritsen. Local influence of calcifications on the wall mechanics of abdominal aortic aneurysm. volume 6143, pages 745–755. Proc. of SPIE Medical Imaging - Physiology, function and structure from medical images, 2006b.
- S de Putter, BJBW Wolters, MCM Rutten, M Breeuwer, FA Gerritsen, and FN van de Vosse. Patient-specific initial wall stress in abdominal aortic aneurysms with a backward incremental method. *J Biomech*, 40:1081–1090, 2007.
- ES di Martino, G Guadagni, A Fumero, G Ballerini, R Spirito, P Biglioli, and A Readaelli. Fluid-structure interaction within realistic three-dimensional models of the aneurysmatic aorta as a guidance to assess the risk of rupture of the aneurysm. *Med Eng & Phys*, 23:647–655, 2001.
- ES di Martino, S Mantero, F Inzoli, G Melissano, D Astore, R Chiesa, and R Fumero. Biomechanics of abdominal aortic aneurysm in the presence of endoluminal thrombus: experiment characterisation and structural static computational analysis. *Eur J Vasc Endovasc Surg*, 15:290–299, 1998.
- ES di Martino and DA Vorp. Effect of variation in intraluminal thrombus constitutive properties on abdominal aortic aneurysm wall stress. *Ann Biomed Eng*, 31:804–809, 2003.
- PB Dobrin. Pathophysiology and pathogenesis of aortic aneurysms, current concepts. *Surg Clin N Am*, 69(4):687–703, 1989.
- E Falk. Dynamics in thrombus formation. *Ann New York Acad Sci*, pages 205–223, 1992.
- ZA Fayad, JT Fallon, M Shinnar, S Wehrli, HM Dansky, M Poon, JJ Badimon, SA Charlton, EA Fisher, JL Breslow, and V Fuster. Non-invasive in vivo high-resolution magnetic resonance imaging of atherosclerotic lesions in genetically engineered mice. *Circulation*, 98:1541–1547, 1998.
- MF Fillinger, SP Marra, ML Raghavan, and FE Kennedy. Prediction of rupture risk in abdominal aortic aneurysm during observation: wall stress versus diameter. *J Vasc Surg*, 37(4):724–32, 2003.

- MF Fillinger, ML Raghavan, SP Marra, JL Cronenwett, and FE Kennedy. In vivo analysis of mechanical wall stress and abdominal aortic aneurysm rupture risk. *J Vasc Surg*, 36:589–97, 2002.
- V Fontaine, Z Touat, EM Mtairag, R Vranckx, L Louedec, X Houard, B Andreassian, U Sebbag, T Palombi, MP Jacob, O Meilhac, and JB Michel. Role of leukocyte elastase in preventing cellular re-colonization of the mural thrombus. *Am J Pathol*, 164:2077–2087, 2004.
- SC Franks, AJ Sutton, and RD Sayers. Systematic review and meta-analysis of 12 years of endovascular abdominal aortic aneurysm repair. *Eur J Endovasc Surg*, 33:154–171, 2007.
- P Frey, B Sarter, and M Gautherie. Fully automatic mesh generation for 3d domains based upon voxel sets. *Int J Num Meth Eng*, 37:2735–2753, 1994.
- JP Vande Geest, MS Sacks, and DA Vorp. The effects of aneurysm on the biaxial mechanical behavior of human abdominal aorta. *J Biomech*, 39(7):1324–1334, 2006.
- JJ Grange, V Davis, and BT Baxter. Pathogenesis of abdominal aortic aneurysm: an update and look toward the future. *Cardiovasc Surg*, 5(3):256–265, 1997.
- CM He and MR Roach. The composition and mechanical properties of abdominal aortic aneurysms. *J Vasc Surg*, 20(1):6–13, 1994.
- JW Hinnen, DJ Rixen, OHJ Koning, JH van Bockel, and JF Hamming. Development of fibrinous thrombus analogue for in-vitro abdominal aortic aneurysm studies. *J Biomech*, 40(2), 2007.
- M Hrapko, JAW van Dommelen, GWM Peters, and JSHM Wismans. The mechanical behaviour of brain tissue: large strain response and constitutive modelling. *Biorheology*, 43(5):623–636, 2006.
- HT Hua, RP Cambria, SK Chuang, MC Stoner, CJ Kwolek, KS Rowell, SF Khuri, WG Henderson, DC Brewster, and WM Abbott. Early outcomes of endovascular versus open abdominal aortic aneurysm repair in the national surgical quality improvement program-private sector (nsqip-ps). *J Vasc Surg*, 41:382–389, 2005.
- J Hua and WR Mower. Simple geometric characteristics fail to reliably predict abdominal aortic aneurysm wall stress. *J Vasc Surg*, 34:308–315, 2001.
- F Inzoli, F Boschetti, M Zappa, T Longo, and R Fumero. Biomechanical factors in abdominal aortic aneurysm rupture. *Eur J Vasc Endovasc Surg*, 7:667–674, 1993.
- VV Itskovich, DD Samber, V Mani, JGS Aguinaldo, JT Fallon, CY Tang, V Fuster, and ZA Fayad. Quantification of human atherosclerotic plaques using spatially enhanced cluster analysis of multicontrast-weighted magnetic resonance images. *Mag Res Med*, 52:515–523, 2004.
- M Kazi, J Thyberg, P Religa, J Roy, P Eriksson, U Hedin, and J Swedenborg. Influence of intraluminal thrombus on structural and cellular composition of abdominal aortic aneurysm wall. *J Vasc Surg*, 38:1283–1292, 2003.
- ME Kooi, VC Cappendijk, KBJM Cleutjens, AGH Kessels, PJEHM Kitslaar, M Borgers, PM Frederik, MJAP Daemen, and JMA van Engelshoven. Accumulation of ultra-small superparamagnetic particles of iron oxide in human atherosclerotic plaques

- can be detected by in vivo magnetic resonance imaging. *Circulation*, 107:2453–2458, 2003.
- PS Lloyd. Least square quantization in pcm. *IEEE Trans Inform Theory IT-2*, pages 129–137, 1982.
- WE Lorensen and HE Cline. Marching cubes: a high resolution 3d surface construction algorithm. *Computer Graphics*, 21(4):163–169, 1987.
- GT Luk-Pat, GE Gold, EW Olcott, BS Hu, and DG Nishimura. High-resolution three-dimensional in vivo imaging of atherosclerotic plaque. *Mag Res Med*, 42:762–771, 1999.
- CW Macosko. *Rheology. Principles, measurements and applications*. VCH publishers, 1994.
- STR MacSweeney, JT Powell, and RM Greenhalgh. Pathogenesis of abdominal aortic aneurysm. *Brit J Surg*, 81:935–941, 1994.
- SP Marra, CP Daghljan, MF Fillinger, and FE Kennedy. Elemental composition, morphology and mechanical properties of calcified deposits obtained from abdominal aortic aneurysms. *Acta Biomat*, 2:515–520, 2006.
- MHH Meuwissen. *An Inverse Method for the Mechanical Characterisation of Metals*. PhD thesis, Technische Universiteit Eindhoven, 1998.
- J Morrisett, W Vick, R Sharma, G Lawrie, M Reardon, E Ezell, J Schwartz, G Hunter, and D Gorenstein. Discrimination of components in atherosclerotic plaques from human carotid endarterectomy specimens by magnetic resonance imaging ex vivo. *Mag Res Imag*, 21:465–474, 2003.
- WR Mower, WJ Quinones, and SS Gambhir. Effect of intraluminal thrombus on aortic aneurysm wall stress. *J Vasc Surg*, 26(4):602–608, 1997.
- Y Papaharilaou, JA Ekaterinaris, E Manousaki, and AN Katsamouris. A decoupled fluid structure approach for estimating wall stress in abdominal aortic aneurysms. *J Biomech*, 40(2):367–377, 2007.
- JC Parodi, JC Palmaz, and HD Barone. Transfemoral intraluminal graft implantation for abdominal aortic aneurysms. *Ann Vasc Surg*, 5:491–499, 1991.
- ML Raghavan, MF Fillinger, SP Marra, BP Naegelein, and FE Kennedy. Automated methodology for determination of stress distribution in human abdominal aortic aneurysm. *Trans ASME*, 127:868–871, 2005.
- ML Raghavan and DA Vorp. Toward a biomechanical tool to evaluate rupture potential of abdominal aortic aneurysm: identification of a finite strain constitutive model and evaluation of its applicability. *J Biomech*, 33:475–482, 2000.
- ML Raghavan, DA Vorp, MP Federle, MS Makaroun, and MW Webster. Wall stress distribution on three-dimensionally reconstructed models of human abdominal aortic aneurysm. *J Vasc Surg*, 31(4):760–769, 2000.
- MS Sacks, DA Vorp, ML Raghavan, MP Federle, and MW Webster. In vivo three-dimensional surface geometry of abdominal aortic aneurysms. *Ann Biomed Eng*, 27:469–479, 1999.

- CM Scotti, AD Shkolnik, SC Muluk, and EA Finol. Fluid-structure interaction in abdominal aortic aneurysms: effects of asymmetry and wall thickness. *Biomed Engin online*, 4(64), 2005.
- M Shinnar, JT Fallon, S Wehrli, M Levin, D Dalmacy, ZA Fayad, JJ Badimon, M Harrington, E Harrington, and V Fuster. The diagnostic accuracy of ex vivo mri for human atherosclerotic plaque characterization. *Art Thromb Vasc Biol*, 19:2756–2761, 1999.
- K Singh, KH Bonaa, BK Jacobsen, L Bjork, and S Solberg. Prevalence of and risk factors for abdominal aortic aneurysms in a population-based study - the tromso study. *A J Epid*, 514(3):236–244, 2001.
- L Speelman, A Bohra, EMH Bosboom, GWH Schurink, and FN van de Vosse. Effect of wall calcifications in patient-specific wall stress analyses of abdominal aortic aneurysms. *J Biomech Eng*, 129:1–5, 2007.
- MM Stringfellow, PF Lawrence, and RG Stringfellow. The influence of aorta-aneurysm geometry upon stress in the aneurysm wall. *J Surg Res*, 42:425–433, 1987.
- DS Sumner, DE Hokanson, and DE Strandness. Stress-strain characteristics and collagen-elastin content of abdominal aortic aneurysms. *Surg Gyn Obs*, 130:459–466, 1970.
- MA Sutton, M Cheng, WH Peters, YJ Chao, and SR McNeill. Application of an optimized digital correlation method to planar deformation analysis. *Im Vis Comp*, 4(3):143–150, 1986.
- MJ Thubrikar, J Al-Soudi, and F Robicsek. Wall stress studies of abdominal aortic aneurysm in a clinical model. *Ann Vasc Surg*, 15:355–366, 2001a.
- MJ Thubrikar, M Labrosse, F Robicsek, J Al-Soudi, and B Fowler. Mechanical properties of abdominal aortic aneurysm wall. *J Med Eng Tech*, 25(4):133–142, 2001b.
- J-F Toussaint, GM LaMuraglia, JF Southern, V Fuster, and HL Kantor. Magnetic resonance images lipid, fibrous, calcified, hemorrhagic, and thrombotic components of human atherosclerosis in vivo. *Circulation*, 94:932–938, 1996.
- R Uflacker and J Robison. Endovascular treatment of abdominal aortic aneurysms: a review. *Eur Radiol*, 11:739–753, 2001.
- EA van Dam, SD Dams, GWM Peters, MCM Rutten, GWH Schurink, J Buth, and FN van de Vosse. Determination of linear viscoelastic behavior of abdominal aortic aneurysm thrombus. *Biorheology*, 43:695–707, 2006.
- EA van Dam, SD Dams, GWM Peters, MCM Rutten, GWH Schurink, J Buth, and FN van de Vosse. Non-linear viscoelastic behavior of abdominal aortic aneurysm thrombus. *BMMB*, DOI 10.1007/s10237-007-0080-3, 2007.
- JA van der Vliet and APM Boll. Abdominal aortic aneurysm. *The Lancet*, 349:863–866, 1997.
- M van Turnhout, GWM Peters, A Stekelenburg, and CWJ Oomens. Passive transverse mechanical properties as a function of temperature of rat skeletal muscle. *Biorheology*, 42(3):193–207, 2005.

- AK Venkatasubramaniam, MJ Fagan, T Mehta, KJ Mylankal, B ray, G Kuhan, IC Chetter, and PT McCollum. A comparative study of aortic wall stress using finite element analysis for ruptured and non-ruptured abdominal aortic aneurysms. *Eur J Vasc Endovasc Surg*, 28:168–176, 2004.
- E Verhulp, B van Rietbergen, and R Huiskes. A three-dimensional digital image correlation technique for strain measurements in microstructures. *J Biomech*, 37:1313–1320, 2004.
- DA Vorp, PC Lee, DHJ Wang, MS Makaroun, EM Nemoto, S Ogawa, and MW Webster. Association of intraluminal thrombus in abdominal aortic aneurysm with local hypoxia and wall weakening. *J Vasc Surg*, 34:291–299, 2001.
- DA Vorp, WA Mandarino, MW Webster, and J Gorscan. Potential influence of intraluminal thrombus on abdominal aortic aneurysm as assessed by a new non-invasive method. *Cardiovasc Surg*, 4(6):732–739, 1996.
- DA Vorp, ML Raghavan, and MW Webster. Mechanical wall stress in abdominal aortic aneurysm: influence of diameter and asymmetry. *J Vasc Surg*, 27:632–639, 1998.
- DHJ Wang, MS Makaroun, MW Webster, and DA Vorp. Mechanical properties and microstructure of intraluminal thrombus from abdominal aortic aneurysm. *J Biomech Eng*, 123:536–539, 2001.
- DHJ Wang, MS Makaroun, MW Webster, and DA Vorp. Effect of intraluminal thrombus on wall stress in patient-specific models of abdominal aortic aneurysm. *J Vasc Surg*, 36:598–604, 2002.
- M Wassef, GR Upchurch, H Kuivaniemi, RW Thompson, and MD Tilson. Challenges and opportunities in abdominal aortic aneurysm research. *J Vasc Surg*, 45:192–198, 2007.
- A Wills, MM Thompson, M Crowther, RD Sayers, and PRF Bell. Pathogenesis of abdominal aortic aneurysms-cellular and biochemical mechanisms. *Eur J Vasc Endovasc Surg*, 12:391–400, 1996.
- YG Wolf and EF Bernstein. A current perspective on the natural history of abdominal aortic aneurysms. *Cardiovasc Surg*, 2(1):16–22, 1994.
- BJBM Wolters, MCM Rutten, GWH Schurink, U Kose, J de Hart, and FN van de Vosse. A patient-specific computational model of fluid-structure interaction in abdominal aortic aneurysms. *Med Eng & Phys*, 27:871–883, 2005.
- C Yuan, KW Beach, LH Smith, and TS Hatsukami. Measurement of atherosclerotic carotid plaque size in vivo using high resolution magnetic resonance imaging. *Circulation*, 98:2666–2671, 1998.
- C Yuan, WS Kerwin, MS Ferguson, N Polissar, S Zhang, J Cai, and TS Hatsukami. Contrast-enhanced high resolution mri for atherosclerotic carotid artery tissue characterization. *JMRI*, 15(1):62–67, 2002.
- C Yuan, LM Mitsumori, MS Ferguson, NL Polissar, D Echelard, G Ortiz, R Small, JW Davies, WS Kerwin, and TS Hatsukami. In vivo accuracy of multispectral magnetic resonance imaging for identifying lipid-rich necrotic cores and intraplaque hemorrhage in advanced human carotid plaques. *Circulation*, 104:2051–2056, 2001.

- CK Zarins, RA White, D Swarten, E Kinney, EB Diethrich, KJ Hodgson, and TJ Fogarty. Aneurx stent graft versus open surgical repair of abdominal aneurysms: Multicenter prospective clinical trial. *J Vasc Surg*, 29(2):292–308, 1999.
- GG Zimmermann-Paul, HH Quick, P Vogt, GK von Schulthess, D Kling, and JF Debatin. High-resolution intravascular magnetic resonance imaging, monitoring of plaque formation in heritable hyperlipidemic rabbits. *Circulation*, 99:1054–1061, 1999.

Samenvatting

Ruptuur van een abdominaal aorta aneurysma (AAA) brengt de patient in een levensbedreigende situatie. Wanneer het aneurysma tijdig wordt gediagnosticeerd, kan ruptuur voorkomen worden door middel van een endovasculaire of conventionele ingreep. Beide methoden gaan gepaard met een hoog mortaliteitspercentage en de ingreep zou dus alleen moeten worden uitgevoerd wanneer de risicos die verbonden zijn aan de ingreep kleiner zijn dan de kans op een ruptuur. Op dit moment wordt de diameter van het aneurysma gebruikt als criterium om te opereren. Kleine aneurysmata kunnen toch ruptureren, terwijl sommige grote aneurysmata nog niet geruptureerd zijn. De diameter op zich is dus geen sluitend criterium. Ruptuur treedt op als de spanningen in de wand groter worden dan de sterkte van het weefsel en men vermoedt dat ruptuur daarom beter voorspeld kan worden aan de hand van de verdeling van de spanning in de vaatwand.

Voor het berekenen van de wandspanning heeft men niet alleen de geometrie van het aneurysma nodig maar ook de mechanische eigenschappen van de weefsels. Bij studies naar de mechanische eigenschappen van de vaatwand is deze tot nu toe behandeld als een homogeen materiaal. Lokale inhomogeniteiten kunnen echter grote gevolgen hebben voor de spanningsverdeling. In de AAA vaatwand kunnen zich inhomogeniteiten als calcificaties en atherosclerotische plaques bevinden. Daarnaast is in een groot deel van de aneurysmata een gedeelte van de aneurysmabuik gevuld met trombus, een gelaagde fibrine structuur waarin verschillende degeneratie niveaus kunnen worden aangewezen. In dit werk worden de locale mechanische eigenschappen van zowel trombus als vaatwand bepaald met als doel de ruptuur kans voorspelling op basis van de wandspanning te verbeteren.

Vaatwand en trombus monsters worden verkregen van patienten die een conventionele ingreep ondergaan. Van de trombus worden de viscoelastische eigenschappen bepaald met plaat-plaat reologie. Door het bestuderen van een serie monsters genomen over de dikte van de trombus, kan het verloop van de mechanische eigenschappen over de dikte van de trombus worden bepaald. Voor kleine rekken zijn de elastische en visceuze modulus bepaald (1.7 ± 1.3 kPa en 0.2 ± 0.1 kPa respectievelijk). Trombus ondervindt in het lichaam echter grote rekken. De niet-lineaire eigenschappen zijn bepaald met spannings relaxatie experimenten. Vervolgens is een niet-lineair multi mode model gebruikt om het gedrag van de trombus te beschrijven. Om de morfologie van de vaatwand te bepalen, is de mogelijkheid om met multi contrast MRI de verschillende componenten te onderscheiden onderzocht. Multi con-

trast resultaten zijn vergeleken met de gouden standaarden μ CT en histologie. De vaatwandmedia, calcificaties, gebieden met veel cholesterol en de adventitia konden worden onderscheiden op de MR beelden. De resultaten zijn echter niet geschikt voor automatische classificatie van de verschillende componenten.

Om de mechanische eigenschappen van deze componenten te gebruiken is een gemengd numeriek experimentele methode ontwikkeld. Dit is een robuuste methode om de mechanische eigenschappen van individuele componenten van een monster te bepalen zonder deze te hoeven isoleren. Met deze methoden zijn de elasticiteitsmoduli van de verschillende componenten van AAA vaatwand bepaald. De media is weliswaar iets minder stijf dan de adventitia, maar de stijfheden zijn van dezelfde orde grootte (≈ 1 MPa). De stijfheid van de trombus ligt een orde grootte lager (≈ 40 kPa). Cholesterolrijke gebieden zijn stijver dan de media en adventitia (≈ 7.5 MPa) en een gecalcificeerd gebied is zelfs nog stijver (≈ 50 MPa).

Implementatie van de gerapporteerde elastische moduli voor trombus in een patient specifiek model leidt tot de conclusie dat trombus weliswaar een invloed heeft op de wandspanningsverdeling, maar dat het effect veel kleiner is dan tot nu toe wordt gerapporteerd in literatuur. Wanneer er calcificaties aanwezig zijn in de vaatwand dan heeft dat een groot effect op de spanningsverdeling. De nauwkeurigheid waarmee de geometrie van de calcificaties wordt beschreven heeft een grote invloed op de spanningsverdeling die berekend wordt in de wand. In de huidige klinische modellen is deze resolutie beperkt wat leidt tot een niet-realistische berekende wandspanningsverdeling. Om de inhomogeniteiten van de vaatwand goed te kunnen implementeren in de patient specifieke modellen dienen de resoluties van zowel de afbeeldingstechnieken als de berekeningen toe te nemen.

Dit werk draagt op verschillende punten bij aan het aneurysma onderzoek. Niet alleen worden de morfologie en mechanische eigenschappen van aneurysma wand en trombus gepresenteerd, maar leidt dit werk ook tot de aanbeveling ter verbetering van de klinische methoden zodat de morfologie en mechanische eigenschappen kunnen worden gebruikt in de ruptuurvoorspelling van aneurysmata.

Dankwoord

*-hand an de ploog, ik kreeg wat ik vroeg-
Vechte, valle en opstoan - Rowwen Heze*

Maar ik was natuurlijk niet de enige die de hand aan de grote promotieploeg hield. Ten eerste een woord van dank aan mijn directe begeleiders. Marcel, de discussies begonnen altijd serieus maar eindigde op de een of andere manier altijd in voor-het-onderzoek-niet-zo-heel-maar-voor-de sociale-ontwikkeling-zeer-relevante onderwerpen. Ondanks dat hebben jouw inzicht en mening een grote rol gespeeld bij de vormgeving van dit project en was je altijd bereid een helpende hand toe te steken als ik er zelf niet meer uitkwam. Gerrit, je werd er ergens halverwege bij betrokken toen we besloten dat we ook de trombus wilde meenemen in dit onderzoek. Ik wil je bedanken voor het geduld waarmee je hebt geïntroduceerd in de wondere wereld van de reologie. De stapels kladblaadjes waar hele materiaalbeschrijvingen op gehierogliefd stonden zal ik niet snel vergeten. Frans, ik heb erg kunnen waarderen dat je tijd had/maakte voor een wekelijks overleg. Het werkte niet alleen als een stok achter de deur, maar was ook de plaats waar alles bespreekbaar was. Ik wil je graag bedanken voor het vertrouwen dat je me gedurende het project hebt gegeven.

Zonder de medewerking van de vaatchirurgen van het AZM en het Catharina ziekenhuis, in het bijzonder Geert Willem Schurink en Jaap Buth, was dit proefschrift gebleven bij ideeën. De discussies met jullie confronteerde me er keer op keer mee dat aneurysmata nog steeds een probleem zijn en dit motiveerde mij enorm.

Een ander bron van motivatie was de samenwerking in het Hemodyn project. Het is goed te weten dat je werk niet voor niks is en dat anderen met aansluitend onderzoek bezig zijn. In het bijzonder wil Sander de Putter en Lambert Speelman bedanken voor de interesse in mijn werk en de daarbij behorende discussies over alle moeilijkheden die we tegenkwamen bij de aneurysma vaatwand en thrombus.

De leden van de NMR groep wil ik bedanken voor de hulp die ik steeds van jullie kreeg als ik weer eens niet wist hoe de kabels ook al weer aangesloten moesten worden aan de scanner. Vooral Gustav Strijkers en Klaas Nicolay wil ik bedanken voor de inhoudelijke inbreng op het gebied van de Multi contrast metingen.

Matej Hrapko en Marion Geerligts, jullie waren fijne gesprekspartners wanneer zich problemen voordeden bij de reologie experimenten en de verwerking daarvan. Bert van Rietbergen bedank ik voor het ter beschikking stellen van de μ CT scanner. Eelco

Verhulp wil ik graag bedanken voor het ontwikkelen van de imagecorrelatie en meshing software. Als ik dat niet van je had kunnen 'lenen' zat ik nu nog ergens in mijn eentje te programmeren. Voor de histologie ben ik Femke Hellenthal en Sylvia Heeneman heel veel dank verschuldigd.

Mijn dank gaat ook uit naar de (destijds) studenten die een bijdrage hebben geleverd. Judith, van jouw werk is uiteindelijk niets meer terug gekomen in het boekje, maar het vormde wel de basis voor hoofdstuk 4. Arjen, zonder jou geen hoofdstuk 5. Susanne, uit onze samenwerking zijn een tweetal mooie artikelen voortgekomen. Ik waardeer niet alleen jullie bijdrage, maar kijk ook met plezier terug op onze samenwerking.

Mijn ex-kamergenoten Marlies, Eelco en Wouter wil ik bedanken voor de nuttige en minder nuttige discussies en het zonder mopperen aanhoren van mijn lief en leed. Janine, ik weet niet of ik erg gezellig was, toen jij me kwam vergezellen in de laatste weken voordat het boekje af was, maar ik heb je gezelschap erg kunnen waarderen. Fijn dat er weer iemand was om mee te praten.

Naast het werk hebben familie en vrienden deze tijd tot een zeer aangename gemaakt. Een aantal wil ik in het bijzonder bedanken.

Met veel plezier ben ik al die jaren naar Maastricht afgereisd om op vrijdagavond bij de 'blouw' te repeteren. In het bijzonder wil ik iedereen bedanken die betrokken is bij de jeugd en opleidingen binnen onze harmonie. Het opzetten van een bijna compleet nieuw jeugdbeleid vormde een bijna even grote uitdaging als promoveren. Ondanks de successen die we geboekt hebben, gaf het een en ander mij reden genoeg om eens van iets anders dan promoveren wakker te liggen.

Geralda, Debby en Lotte, ik hoop dat we ook in toekomst onze traditie van 'meezing' films en dubieuze TV-series kijken kunnen voortzetten. Joep, Paulien, Marlies, Frank, Linda, Pim, Jiska, Edwin, Berent en Niels wil ik bedanken voor de (kampeer)weekenden en avonden waarin alle frustraties gedeeld werden. Zonder jullie waren de laatste vier jaar een eenzame tijd geweest.

Linda en Marlies, samen weten jullie alles van mij en kan ik dus zonder veel uitleg mijn groot en klein leed bij jullie kwijt. Daarnaast zijn Beer, Igor, Apple en alle eenden blij dat ik vrienden heb die elk pluche beest op zijn waarde weten te schatten.

Roelant, Brechtje en de familie Janssen wil ik bedanken voor de gezelligheid en de interesse in mij en mijn werk. Roelant, jouw meedenken en jouw silicakorrels hebben hoofdstuk 5 en 6 mogelijk gemaakt! Pap en mam, zonder jullie onvoorwaardelijke steun en interesse was ik niet zo ver gekomen. Het is fijn te weten dat ik altijd bij jullie kan aankloppen, ook als het eens niet zo meezit. Leon, herhaaldelijk heb je mijn 'relativator' gerepareerd omdat die door de hoeveelheid promotiestress helemaal vastliep. Jouw kalmte en steun zijn voor mij van onbetaalbare waarde.

Curriculum Vitae

Evelyne van Dam werd geboren op 5 oktober 1977 te Maastricht. In 1996 haalde zij haar VWO diploma aan de Stedelijke Scholengemeenschap Maastricht. Na het behalen van het Bachelor diploma van de studie biomedische technologie (BMT) aan de technische universiteit eindhoven (TU/e), koos zij voor de richting Biomechanics and Tissue Engineering bij de faculteit BMT. Zij voerde een stage uit aan de University of Pittsburgh. In deze stage werd de buiging van hartklep prothesen gedurende het open en sluiten bestudeerd. Dit werk werd vervolgd in een afstudeerproject waarin de stroming rond hartkleppen werd gevisualiseerd en bestudeerd met behulp van magnetic resonance imaging (MRI). Na de afronding hiervan in 2003 besloot zij te beginnen aan promotieonderzoek waarin de combinatie van MRI en biomechanica terugkeerde en dat resulteerde in dit proefschrift.